

FLOW DYNAMICS AROUND DOWNWELLING SUBMARINE CANYONS

by

Jessica Michelle Spurgin

B.Sc., Texas A&M University - Galveston, 2011

A THESIS SUBMITTED IN PARTIAL FULFILLMENT OF
THE REQUIREMENTS FOR THE DEGREE OF

MASTER OF SCIENCE

in

The Faculty of Graduate and Postdoctoral Studies

(Oceanography)

THE UNIVERSITY OF BRITISH COLUMBIA

(Vancouver)

March 2014

© Jessica Michelle Spurgin, 2014

Abstract

Flow dynamics around a downwelling submarine canyon were analyzed with the Massachusetts Institute of Technology general circulation model. Blanes Canyon (Northwest Mediterranean) was used for topographic and initial forcing conditions. Fourteen scenarios were modelled with varying forcing conditions. Rossby number and Burger number were used to determine the significance of Coriolis acceleration and stratification (respectively) and their impacts on flow dynamics. A new non-dimensional parameter (χ) was introduced to determine the significance of vertical variations in stratification. Downwelling (downwards advection of density) occurs under all forcing conditions and is enhanced within the canyon. High Burger numbers lead to negative vorticity and a trapped anticyclonic eddy within the canyon, as well as an increased density anomaly. Low Burger numbers lead to positive vorticity, cyclonic circulation and weaker density anomalies. Vertical variations in stratification affect zonal jet placement. Under the same forcing conditions, the zonal jet is pushed offshore in more uniformly stratified domains. Offshore jet location generates upwards density advection away from the canyon, while onshore jets generate downwards density advection everywhere within the model domain. Increasing Rossby values across the canyon axis, as well as decreasing Burger values, increase negative vertical flux at shelf break depth (150 m). Increasing Rossby numbers lead to stronger downwards advection of a passive tracer (nitrate). Comparisons were made to previous studies to explain how variations in initial forcing conditions impact regional flow dynamics.

Preface

This thesis describes experiments that used an open-source numerical model designed for the study of atmosphere, ocean, and climate (MIT general circulation model; Marshall et al., 1997). Methods for experimental design, model set-up, and result analysis were conceived and executed by the author, Jessica Spurgin. This work was supervised by Susan Allen; she assisted with experimental approach, comprehension of results and thesis edits. This work is unpublished, but undergoing preparation for submission to a peer reviewed journal.

Table of Contents

Abstract	ii
Preface	iii
Table of Contents	iv
List of Tables	vi
List of Figures	vii
Acknowledgements	ix
Dedication	x
1 Introduction	1
1.1 Importance of submarine canyons in the Mediterranean Sea	1
1.2 Coastal/open ocean separation	2
1.3 Flow around submarine canyons	3
1.4 Previous downwelling canyon studies	5
1.5 Study region; northwest Mediterranean Sea	7
1.6 Research objectives	7
2 Flow Dynamics of Downwelling Submarine Canyons	10
2.1 Model description	10
2.1.1 Domain and canyon bathymetry	10
2.1.2 Parameter specifications	11
2.1.3 Model simulations	12
2.1.4 Result calculations	16
2.2 Results	18

2.2.1	Flow evolution	18
2.2.2	Circulation in the canyon	20
2.2.3	Comparison to previous studies	24
2.2.4	Vorticity in the canyon	25
2.2.5	Upwelling in a downwelling canyon	27
2.2.6	Nitrate anomaly	34
2.3	Discussion	35
2.3.1	Upwelling in downwelling canyons	35
2.3.2	Parameter effects	36
2.3.3	Diffusivity	48
2.3.4	Summary: Circulation, flux, and advection for steady flow over downwelling canyons	49
2.4	Conclusion	50
3	Conclusions	51
3.1	Research objectives	51
3.1.1	Determine if upwelling occurs in or around downwelling canyons. If so, where does upwelling occur, and how intense is upwelling?	51
3.1.2	Determine what parameters affect flow dynamics.	52
3.2	Future research	54
3.3	Application to real world	55
	Bibliography	56
A	Boundary Conditions	61
B	Model Discretization	64
C	Advection Scheme	65
D	Extended Simulation	66
E	Aliasing	68
F	Additional Figures	70

List of Tables

1.1	Features seen in previous studies	9
2.1	Constant geometric parameters for model simulations	11
2.2	Non-dimensional parameters for all model simulations	13
2.3	Forcing flow for all model simulations	14
2.4	Temporal variations in forcing for all model simulations	16
2.5	Absolute vorticity and canyon circulation for all model simulations	25
2.6	Positive density anomaly depth range for all model simulations	32
2.7	Diffusive and advective flux of nitrate across 3 vertical planes	48

List of Figures

1.1	Model canyon bathymetry	4
1.2	Location of Blanes Canyon, Northwest Mediterranean Sea	8
2.1	Planes used for transport calculations	17
2.2	Time series of horizontal and vertical flux	19
2.3	Horizontal and vertical circulation during the time-dependent phase	21
2.4	Horizontal velocity vectors at shelf break depth	22
2.5	Particle trajectories in an anticyclonic simulation	23
2.6	Particle trajectories in a cyclonic simulation	24
2.7	Vorticity cross-sections at mid-canyon	26
2.8	Vertical velocity at shelf break depth	28
2.9	Times of net upwards across 3 vertical planes	29
2.10	Particle trajectories for all depths	30
2.11	Density anomaly at shelf break depth	31
2.12	Density difference anomaly at shelf break depth	33
2.13	Nitrate anomaly upstream and along the canyon axis	34
2.14	Isopycnal cross-sections at mid-canyon	37
2.15	Burger and incoming Rossby number effect on canyon vorticity	39
2.16	Zonal jet location upstream of the canyon	40
2.17	Incoming Rossby and canyon Rossby number correlation	41
2.18	Burger and canyon Rossby number effect on vertical flux	43
2.19	Burger and incoming Rossby number effect on density anomaly	45
2.20	Incoming Rossby number effect on nitrate anomaly	47
A.1	Isopycnal cross-sections along the upstream and downstream boundaries	63

D.1	Time series of horizontal and vertical flux over 20 model days	67
E.1	Time series of horizontal and vertical flux with 3 hour model output	69
F.1	Time series of horizontal and vertical flux for all model simulations	70
F.2	Horizontal velocity vectors at shelf break depth for all model simulations	73
F.3	Vorticity cross-sections at mid-canyon for all model simulations	75
F.4	Vertical velocity at shelf break depth for all model simulations	77
F.5	Density anomaly at shelf break depth for all model simulations	79
F.6	Density difference anomaly at shelf break depth for all model simulations	81
F.7	Nitrate anomaly upstream and along the canyon axis for all model simulations	83

Acknowledgements

I would like to thank my supervisor, Dr. Susan Allen for her constant assistance and support throughout my thesis program. Thank you Susan for always having time for a quick (and sometimes not so quick) meeting and for giving me the opportunity to grow and learn in a field in which I previously had limited experience. Also, thank you for the wonderful opportunity to get away from a computer screen and experience oceanography from an observational point of view.

I also wish to thank my supervisory committee (Dr. William Hsieh and Dr. Neil Balmforth) for their constructive input throughout my project. Thank you to Dr. Richard Pawlowicz for agreeing to examine my thesis, as well as all the useful suggestions during lab seminars.

Thank you to everyone in the Waterhole for your continued support and countless cookie breaks. You all were there to help keep my sanity in check, even when it seemed too late.

Finally, many massive thanks to my wonderful mother and extended family for their continual support and encouragement, no matter the miles between us. Mom, without your undying encouragement I never would have made it this far in my project or in my life. There is no one else I would want to take an 8 day cross-country trip with (twice).

Dedication

For my father who continues to watch over me and who gave me his love of all things science!

Chapter 1

Introduction

1.1 Importance of submarine canyons in the Mediterranean Sea

Almost 518 large submarine canyons have been identified in the Mediterranean Sea [Harris and White-way, 2011]. Interest in these canyons was initially driven by economic reasons (e.g. exploration for fossil energy resources and exploitation of ancient deposits), but recent interest has focused on submarine canyons and their impact on exchanges between the deep ocean and continental shelf [Wurtz, 2012].

Submarine canyons concentrate sediments rich in organics and contain denser deposits of phytodetritus [Garcia et al., 2008]; making canyons more favorable habitats for benthic consumers and suspension feeders. Complex topography within a canyon enhances habitat heterogeneity, creating a greater abundance and diversity of fish along margins where canyons are common [Marques et al., 2005; Morais et al. 2007].

Due to the presence of several submarine canyons (Cap de Creus, Palamòs, Blanes, Arenys and Merenguera Canyons), the Catalan continental margin supports an important commercial fishery [Company et al., 2012]. The deep-sea red shrimp *Aristeus antennatus* (Risso, 1816) is a target species and highly appreciated crustacean in this region [Company et al., 2012], making it an important resource to the local economy.

Hydrodynamics in these canyons depends upon forcing conditions such as bottom morphology, general circulation, and atmospheric regime [Company et al., 2012]. Such forcing conditions can vary between canyons and lead to different hydrodynamic responses. These hydrodynamic responses in turn affect particulate matter retention and/or resuspension and coastal biological productivity. Submarine canyons can be classified as upwelling or downwelling, depending on the incoming flow direction. Upwelling

canyons generally have incoming flow with the coast to the left, and downwelling canyons typically have a right-bounded flow (in the Northern Hemisphere).

Forcing conditions in the Mediterranean Sea create downwelling canyons, which have previously been found to enhance coastal downwelling [Klinck, 1996; Skliris et al., 2001; 2002]. However, the higher than average biological productivity of this region [Palomera, 1992; Sabates and Olivar 1996] helps sustain the important commercial fisheries.

This study will model a downwelling canyon based on forcing conditions observed in the Mediterranean Sea. Forcing conditions will then be varied to test their impacts on canyon hydrodynamics. Advection, horizontal and vertical circulation will be used to determine if downwelling is enhanced, or if upwelling occurs in these canyons.

1.2 Coastal/open ocean separation

The oceans cover approximately 71% of the Earth, with the coastal oceans covering only 7%. The proximity to land and its nutrient sources, the interception of sinking organic matter by the shallow seafloor, and the propensity for coastal upwelling all result in highly productive coastal ecosystems [Sigan and Hain, 2012]. A shallow feature, the shelf-break, occurs at the transition between the gently sloping continental shelf and the steeper continental slope and separates the coastal and open ocean.

Geostrophic flow occurs when the balance of forces in the horizontal is between pressure gradient force and Coriolis force. Geostrophic flow is parallel to isobars with high pressure to the right of the flow (in the Northern Hemisphere; left of the flow in the Southern Hemisphere). In homogeneous, geostrophic flow, fluid columns cannot change their area (due to no net horizontal flux into or out of them) and therefore move as rigid columns of water [Taylor, 1923]. In this state, flow cannot change its depth and is constrained to follow isobaths. When flow is stratified, it is similarly constrained up to a depth where there is zero flow [Brink, 1998]. Therefore, a shelf-break current that extends from the surface to depth blocks stratified (and non-stratified) geostrophic flow from crossing isobaths. This causes a lack of exchange and is illustrated by significant changes in water properties near the location of the shelf-break.

There are various processes (e.g. bottom friction and strong flow) that can break these dynamical constraints. Small-scale topography, such as submarine canyons, can lower the dynamical length-scale and allow cross-isobath flow. Numerical models have shown, based on incoming flow direction, submarine canyons can enhance upwelling/downwelling in coastal regions [Klinck, 1996]. Thus, submarine canyons have a significant impact on regional circulation and are therefore an important feature for coastal and

open ocean interaction.

1.3 Flow around submarine canyons

Submarine canyons are features typical of continental slopes and deeply incise the continental shelf. In coastal regions with submarine canyons, the characteristic length scale (L) is reduced from the scale of the slope or shelf, to the scale of the canyon, which is often an order of magnitude smaller [Allen and Durrieu de Madron, 2009]. By reducing the length scale, the non-dimensional Rossby number (U/fL ; where U = incoming velocity and f = Coriolis parameter) increases and effects due to advection of momentum become important.

In a review of coastal submarine canyons, Hickey [1995] points out that, on a regional scale, physical processes can be modified/enhanced due to the presence of a submarine canyon. Some of these processes include mixing, internal wave activity, upwelling and cross-shelf/slope exchange. These processes can in turn affect mass balance on regional and larger scales.

Allen and Durrieu de Madron [2009] distinguished three phases of flow response during an upwelling or downwelling scenario due to realistic coastal winds:

- 1) An initial time-dependent response (shelf flow increases). This response is strong and usually occurs within an inertial period [Klinck, 1988; Kämpf, 2006]. If alongshore-current continues to increase (i.e. because of steady winds) density advection within the canyon reduces time-dependent upwelling after about 5 days [She and Klinck, 2000].

- 2) An advection dominated response (shelf break flow is reasonably steady). This response is strongly dependent on canyon topography and flow strength [Allen, 2004]. For weaker flows, it can be enhanced if convergent isobaths occur over the canyon [Allen, 2000; Waterhouse et al., 2009].

This advection dominated phase is not friction controlled but friction influenced and the concept of "steady" advection driven flow is theoretical. In reality wind is continually changing, which drives small changes in the strength of zonal flow; if the flow stops, the flow slowly spins down. These small changes in zonal flow impact other dynamics within the system. During this quasi-steady state, even with steady forcing, flow can exhibit oscillations over multi-day periods [She and Klinck, 2000].

- 3) A relaxation phase (shelf break flow decreases). This phase sees strong, generally cyclonic flow within the canyon [Hickey, 1997].

Consider a right bounded flow (in the same direction as Kelvin wave propagation). The current will be in geostrophic equilibrium with a cross-shore pressure gradient, where pressure is lower towards the open

ocean. Within the canyon, alongshore flow is restricted by canyon walls and the Coriolis force cannot balance the cross-shore pressure gradient [Allen and Durrieu de Madron, 2009]. These right bounded flows are generally associated with net downwelling (downward flow and flow toward the ocean) [Klinck, 1996].

The shoreward end of a canyon is known as the canyon head, while the broader side opening towards the open ocean is referred to as the canyon mouth (Figure 1.1). The boundary between the continental shelf and submarine canyon is known as the canyon rim. The term shelf break refers to the continental edge, where slope gradients increase toward the deep ocean bottom. For the purposes of this study, the term canyon wall will refer to the vertical rise between bottom topography and the canyon rim. Flow direction is towards the downstream, so 61-120 km (in the alongshore) is referred to as upstream of the canyon axis, and anything 0-59 km is downstream of the canyon axis.

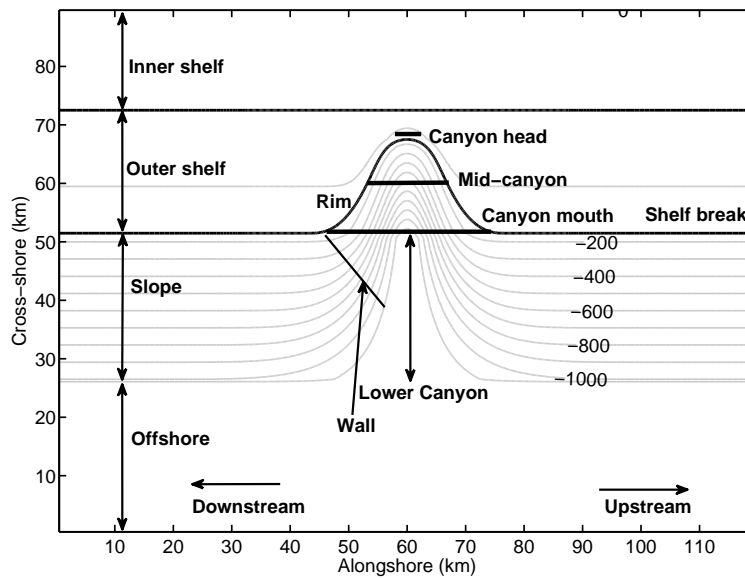


Figure 1.1: Canyon bathymetry (gray lines) and reference terminology used in this thesis. Canyon rim indicates the boundary between the continental shelf and the canyon. Shelf break indicates change in slope gradient between the continental shelf and slope. Canyon mouth is the open region along the shelf break; canyon head is the shallowest onshore canyon region; mid-canyon is the region between the canyon head and mouth; lower canyon is offshore of the canyon mouth. Canyon wall refers to canyon topography between shelf break and bottom depth. Zonal flow is in the alongshore, and meridional flow is in the cross-shore. Contour intervals are 100 m.

1.4 Previous downwelling canyon studies

The direction of alongshore flow is critical to the circulation over a canyon [Klinck, 1996]. For right-bounded coastal flows, the geostrophic pressure gradient is offshore. Under barotropic forcing, the flow at the shelf break turns towards the coast and begins to slow and weaken, due to the large scale, cross-shore pressure gradient, which leads to a reduction in the Coriolis acceleration [Klinck, 1996]. This reduction allows water to be pushed down the topographic slope. Once water crosses the axis of the canyon, it is then accelerated by the large scale pressure gradient, and begins to rise due to the increased Coriolis acceleration. With weak dissipation, water returns almost to its original depth and continues alongshore [Klinck, 1996].

With either a uniform incoming flow or a continental slope jet, antisymmetrical upwards (downwards) vertical velocity is seen in the downstream (upstream) region of a canyon, with upwards velocity being less intense than downwards velocity [Klinck, 1996; Skliris et al., 2002, respectively]. In both cases, cyclonic circulation is seen in the canyon head, as well as negative density anomalies everywhere over the canyon (with positive anomalies both upstream and downstream of the canyon in the slope region).

Stratification controls the magnitude of a forcing response and limits the influence of a canyon on overlying flow, independent of the direction of alongshore flow [Klinck, 1996]. Increased stratification reduces vertical and cross-shore transport, as well as depth range over which fluid parcels move in a circuit around a canyon [Klinck, 1996; Skliris et al., 2002].

Aside from Klinck [1996] and Skliris [2001, 2002], there are several other studies of downwelling submarine canyons, mostly numerical models of canyons in the northwest Mediterranean Sea.

Observational cruises near Palamòs Canyon (northeastern edge of Spain) reveal that small-scale temporal variability in the onshore/offshore location of an incoming zonal jet has important impacts on flow dynamics [Alvarez et al., 1996]. Transient factors (such as river runoff and the climatology of the area) induce a series of modifications in the permanent front-current of the region; affecting both its vertical extension and offshore location [ibid.]. In areas where canyon width is narrow and depth variations are strong (i.e. canyon head), vorticity adjustments and associated vertical velocities are induced as part of ageostrophic adjustment, and the core of the front-current is displaced offshore downstream of the canyon [Alvarez et al., 1996]. When incoming zonal jets are displaced onshore, flow is narrower and faster, and vertical velocities are greater (relative to an incoming zonal jet placed further offshore) [Jordi et al., 2005]. The ageostrophic component of the current is more significant when a coastal current interacts with the canyon head instead of the canyon mouth [Alvarez et al., 1996; Jordi et al. 2005]. In areas where

depth changes are not so strong and the canyon is wide (i.e. canyon mouth), flow adjustment is almost geostrophic and vertical velocity allows flow to maintain a thermal wind balance [Alvarez et al., 1996]. At high Rossby number, vorticity and vertical velocity are maximum where a coastal jet interacts with a canyon [Jordi et al., 2005].

Under constant downwelling winds and at low Rossby number ($R_o = 0.005$), a strong anticyclone within a canyon (in the upper 200 m) and small net cross-shore exchanges are driven by vortex compression or frictional coupling to alongshore flow [She and Klinck, 2000]. Along the canyon mouth and above shelf break depth (150 m), upstream onshore (into canyon) transport is stronger than downstream offshore (out of canyon) transport. Transports below shelf break depth are net offshore until the anticyclone forms, at which point net cross-shore transport becomes onshore. Vertical flux is downwards everywhere over the canyon at shelf break depth and stronger over the upstream rim.

Observational cruises around Blanes Canyon (northwest Mediterranean Sea) use velocity (measured with Acoustic Doppler Current Profiler, ADCP) and hydrographic (measured with Conductivity, Temperature, Depth instrument, CTD) samples taken in the upper 400 m of 59 stations in and around the canyon to study horizontal and vertical circulation [Flexas et al., 2008]. Velocity data shows that near the shelf break, flow follows isobaths along canyon walls, with weak circulation in the canyon head. In the upper 100 m, circulation is cyclonic along the canyon mouth, but anticyclonic within the canyon. Vertical velocity is estimated in 10 m depth layers, using conservation of volume and balancing vertical volume flux and net horizontal flux in each layer. In the upper 100 m, vertical velocities are negative (maximum velocity = $-6.9 \times 10^{-4} \text{ m s}^{-1}$). From 100-200 m, vertical velocities are positive (maximum velocity = $3.1 \times 10^{-4} \text{ m s}^{-1}$). Density sections suggest local downwelling/upwelling occurs along the upstream/downstream canyon walls between 100 m to 200 m depth.

Meandering of the Northern Current (NW Mediterranean Sea) has been found to enhance vertical motions inside Blanes Canyon and impact local net upwelling/downwelling events [Ahumada-Sempol et al., 2013]. Northern Current meanders produce an oscillation of the vertical flow characterized by net upwelling when the onshore meander is located over the upstream side of the canyon followed by net downwelling as the meander moves downstream [ibid.]. Net vertical fluxes are approximately two orders of magnitude higher in the presence of a meander than in its absence.

1.5 Study region; northwest Mediterranean Sea

As previously stated, flow dynamics in submarine canyons depend on forcing conditions, which can vary between canyon systems and individual canyons. For the purpose of this study, canyon topography is based on the bathymetry of Blanes Canyon. Blanes Canyon is one of the few submarine canyons in the Mediterranean Sea for which there have been multiple observational and numerical studies. Forcing conditions measured in previous studies are used to create a basic downwelling scenario similar to that observed in Blanes Canyon. However, changes to individual forcing parameters are made to better understand the impacts to flow dynamics on any downwelling submarine canyon.

Circulation in the Mediterranean Sea is characterized by a large cyclonic gyre of incoming Atlantic waters (Northern Current) [Wurtz, 2012]. This flow can generate anticyclonic eddies on the right side (onshore side) and cyclonic eddies on the left side (offshore side), strongly affecting current patterns within the continental shelf and pelagic domain, respectively. Bottom morphology, wind forcing, river runoff and changes in regional climatology can alter current patterns, thus the main feature of Mediterranean circulation is a high time-volume variability. Because the Mediterranean Sea is a semi-enclosed basin with a narrow inlet/outlet into the Atlantic (the Strait of Gibraltar), tides are very small (i.e. maximum tidal amplitudes, away from the Strait of Gibraltar, are less than 10 cm [Tsimplis et al., 1995]) and are thus neglected in canyon studies of the region.

Blanes Canyon (BC) lies along the Catalan coast, in the northwest Mediterranean Sea (Figure 1.2). General circulation around BC includes a baroclinic current (Northern Current), the path of which is generally a cyclonic flow along the continental slope [Millot, 1999]. The Northern Current is 30 to 50 km wide and is characterized by a velocity profile of about 30 to 50 cm s⁻¹ at the surface, decreasing approximately linearly with depth to speeds of a few centimeters per second at several hundred meters depth [Lapouyade and de Madron, 2001]. In fall, the core of the Northern Current has been observed as narrow, lying over the shelf break with velocities of about 20 cm s⁻¹ [Flexas et al., 2008].

1.6 Research objectives

Of the relatively few studies of downwelling submarine canyons, there does not appear to be a clear agreement on flow dynamics. Some numerical models find antisymmetrical upwelling and downwelling occurring in canyons, with downwelling being slightly stronger and net warmer/denser water everywhere within canyons [Klinck, 1996; Skliris et al., 2001; 2002]. One observational study [Flexas et al., 2008] and one numerical model [Ardhuin et al., 1999] show net upwelling of water parcels. Some models exhibit

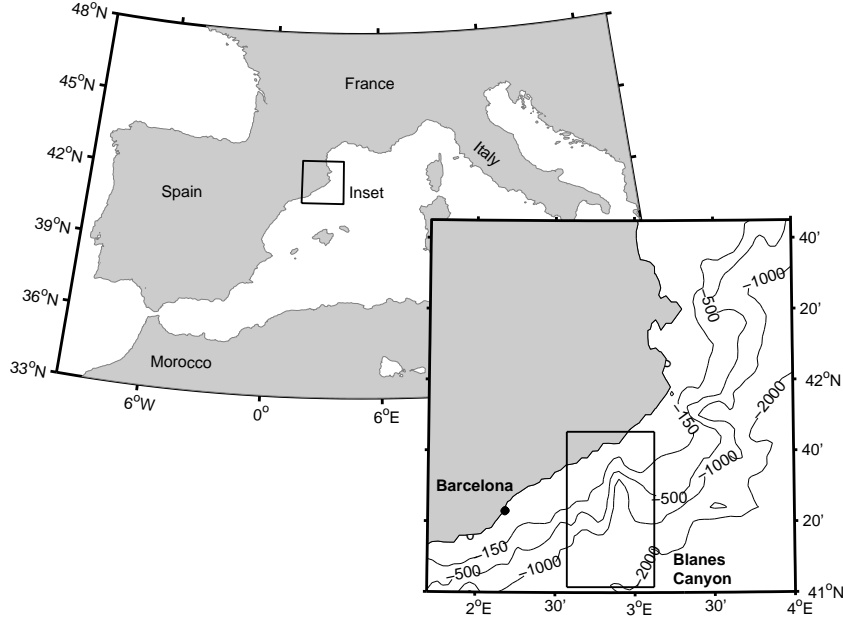


Figure 1.2: Location of Blanes Canyon, Northwest Mediterranean Sea.

cyclonic circulation everywhere over a canyon [Klinck, 1996; Skliris et al., 2001; 2002], and other models exhibit anticyclonic circulation at the shelf break depth [Arduin et al., 1999; She and Klinck, 2000].

In order to create an encompassing explanation of flow dynamics in downwelling canyons, it is important that current simulations are able to reproduce results of previous work. Then, from these simulations, the parameters that drive flow dynamics can be inferred. This study attempts to better understand these and other differences between previous studies, as well as resolve the parameters that drive general flow dynamics in downwelling submarine canyons. The objectives of this study are:

- 1) Determine if upwelling occurs in or around downwelling canyons. If so, where does upwelling occur, and how intense is upwelling?
- 2) Determine what parameters affect flow dynamics. Particularly, which parameters impact:
 - (a) horizontal circulation
 - (b) vertical transport
 - (c) density advection
 - (d) passive tracer advection

The core simulation is a model of Blanes Canyon, which replicates observations of Flexas et al. [2008]. Simulations of Klinck [1996], She and Klinck [2000], and Skliris et al. [2001, 2002] are also replicated.

The key features this study attempts to reproduce are summarized in Table 1.1.

The current model simulations have varying coastal jet placement. However, none of the simulations include time-varying onshore/offshore jet displacements or meandering of the shelf break current, such as those found in the studies performed by Alvarez et al. [1996], Jordi et al. [2005], and Ahumada-Sempool et al. [2013]. While these studies have found time-varying current displacement to have significant impacts on flow dynamics, this specification adds a level of complexity to the model that is beyond the scope of the current study. One goal of this study is to identify the parameters that impact flow dynamics in a general, semi-steady state scenario. After these primary features are understood, future models can build upon the basic understanding and increase the complexity in simulations.

Table 1.1: Features seen in previous studies

Study	Vorticity	Vertical Velocity	Temporal density change
Klinck [1996]	Positive everywhere	Net downwards (anti-symmetrical)	Negative everywhere in canyon; positive on either side of the canyon
She and Klinck [2000]	Negative over the canyon, cyclonic at 300 m	Net downwards	—————
Skloris et al. [2001, 2002]	Positive everywhere	Net downwards (anti-symmetrical)	Negative everywhere in canyon; positive on either side of the canyon
Flexas et al. [2008]	Negative over canyon	Net upwards	—————

Chapter 2

Flow Dynamics of Downwelling Submarine Canyons

2.1 Model description

Simulations were run with the Massachusetts Institute of Technology general circulation model (MIT-gcm) [Adcroft et al., 2004]. The model is rooted in incompressible Navier-Stokes equations; non-hydrostatic terms were used for all simulations.

2.1.1 Domain and canyon bathymetry

The model domain is 120 km in the alongshore (x-direction), 90 km in the cross-shore (y-direction), and 1200 m in the vertical (z-direction) (Figure 1.1). Positive x points upstream (eastward), positive y points onshore (northward), and positive z points upwards.

Minimum ocean depth is 20 m and stretches for ~ 20 km in the cross-shore (hereafter referred to as the inner shelf). Between the inner shelf and shelf break lies the outer shelf; in this region depth drops to 150 m over 20 km. The slope extends from the shelf break (150 m) to an abyssal depth of 1200 m, and extends over 25 km in the cross-shore. The canyon topography was based on Blanes Canyon bathymetry shown by Flexas et al., [2008]. Geometric parameters were kept nearly constant in all model simulations (Table 2.1).

Table 2.1: Constant geometric parameters for model simulations

Variable	Symbol	Value
Depth at shelf break	H_s [m]	150
Depth at canyon head*	H_h [m]	30
Depth drop across canyon	H_c [m]	950
Depth of basin	d [m]	1200
Canyon length	L [m]	16180
Width at shelf break	W_{sb} [m]	13005
Width at mid-canyon	W [m]	7660

*Value is different for Klinck-like simulation (KL), which used a flat shelf; $H_h = 150$ m.

2.1.2 Parameter specifications

Temperature, salinity, and nitrate stratification in the model were based on data from the National Virtual Ocean Data System (NVO DS, <http://ferret.pmel.noaa.gov/NVO DS/UI.vm>). Measured values at various depths of temperature and salinity were collected from the World Ocean Atlas 2005 1x1 degree Monthly Means at approximately 40.5°N, 2.5°E. Values for nitrate were collected from annual means of the same data set at the same position. For high vertical resolution runs, values between data points were linearly interpolated. A linear equation of state was applied, with a thermal expansion coefficient of 2.0×10^{-4} ($^{\circ}\text{C}^{-1}$) and a haline contraction coefficient of 7.4×10^{-4} .

Horizontal resolution varies in alongshore and cross-shore directions, grid spacing is ~ 1 km along each boundary and decreases linearly to 200 m over the canyon. Overall, there is 200 m horizontal spacing between 33 km to 87 km in the alongshore, and 20 km to 80 km in the cross-shore. Ninety vertical layers are concentrated around the top of the domain, and vertical spacing ranges from 5 m (in the upper 200 m) to 20 m (everywhere below 200 m).

The Coriolis parameter was assumed constant ($f = 1.0 \times 10^{-4} \text{ s}^{-1}$). Bottom friction was parameterized with a quadratic drag coefficient of 2.0×10^{-3} . A vertical eddy viscosity of $1.0 \times 10^{-2} \text{ m}^2 \text{ s}^{-1}$ was applied. The model used non-hydrostatic equation sets, with a time step of 40 seconds for all runs. Viscous (i.e. no-slip) conditions were applied at the sides and bottom of the domain, and an implicit free surface was used. Heat and salt were laterally and vertically diffused with a Laplacian diffusivity of $1 \times 10^{-7} \text{ m}^2 \text{ s}^{-1}$. A Smagorinsky harmonic viscosity factor [Smagorinsky, 1963] of 2.2 was applied (as recommended in Griffies and Hallberg [2000]). All tracers (i.e. temperature, salinity, and nitrate) were advected in time using a 3rd order direct space-time with flux limiting scheme.

All model scenarios had a closed (no-slip) boundary along the coastal boundary. The offshore bound-

ary was open with an Orlanski [1976] radiation condition applied. All but 2 simulations used periodic alongshore conditions; these two simulations will be explained further in the next section.

2.1.3 Model simulations

All modelled scenarios were forced by applying a wind stress and/or body force over the domain. A body force was applied as an additional forcing to the momentum equations [Dawe and Allen, 2010]. Fourteen scenarios were modelled based on minor changes in either forcing or domain stratification (Table 2.2, Table 2.3). Two non-dimensional parameters were calculated to highlight incoming velocity (Rossby number, R_o):

$$R_o = \frac{U}{fL}$$

and stratification (Burger number, B_u):

$$B_u = \frac{N_{sb}H_{sb}}{fW}.$$

Dynamic parameters are incoming velocity, U , the Coriolis parameter, f , and stratification characterized by the buoyancy frequency at shelf break depth (150 m), N_{sb} . Geometric parameters are length of the canyon, L , depth at the shelf break, H_{sb} , and width across mid-canyon, W .

To better understand the impact changes in stratification have on flow dynamics, a third parameter, a non-dimensional measure of vertical stratification, χ , was introduced. This new parameter measured uniformity of stratification and was calculated as the change in buoyancy frequency (N) divided by the average frequency near shelf break depth:

$$\chi = \Delta N(z)[\bar{N}(z)]^{-1},$$

where $N(z)$ is measured over a lengthscale of ± 75 m from the shelf break and $\bar{N}(z)$ is the average stratification over the lengthscale. Negative χ values indicate stronger stratification in the shallower layers.

In addition, placement of incoming coastal jets varied, vertically and horizontally, in previous studies (Table 2.3). These were recreated to ensure the dynamics of the original studies were reproduced.

Core model simulations were based on the Flexas et al., [2008] observations. The first scenario (uniform wind, **UW**) consisted of a uniform wind stress ($\tau = -0.0626$ N m⁻²) to drive a current along the surface, and a body forcing (applied near shelf break depth) to drive a current along the shelf break (similar to the Northern Current seen in the Mediterranean Sea). The current was accelerated over the first two model days, and then held at a steady state for the remainder of the simulation (steady state indicates maximum flow velocity never varied more than 20%).

Table 2.2: Non-dimensional parameters for all model simulations

	Rossby number (R_o)	Burger number (B_u)	Stratification Uniformity (χ)
UW	0.22	0.46	-0.64
OW	0.25	0.46	-0.64
OBC	0.28	0.46	-0.64
ST	0.25	0.46	-0.64
KL	0.07	0.16	0
SK	0.04	0.14	-0.46
US	0.21	0.16	0
HB	0.28	0.46	0
She	0.04	0.28	-0.35
SF	0.05	0.46	-0.64
LRC	0.09	0.46	0
SHR	0.15	0.14	-0.46
BLRB	0.12	0.28	-0.63
KHRB	0.22	0.46	0

The second scenario (opposing wind, **OW**) consisted of two opposing wind stresses to drive surface flow, and a slightly stronger body forcing to drive the shelf break current. This setup was used to reproduce eastward flow seen over the continental shelf [Flexas et al., 2008]. To match the offshore distance of the eastward flow, wind stresses were applied such that the offshore two-thirds of the domain had a wind stress of $\tau = -0.0626 \text{ N m}^{-2}$ and the nearshore one-third of the domain had a wind stress of $\tau = +0.0376 \text{ N m}^{-2}$. Again, the current was increased during the first two model days.

Additional scenarios were modelled to either recreate flow dynamics seen in previous numerical studies (3 scenarios) or investigate other impacts to flow dynamics (9 scenarios).

A Klinck-like (**KL**) scenario was modelled using a uniform stratification ($N = 0.0016 \text{ s}^{-1}$) and a flat shelf at 150 m (topography everywhere else in the domain remained the same) [Klinck, 1996]. A mostly uniform flow was reproduced by removing all wind stress and y-dependence in the body forcing. However, flow over the flat shelf was weaker relative to flow along the continental shelf and over the open ocean. Speed of the body forcing was reduced to create a zonal velocity of about 10 cm s^{-1} .

A Skliris-like (**SK**) simulation has uniform stratification over three regions: 1) the upper 20 m ($N = 6.0 \times 10^{-3} \text{ s}^{-1}$); 2) from 20 m to 120 m ($N = 1.5 \times 10^{-3} \text{ s}^{-1}$); 3) from 120 m to bottom depth ($N = 0.5 \times 10^{-3} \text{ s}^{-1}$) [Skliris et al., 2001]. Wind stress was removed, but y dependence on body forcing was kept. Body forcing was reduced to create a maximum zonal velocity of approximately 7 cm s^{-1} .

To simulate the She and Klinck [2000] study, a constant weak body forcing was applied over the upper

Table 2.3: Forcing flow for all model simulations

	Jet location	Vertical shear	Horizontal shear
UW	outer shelf	surface intensified; negligible along bottom topography	intensified over mid-outer shelf to shelf break
OW	outer shelf	surface intensified; negligible along bottom topography	intensified over mid-outer shelf to shelf break
OBC	outer shelf	surface intensified; negligible along bottom topography; secondary jet at shelf break	intensified over shelf break
ST	outer shelf	surface intensified; negligible along bottom topography	intensified over mid-outer shelf to shelf break
KL	offshore	uniform offshore	uniform offshore of shelf break; weak flow over flat shelf (shelf break to coast)
SK	shelf break	intensified along bottom topography (150-600 m)	intensified between shelf break and 10 km offshore
US	offshore	intensified at shelf break depth (150 m); negligible along continental slope	intensified 5 km offshore of shelf break
HB	offshore	intensified at shelf break depth (150 m); negligible along continental slope	intensified 7 km offshore of shelf break
She	coastal	surface intensified	intensified near inner shelf
SF	coastal	surface intensified	intensified near inner shelf
LRC	offshore	intensified at shelf break depth (150 m); negligible along bottom topography	intensified 5 km offshore of shelf break
SHR	shelf break	intensified along bottom topography (150-600 m)	intensified between shelf break and 10 km offshore
BLRB	outer shelf	surface intensified; negligible along bottom topography	intensified over mid-outer shelf to shelf break
KHRB	offshore	uniform offshore; negligible along continental slope	uniform 10 km offshore of shelf break; weak flow over outer shelf; negligible over inner shelf

40 m, generating a maximum zonal speed of $\sim 13 \text{ cm s}^{-1}$ (**She**). Stratification was varied over the entire depth, based on the equation for density provided in the original study. Initial fields are temperature (T):

$$T(z, t = 0) = 10 - 0.5 \exp\left(\frac{z}{110}\right)$$

and salinity (S):

$$S(z, t = 0) = 33 - 0.5 \exp\left(\frac{z}{110}\right),$$

where z is depth below 0.

To better understand the impact of open versus periodic boundary conditions, two scenarios with open alongshore boundaries were modelled. In these simulations, Orlandi radiation conditions were

applied across both alongshore boundaries and the offshore boundary. The first scenario (open boundary conditions, **OBC**) has the same geometry as the UW case, but both wind stress and body forcing were increased to recreate a similar zonal flow field as seen in the UW simulation. The second simulation (slanted topography, **ST**) used geometry that was similar to real world Blanes Canyon bathymetry (i.e. a slanted coastline and curvature within the canyon) (Figure F.4c). Forcing in this scenario was the same as the OBC case.

Two scenarios of constant surface forced (**SF**) flow were modelled, one forced by a wind stress and one forced with a surface body force applied to the upper 30 m. Results from these simulations were very similar, and will therefore be discussed as one example.

A uniform stratification (**US**) scenario was modelled with the same geometry and forcing as the UW scenario, but stratification from the Klinck-like case was used ($N=0.0016 \text{ s}^{-1}$ everywhere). Similarly, a high Burger number (**HB**) scenario was modelled. This case is exactly the same as the uniform stratification scenario, but now with a uniform N value of 0.005 s^{-1} .

Four final scenarios were modelled using various parameter specifications from previous simulations. To generate a simulation with low Rossby and χ values (**LRC**), SK forcing was applied, but with the same stratification as the HB case. The Skliris-like scenario was modelled again, but with a stronger forcing to generate a similar simulation but with a high Rossby number (**SHR**). Core case forcing and stratification was reduced to generate a simulation with low Rossby and Burger values (**BLRB**). The barotropic forcing was increased and run with core case stratification to produce high Rossby and Burger values (**KHRB**).

For all simulations with a wind forcing, the wind stress was linearly ramped over the initial model day, then held constant for model days 1-10 (wind magnitude, Table 2.4). All but one simulation with a body forcing (She) was linearly increased during the first model day. For these scenarios, a constant force was applied over model day 1-2 (body force magnitude; Table 2.4), followed by a linear decrease at the same rate as the increase, down to a constant value which was maintained to the end of the simulation (Table 2.4). For the She simulation, a body force was linearly ramped over the initial model day, then a constant body force was applied for model days 1-10.

The two simulations with constant forcing (She and SF) are not steady in time and experience a large time-dependence in their flow dynamics. However, none of the conclusions/trends discussed in this study are dependent on the results from these two simulations.

Table 2.4: Temporal variations in forcing for all model simulations

	Wind magnitude (τ ; N m^{-2})	Peak body force magnitude (m s^{-1})	Constant body force magnitude (m s^{-1})
UW	0.0626	0.315	0.047
OW	0.0626 (offshore) 0.0376 (onshore)	0.315	0.063
OBC	0.13	0.53	0.133
ST	0.13	0.53	0.133
KL	-	0.06	0.024
SK	-	0.09	0.029
US	0.0626	0.315	0.079
HB	0.0626	0.315	0.047
She*	-	0.18	-
SF	0.0626	-	-
LRC	-	0.09	0.032
SHR	-	0.3	0.105
BLRB	0.0313	0.15	0.023
KHRB	-	0.18	0.063

2.1.4 Result calculations

Transport calculations were used to estimate the volume of water exchanged vertically and horizontally in the domain. An initial plane along the canyon axis divides the canyon into an upstream and downstream half (Figure 2.1). Zonal flux was calculated across this plane from surface to shelf break depth, and from the canyon mouth to coastal boundary (U3). Meridional flux was calculated across two planes that lie along the canyon mouth; one in the upstream (V2) and one in the downstream (V3). Again, flux was calculated from surface to shelf break depth. Finally, two planes were used to calculate vertical flux at shelf break depth. These planes extend from the canyon head to canyon mouth and split across the canyon axis (upstream = W1, downstream = W2). Net vertical flux was calculated by summing flux across these two planes. Flux across all planes was found by multiplying velocity of each grid cell by area of each grid cell and summing over the entire plane.

To better understand overall flow patterns, float particles were introduced at various positions in the model domain. Particle trajectories were tracked from model days 2 through 10, with new particle positions collected every six hours. The numerical model printed variable outputs twice a day, a fourth-order Runge-Kutta algorithm was then applied to interpolate particle movement more frequently [Dawe and Allen, 2010].

Relative vorticity in the basin can be expressed as:

$$\zeta = \frac{\delta V}{\delta x} - \frac{\delta U}{\delta y},$$

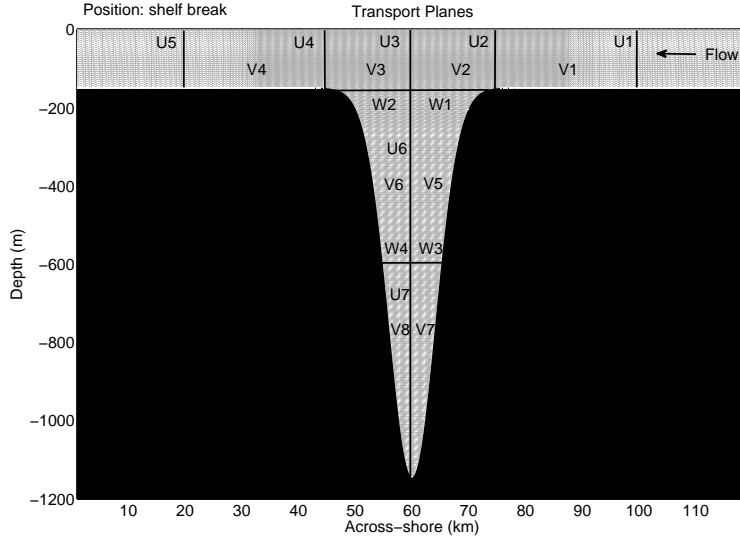


Figure 2.1: Planes used for transport calculations.

where ζ is the vertical component of vorticity, V is the meridional velocity, and U is zonal velocity. Absolute vorticity was measured as the relative vorticity divided by Coriolis parameter, f .

Average zonal velocity across the canyon axis at shelf break depth (150 m) was used to calculate a second Rossby number ($R_{\bar{U}_{can}}$). This velocity is calculated as:

$$\bar{U}_{can} = \frac{\sum U(y) \Delta y}{L},$$

where U is taken as the zonal velocity in each meridional grid point that lies along the canyon axis, and Δy is the horizontal distance the zonal velocity is applied. A canyon Rossby number was calculated as:

$$R_{\bar{U}_{can}} = \frac{\bar{U}_{can}}{fL}.$$

Density was calculated for all model simulations as average density in the canyon across the shelf break plane (W1 and W2). This value was averaged during the approximate advection dominated phase (averaged from model day 4-10). Average density was subtracted from initial density at shelf break depth to give an average density anomaly in the canyon.

Changes in density difference within the canyon relative to away from the canyon were determined by calculating a density difference anomaly. This anomaly was found by subtracting a background density difference (calculated as a 5 grid point average along the downstream boundary) from the difference at grid points of similar isobaths:

$$\rho_{anom} = \rho_{difference}(x_i, y_i, z) - \rho_{boundary}(y_i, z),$$

where x_i and y_i are alongshore and cross-shore points (respectively) that are ± 5 m of the isobath used to calculate the background density difference ($\rho_{boundary}(y_i, z)$).

Nitrate concentration was used as a passive tracer in the model. An average nitrate concentration was also calculated as the average nitrate value in the canyon across the shelf break plane (W1 and W2) during the advection dominant phase (model days 4-10). The average nitrate concentration is subtracted from the initial nitrate concentration at shelf break depth to give an average nitrate anomaly in the canyon.

2.2 Results

2.2.1 Flow evolution

All model scenarios show an initial time-dependent response to model forcing, similar to that described by Allen and Durrieu de Madron [2009], which lasts approximately two to three days (Figure 2.2; Figure F.1). During this phase, zonal and vertical flux exhibit a negative ramping everywhere in the domain. In all but two simulations, vertical flux across the downstream plane (W2; Figure 2.1) reverses at approximately day 1, and continues towards a maximum positive value by day 2-2.5. In these simulations, magnitude of meridional flux over the canyon gently increases across both planes, being positive (onshore) in the upstream (V2; Figure 2.1) and negative (offshore) in the downstream (V3; Figure 2.1) until reaching a maximum near the end of the time-dependent phase. In the simulations with a coastal jet (She and SF; Figure F.1h and F.1i, respectively), vertical flux is downwards across both the upstream and downstream planes until day 1. After this, negative flux across the downstream plane weakens in time, while negative flux across the upstream plane continues to strengthen. For these scenarios, upstream onshore flux and downstream offshore flux strengthen during the model simulation.

The time-dependent phase is followed by an advection dominated phase. During this phase, zonal flux stays within approximately 2-17% of the maximum value reached during the time-dependent phase for most simulations. Meridional flux also gently fluctuates, always being positive in the upstream and negative in the downstream for all model scenarios. The two surface forced simulations (She and SF) show a zonal flux that continuously increases during the model simulation, with a final zonal flux that is approximately 50% stronger than flux at the end of the time-dependent phase. This indicates neither scenario may be reaching an advection dominated phase.

Vertical flux time dependence varies between model simulations, with 3 primary patterns emerging (Figure F.1). Firstly, vertical flux varies between positive and negative transport over both the upstream and downstream plane of the canyon, with flux values being roughly the same in the upstream/downstream. This pattern is seen in the UW and OW simulations. Secondly, flux across the

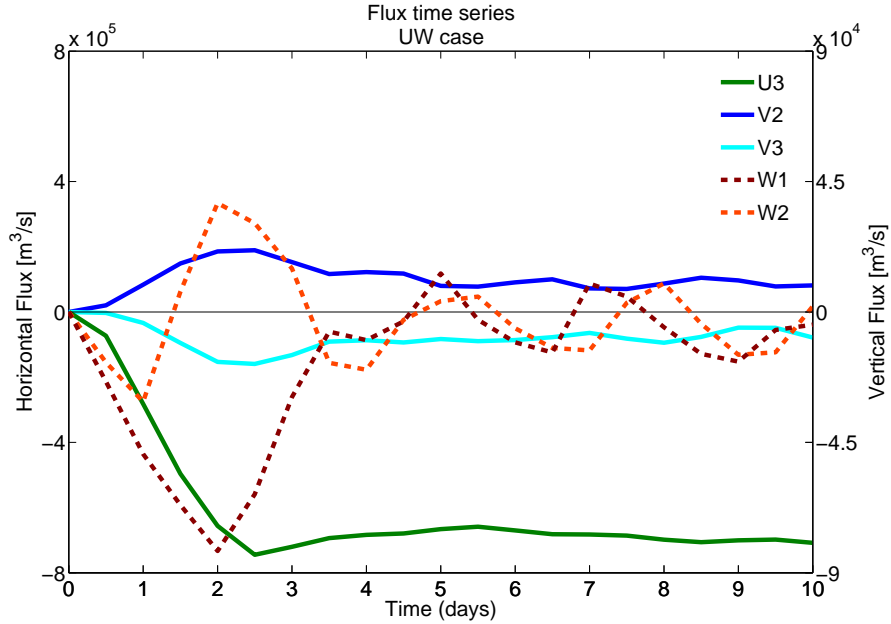


Figure 2.2: Time series of horizontal and vertical flux directly over the canyon for core (UW) simulation. U3 indicates zonal flux across the canyon axis (from canyon head to canyon mouth). V2 and V3 are meridional flux along the canyon mouth from the upstream rim to canyon axis, and from the canyon axis to downstream rim, respectively. All horizontal fluxes are measured from surface to shelf break depth. W2 and W3 are vertical flux across the shelf break depth plane (150 m) everywhere within the canyon, from the upstream rim to canyon axis and from the canyon axis to downstream rim, respectively. Negative U, V, and W values indicate westward, offshore, and downwards fluxes.

upstream plane is mirrored across the downstream plane, i.e. as magnitude across one plane increases, magnitude across the other plane increases well. In 6 simulations (ST, KL, SK, US, HB, SHR) this pattern occurs with upstream transport always positive and downstream transport always negative. In 4 runs (OBC, LRC, BLRB, KHRB) the above pattern occurs, but flux across the upstream/downstream planes does cross between positive and negative values during model days 4-6. Thirdly, simulations with a coastal jet (She and SF) exhibit strengthening negative flow across the upstream plane and weakening negative flow across the downstream plane. In the She case, flux across the downstream plane becomes positive around model day 4. In the SF case, flux over the upstream plane begins to weaken around model day 7.

The core simulation was extended by 10 more model days to determine how steady flux is in time (Appendix D). Meridional and vertical fluxes (V2, V3, W1 and W2) were averaged from days 10-20 and values vary approximately 90% between the core (UW) and extended core simulations (zonal flux across the U3 plane varied only 4% between the simulations). The steady zonal current developed an instability around day 12, causing fluctuations in horizontal and vertical flux. To ensure aliasing is not occurring

with 12-hour model output, another 10-day UW simulation was run with model output written every 3 hours (Appendix E). Small differences in flux estimates are seen during the time-dependent phase. Differences during the advection-dominant phase are less than 10%.

2.2.2 Circulation in the canyon

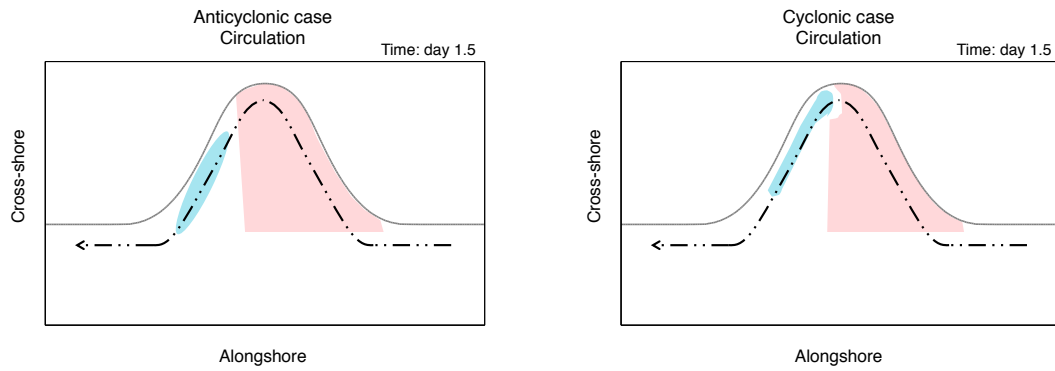
Model simulations exhibit three types of horizontal circulation: 1) formation of an anticyclonic eddy within the canyon, 2) cyclonic circulation everywhere within the canyon and 3) weak circulation everywhere within the canyon. The evolution of the first two horizontal flow patterns are discussed below. Firstly, the anticyclonic circulation is detailed, followed by a description of the cyclonic circulation.

For high Burger number simulations (particularly, UW, OW, OBC, ST, HB, KHRB) horizontal flow during the time-dependent phase is cyclonic over the canyon (Figure 2.3a, left). Towards the end of this phase, flow along the downstream rim becomes stronger relative to the upstream rim (Figure 2.3b, left). After one more model day (by day 3), flow in the canyon head becomes anticyclonic and this pattern persists for the remainder of the model simulation (Figure 2.3c, left). Vertical velocity during the first day of simulation is negative everywhere in the canyon, and strongest in the upstream. As the flow evolves, a region of positive vertical velocity appears in the downstream half of the canyon and moves toward the downstream corner of the canyon mouth.

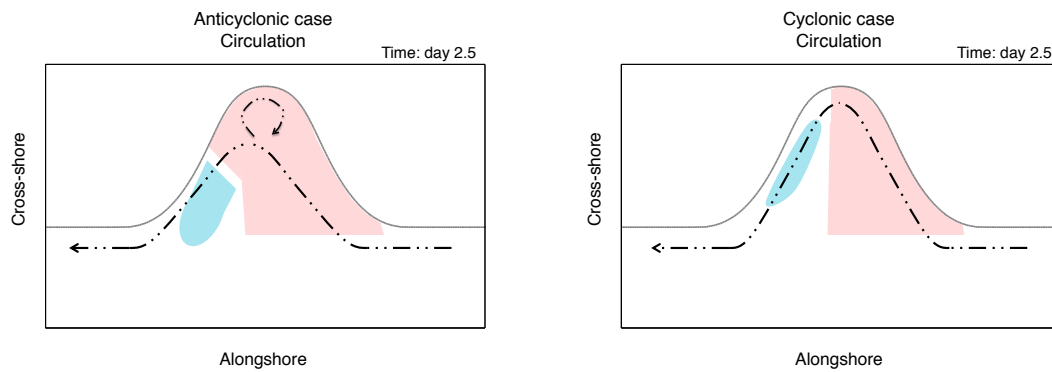
During the time-dependent phase, flow becomes faster over the canyon axis and impinges on the downstream wall. Thus, the shelf break jet splits as it reaches the downstream rim. Shoreward of the jet, an anticyclonic eddy forms in the canyon and persists during the advection dominated phase (Figure 2.4a).

Approximately 20 particle drifters were used to trace circulation around the anticyclonic eddy, with 5 particles used to highlight patterns in various regions (Figure 2.5). Particles flowing over the upstream rim, near shelf break depth, interact with the anticyclonic eddy. After passing the upstream rim (between 140-150 m depth), particles that fall to depths of 200 m or deeper are trapped in the eddy. Particles that drop to depths shallower than 200 m make one loop inside the eddy, then ascend over the downstream rim. It takes all particles approximately 2.5 days to make one loop around the eddy. Particles initiated further upstream of the canyon do not get caught in the eddy after dropping into the canyon. Instead, these particles make a slight descent into the canyon and move slightly onshore, then cross the canyon axis and continue offshore, ascending along the downstream rim.

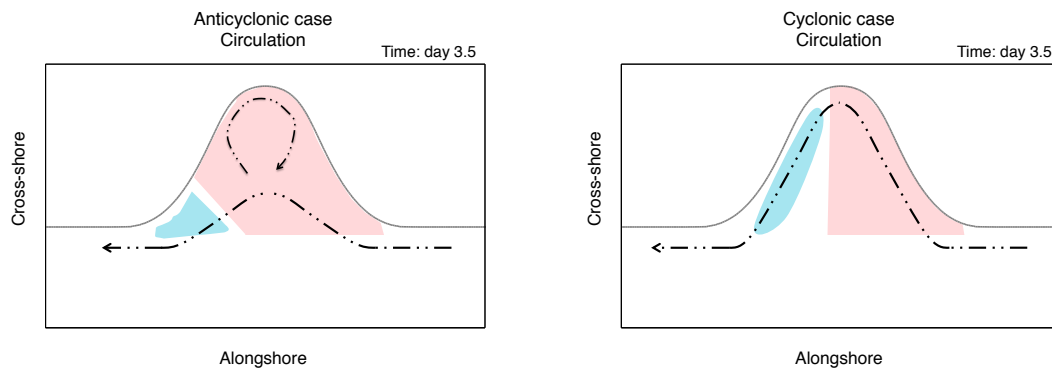
For low Burger number simulations (particularly, KL, SK, US, SHR), the cyclonic circulation that forms during the time-dependent phase strengthens as zonal flow accelerates and remains cyclonic (Figure 2.3, right and 2.4b). Similar to the cases with anticyclonic circulation, vertical flow is negative



(a) day 1.5 circulation

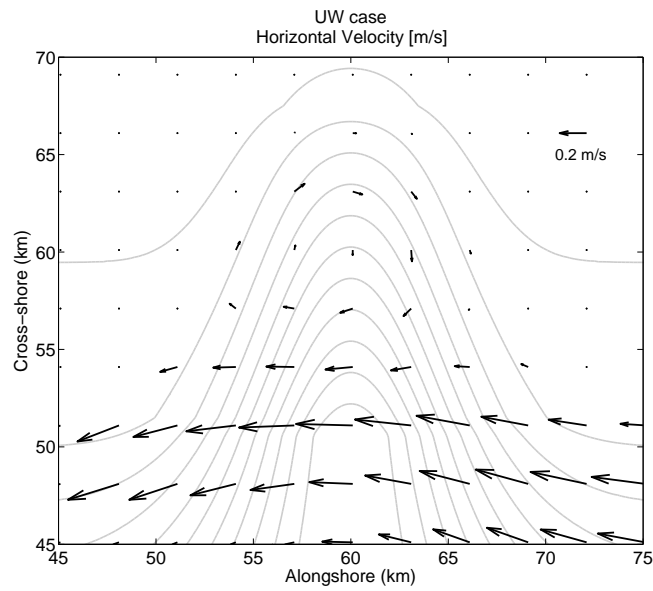


(b) day 2.5 circulation

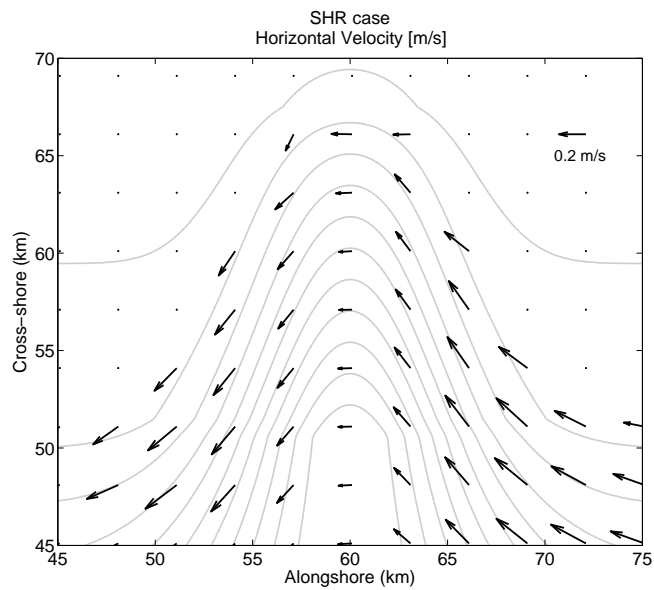


(c) day 3.5 circulation

Figure 2.3: Horizontal and vertical circulation at shelf break depth during the time-dependent phase on (a) day 1.5, (b) day 2.5, and (c) day 3.5. Pink shading indicates downwards velocity and teal shading indicates upwards velocity. Circulation for a simulations with anticyclonic circulation (left) and cyclonic circulation (right) are shown.



(a) Anticyclonic circulation



(b) Cyclonic circulation

Figure 2.4: Horizontal velocity vectors at shelf break depth (150 m) in (a) simulation with anticyclonic circulation (UW) and (b) simulation with cyclonic circulation (SHR). Vectors are averaged over a 3 model day period during the advection phase (model day 5-8).

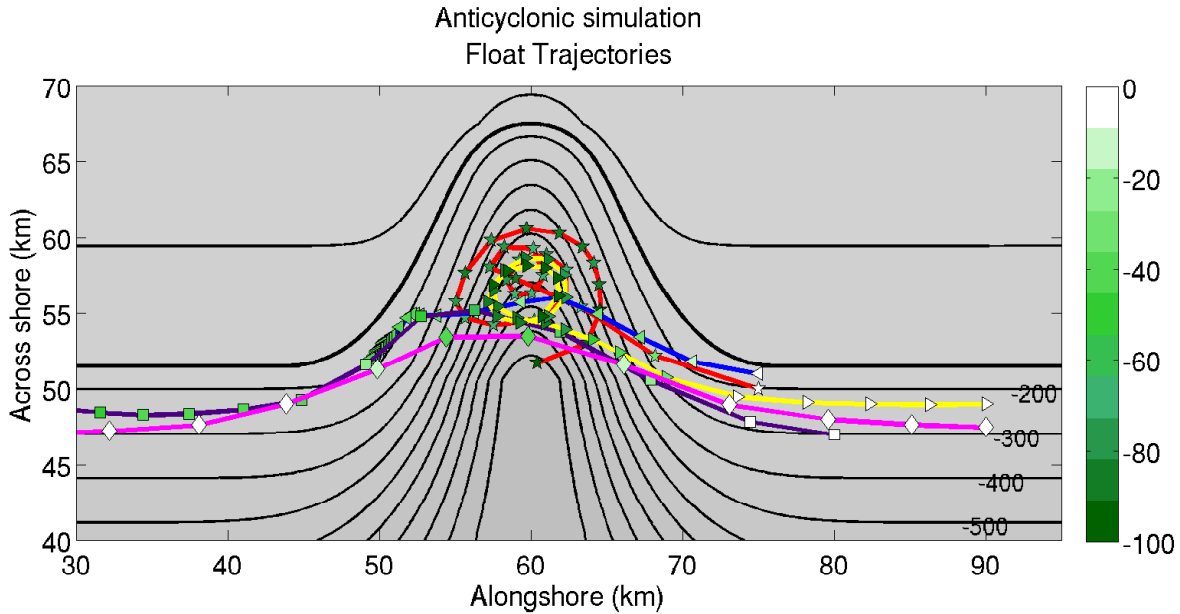


Figure 2.5: Trajectory for shelf break drifter particles released in a simulation with anticyclonic circulation; 5 (out of 20) sample particles are plotted. Trajectories are plotted for model days 2-10. Scale bar and color of individual markers indicates vertical depth change from initial marker depth (first marker in the upstream). Initial particle depths: \star and red line = -150 m, \square and purple line = -140 m, \diamond and pink line = -150 m, \triangleleft and blue line = -150 m, \triangleright and yellow line = -195 m.

everywhere within the canyon and strongest in the upstream. However, as the flow evolves, positive vertical velocity begins to appear in the downstream half of the canyon where it remains (it does not get pushed offshore) (Figure 2.3a-c, left). For these cases, horizontal flow is strongest along the canyon walls and weaker across the canyon axis.

Twenty particle drifters in these simulations highlight the cyclonic circulation seen in the canyon (Figure 2.6). As particles cross the upstream rim, they descend and move onshore. This is followed by an ascent and offshore movement after crossing the canyon axis. Particles entering the canyon near the canyon mouth, or offshore of the canyon mouth (at 130-200 m depth), experience a small (less than 20 m) ascent as they cross the upstream rim and then approximately 50 m before reaching the canyon axis. These particles slowly ascend after crossing the canyon axis.

For the purposes of this study, results focus on flow dynamics during the advection dominant phase. Results in the following sections are time-averaged model output. Based on oscillations in the vertical

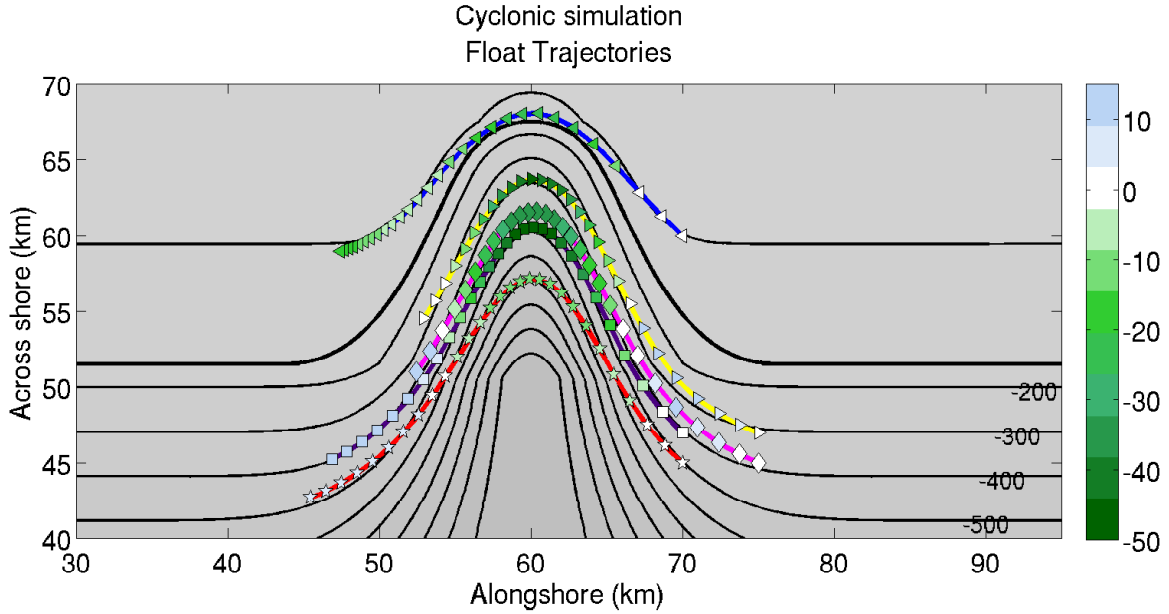


Figure 2.6: Trajectory for outer shelf drifter particles released in a simulation with cyclonic circulation; 5 (out of 20) sample particles are plotted. Trajectories are plotted for model days 2-10. Scale bar and color of individual markers indicates vertical depth change from initial marker depth (first marker in the upstream). Initial particle depths: \star and red line = -77 m, \square and purple line = -200 m, \diamond and pink line = -150 m, \triangleleft and blue line = -60 m, \triangleright and yellow line = -144 m.

flux time series (Figure 2.2), results are averaged from model days 5-8.

2.2.3 Comparison to previous studies

Current simulations reproduced canyon circulation features seen in previous studies (Table 1.1). Klinck [1996] was reproduced in the KL simulation. In this low Rossby number, low Burger number and low $|\chi|$ simulation, the cyclonic circulation, antisymmetrical vertical velocity and density change pattern (positive density anomaly outside the canyon mouth) seen in the original study was reproduced in the current model. Similarly, Skliris et al., [2001; 2002] was replicated in the SK simulation. Cyclonic circulation, antisymmetrical vertical velocity and positive density anomalies away from the canyon were reproduced in this low Rossby number, low Burger number, and intermediate $|\chi|$ simulation.

She and Klinck [2000] was mostly reproduced in the She simulation. In this low Rossby number, intermediate Burger number and intermediate $|\chi|$ simulation, net downwards vertical velocity was reproduced.

However, a weak cyclonic circulation was seen at all depths in the canyon. This is different from the original study, which saw anticyclonic circulation over the canyon and cyclonic circulation at 300 m and below. Multiple scenarios with varying Rossby, Burger, and $|\chi|$ values (UW, OW, OBC, ST, LRC, SHR) exhibit anticyclonic vorticity at shelf break depth and cyclonic vorticity deeper in the canyon, similar to that seen in She and Klinck [2000]. Flexas et al., [2008] was reproduced in the UW and OW simulations. In these high Rossby number, high Burger number, and high $|\chi|$ simulations, the anticyclonic circulation and periods of net positive vertical velocity similar to that seen in the observations were replicated.

2.2.4 Vorticity in the canyon

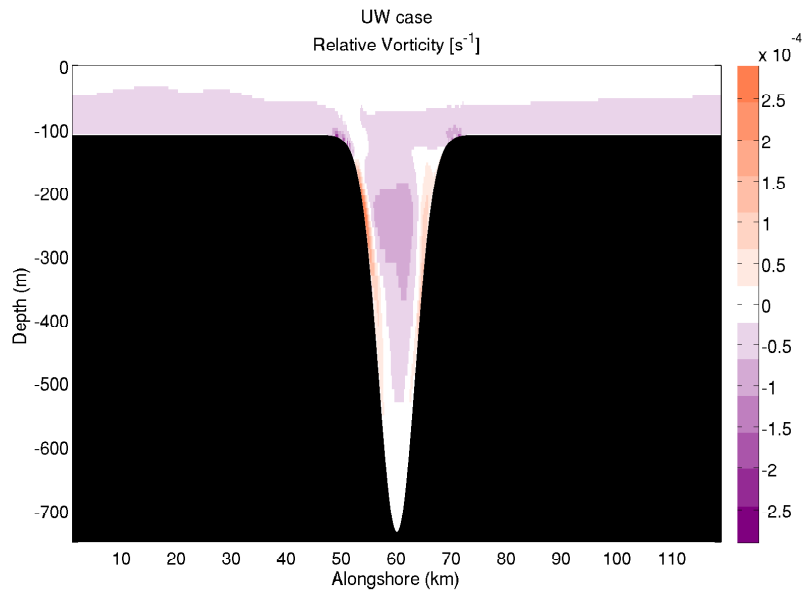
As previously discussed, all model scenarios either form an anticyclonic eddy in the canyon after the time-dependent phase (Figure 2.4a), or have cyclonic circulation in the canyon throughout model simulation (Figure 2.4b). Looking at shelf break depth circulation, 6 simulations exhibit an anticyclonic eddy, 4 simulations show cyclonic circulation, and 4 other simulations show weak circulation at this depth.

Table 2.5: Absolute vorticity and canyon circulation for all model simulations

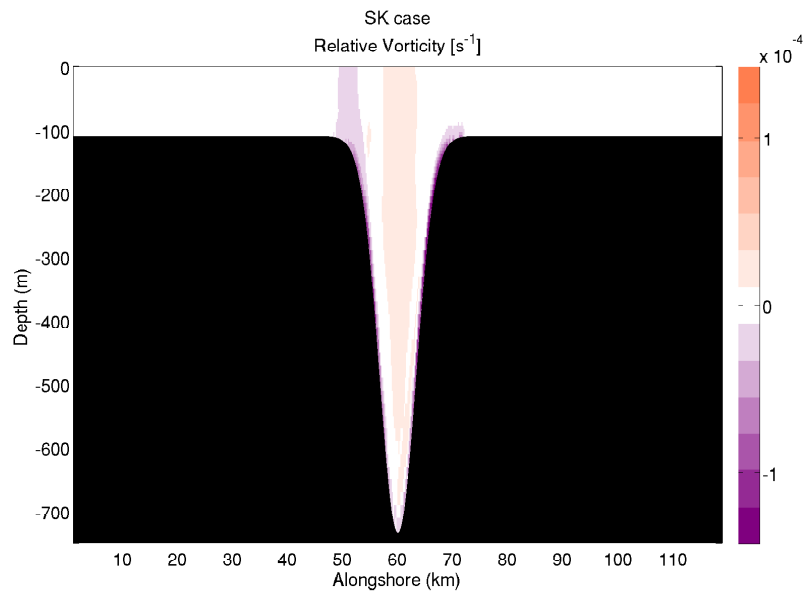
	Absolute Vorticity (1/f)	Canyon Circulation	Shelf break circulation
UW	-0.55	Anticyclonic (50-500 m)	Anticyclonic
OW	-0.54	Anticyclonic (0-500 m)	Anticyclonic
OBC	-0.50	Anticyclonic (75-400 m)	Anticyclonic
ST	-0.40	Anticyclonic (150-450 m)	Anticyclonic
KL	0.2	Cyclonic (0-400 m)	Cyclonic
SK	0.34	Cyclonic (all depths)	Cyclonic
US	0.97	Cyclonic (all depths)	Cyclonic
HB	-0.26	Cyclonic (200-500 m)	Anticyclonic
She	0.08	Cyclonic (all depths)	Weak
SF	0.07	Cyclonic (all depths)	Weak
LRC	-0.09	Anticyclonic (100-350 m)	Weak
SHR	0.71	Cyclonic (all depths)	Cyclonic
BLRB	-0.1	Anticyclonic (100-350 m)	Weak
KHRB	-0.14	Anticyclonic (100-300 m)	Anticyclonic

*Absolute vorticity is taken as maximum vorticity in the canyon head, away from canyon rims, at shelf break depth.

Simulations with anticyclonic circulation display negative vorticity within the canyon, but opposing positive vorticity along the canyon walls (Figure 2.7a). Simulations with cyclonic circulation have the opposite feature, positive vorticity within the canyon, but negative vorticity along canyon walls (Figure 2.7b). This reversal of vorticity along bottom topography is due to friction between water parcels and canyon walls. The simulation in which the anticyclonic eddy appears only at a depth below the shelf



(a) negative in canyon vorticity



(b) positive in canyon vorticity

Figure 2.7: Cross-section of vorticity at mid-canyon in (a) simulation exhibiting negative vorticity (UW) and (b) simulation exhibiting positive vorticity (SK).

break (HB) has negative vorticity at shelf break depth (Table 2.5).

2.2.5 Upwelling in a downwelling canyon

Vertical velocity

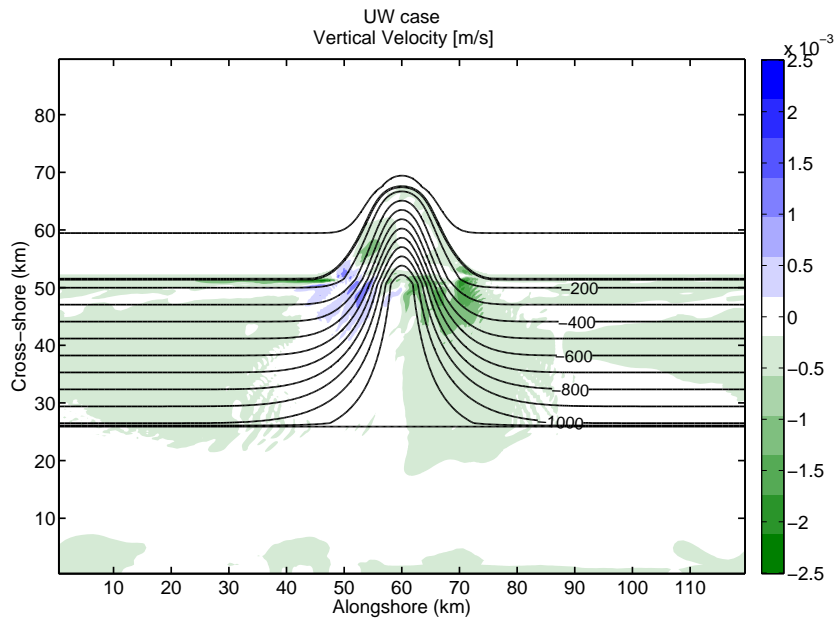
Two main flow patterns are seen in plane views of vertical velocity. In the first pattern, enhanced downwards (upwards) velocity is confined to the upstream (downstream) corner of the canyon mouth at shelf break depth (Figure 2.8a). This pattern occurs in simulations with weak or negative vorticity at shelf break depth (Table 2.5). One exception is the HB scenario, which exhibits varying positive and negative vertical velocity patterns everywhere within the canyon.

In the second vertical flow pattern, vertical velocity presents a more antisymmetric pattern, similar to that seen in previous studies [Klinck, 1996; Skliris et al., 2001; 2002]. In these simulations, regions of positive and negative vertical velocity are split along the canyon axis from canyon head to canyon mouth, with negative velocity in the upstream and positive velocity in the downstream (Figure 2.8b). This pattern occurs in simulations with strong, cyclonic vorticity (Table 2.5).

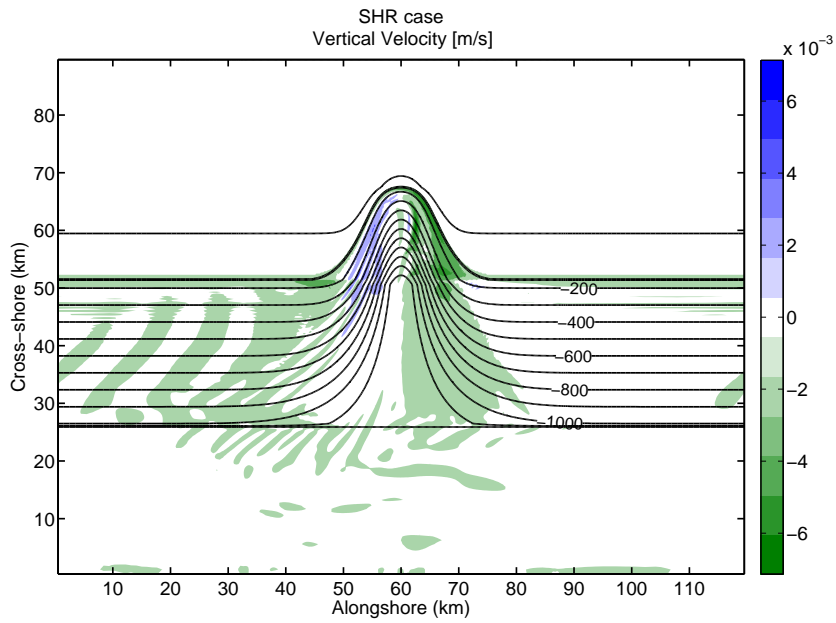
In all model scenarios, regions of enhanced upstream negative velocity are stronger than downstream regions of positive velocity. All simulations also exhibit a background negative velocity in regions away from the canyon.

Using the 12-hourly flux time series, periods of positive vertical flux across 3 planes (100 m, 150 m, and 600 m) in the canyon (i.e. everywhere between canyon walls from the canyon head to mouth) were calculated over the 10 day model period (Figure 2.9). Net upward flux does occur in various downwelling canyon simulations. Note, only 4 scenarios do not see net upwelling at any time (She, SF, SHR, BLRB). Net upwards flux most commonly occurs across the 600 m plane, and least often across the 100 m plane. Periods of net upwards flux mostly occur during the advection dominated phase. The longest occurrence of net upwards flux appears in the OBC simulation, there is a period of net upwards flux that lasts 2.5 model days. Overall, the OBC scenario exhibits the most occurrences of net upwards flux across the 150 m and 600 m planes.

To understand the three-dimensional movement of flow in and around the canyon, particle drifters were initiated upstream of the canyon at varying depths in one of the core simulations (UW case); 70 particles were released near and slightly offshore of the canyon (Figure 2.10). Particles in the upper 20 m experience relatively no change in depth as they cross over and downstream of the canyon. Particles moving over the canyon head descend over the upstream rim and ascend over the downstream with a



(a) enhanced vertical velocity along canyon mouth



(b) antisymmetrical vertical velocity in canyon

Figure 2.8: Vertical velocity at shelf break depth (150 m) in (a) simulation with enhanced vertical velocity along canyon mouth (UW) and (b) antisymmetrical vertical velocity along canyon axis (SHR).

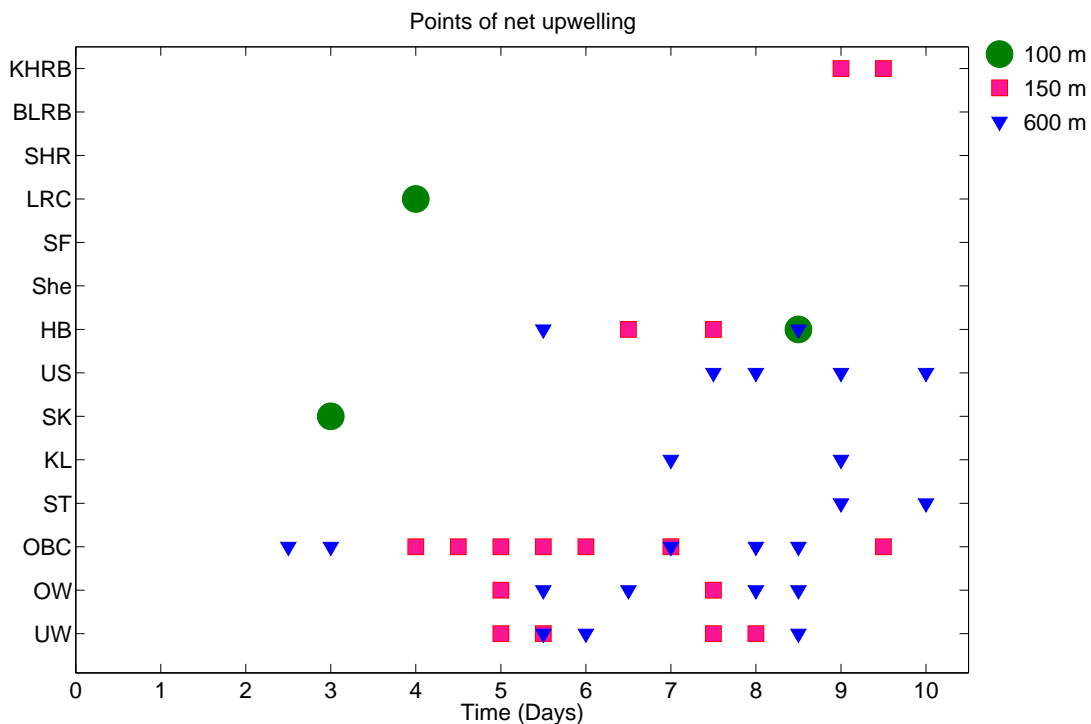


Figure 2.9: Times of net upwards flux across 3 vertical planes for all model simulations. Net upwards flux is plotted if larger than a minimum value of $1000 \text{ m}^3\text{s}^{-1}$.

net offshore and downward movement from their original position. Over the outer shelf (depths between 30-120 m), particles move fastest, descending along the upstream rim, lifting along the canyon axis, and moving over the downstream rim. Upon exiting the canyon, these particles are further offshore and deeper. At these depths, particles move furthest downstream for all particles in the domain. Downstream and away from the canyon, these particles continue to move slightly offshore and deeper with time. Particles near shelf break depth and below (120-250 m), that are not trapped in the anticyclonic eddy, move similar to those over the outer shelf, but slower. Around 250 m to bottom depth, particles descend over the upstream rim, ascend over the downstream rim, and continue moving downstream. Particles at these depths descend much deeper into the canyon relative to shallower particles, due to weaker stratification at these depths.

Particle trajectories are affected far offshore of the canyon (not shown). Trajectories curve shoreward when passing the upstream portion of the canyon and offshore along the downstream region. Curvature of trajectory paths is seen in particles as far away as the offshore boundary. The degree of curvature and change in depth decreases offshore of the canyon; particle velocity also decreases further offshore.

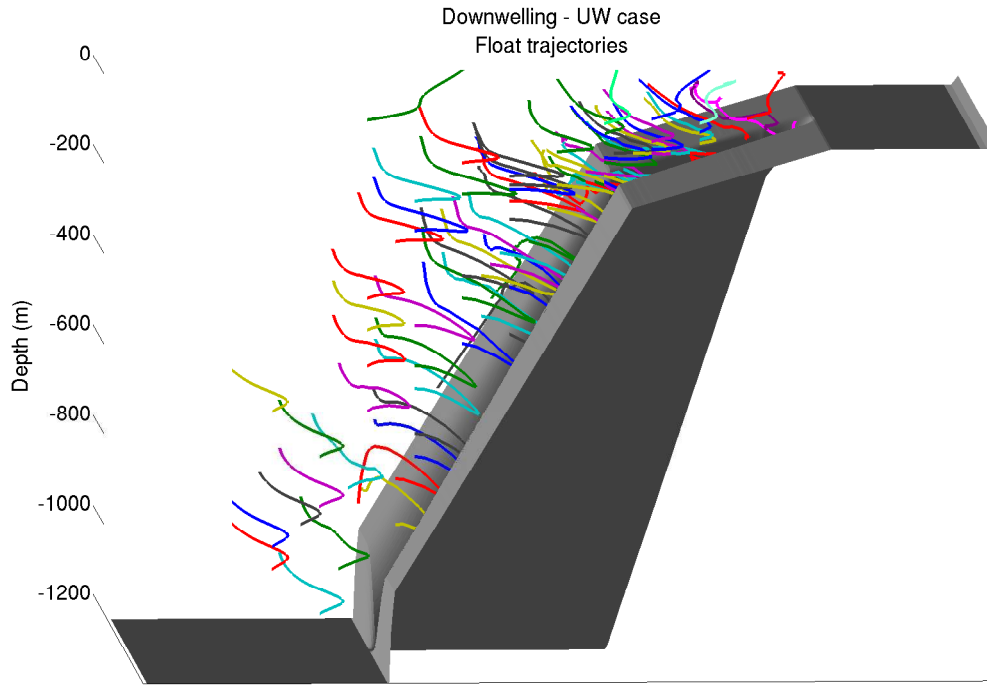
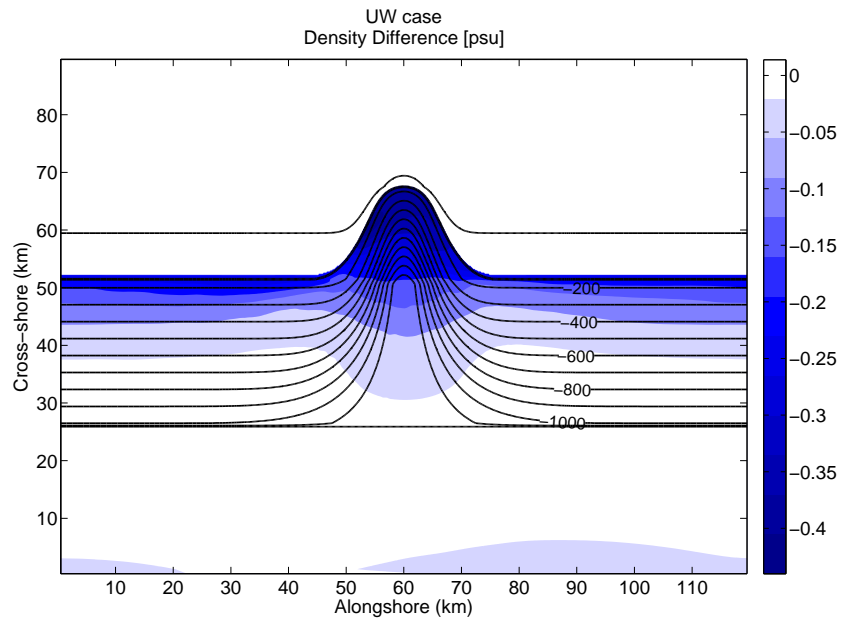


Figure 2.10: Particle trajectories for all depths in a basic simulation (UW). This is a 3-dimensional view of the model domain. The view is from the upstream boundary looking down at the canyon and towards the downstream. The coast is to the right and open ocean to the left. Particles were initiated approximately 5 km upstream of upstream canyon rim. Particles generally strongly descend and then weakly ascend as they travel past the canyon (flow is into the page).

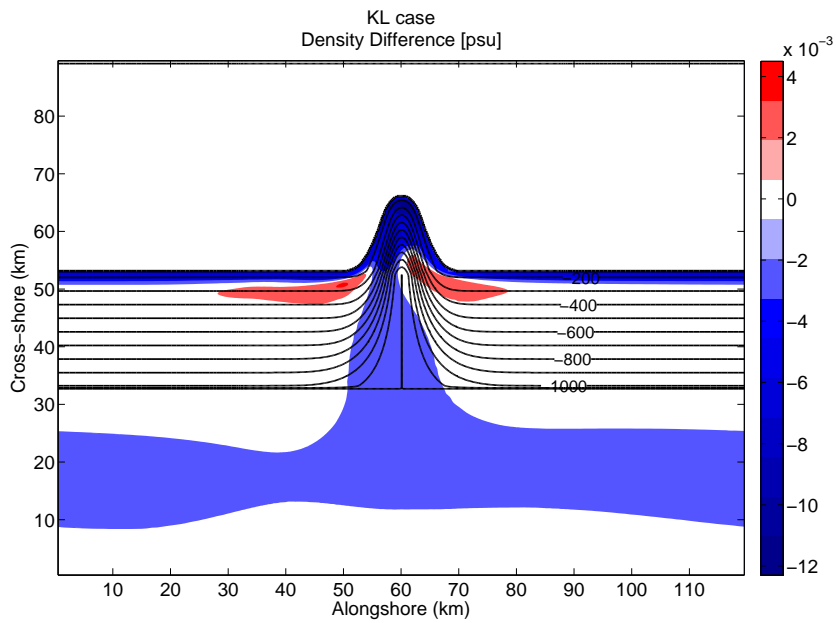
Density anomaly

Density anomalies were calculated as density variations (averaged over days 5-8) relative to initial density profiles. Similar to vertical velocity, two distinct anomaly patterns appear. In the first pattern, density anomaly is negative everywhere in the canyon domain (Figure 2.11a). At all depths, anomalies are strongest along bottom topography and weaken towards the offshore. This pattern is seen in simulations with a coastal or outer shelf jet (UW, OW, OBC, ST, She, SF, BLRB; Table 2.6).

In the second pattern, there are strong negative anomalies along bottom topography, but there are also positive anomalies away from the canyon (Figure 2.11b). This pattern is seen in simulations with a shelf break or offshore jet (KL, SK, US, HB, LRC, SHR, KHRB); the depth range of positive density anomalies varies (Table 2.6). For the majority of these simulations, positive anomalies do not extend down to shelf break depth (SK, US, HB, SHR, KHRB), but in two simulations positive anomalies do extend down to shelf break depth and below (KL, LRC).



(a) everywhere negative density anomalies



(b) positive density anomalies near canyon

Figure 2.11: Density anomaly at shelf break depth (150 m) in (a) simulation with pattern 1: negative density anomalies at all depths (UW) and (b) simulation with pattern 2: positive density anomalies near the canyon (KL).

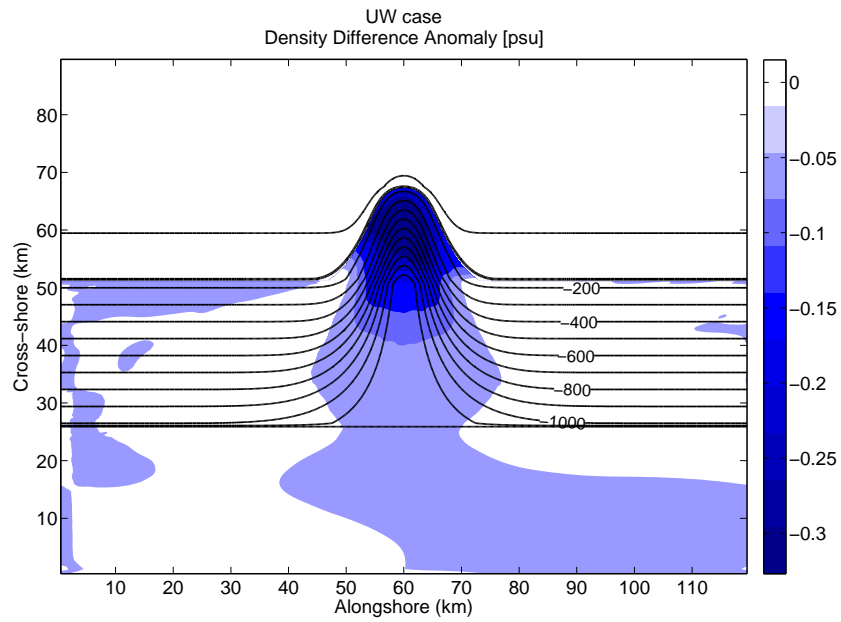
Table 2.6: Positive density anomaly depth range for all model simulations. Pattern 1 density anomalies had no positive values. Pattern 2 density anomalies had positive values.

	Depth of positive density anomaly	Jet location
UW	-	outer shelf
OW	-	outer shelf
OBC	-	outer shelf
ST	-	outer shelf
KL	surface to 200 m	offshore
SK	surface to 120 m	shelf break
US	surface to 100 m	offshore
HB	surface to 100 m	offshore
She	-	coastal
SF	-	coastal
LRC	surface to 150 m	offshore
SHR	surface to 100 m	shelf break
BLRB	-	outer shelf
KHRB	surface to 120 m	offshore

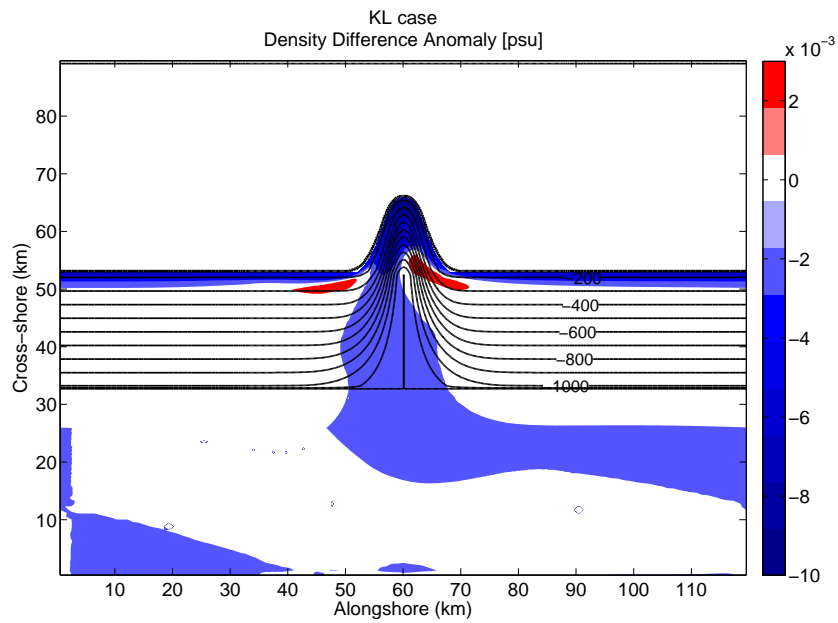
Density difference anomaly

As shown in vertical velocity and density difference, regions with downwelling canyons exhibit a background downwelling flow, with both negative vertical velocity and negative density changes away from the canyon region. To determine what extra effect a canyon has in a downwelling region, a density difference anomaly was calculated.

Downwards density advection is enhanced in all canyon scenarios (Figure 2.12). Two patterns are seen, however, these patterns do not line up exactly with density anomaly patterns. In the first pattern, downwards density advection is strongest in the canyon head and along the canyon axis (Figure 2.12a); this pattern is seen in half (7) of the simulations (UW, OW, OBC, ST, HB, SF and LRC). In the second pattern, downwards density advection is strongest along bottom topography (Figure 2.12b); this pattern is seen in the other half of the simulations (KL, SK, US, She, SHR, BLRB and KHRB). Independent of density advection pattern, 8 simulations exhibit positive density difference anomalies away from the canyon. In these cases, weaker downwelling (positive density difference anomalies) occurs along either the upstream (OW) or downstream (SF, LRC and BLRB) corner of the canyon mouth, or along both corners of the canyon mouth (KL, US, She and SHR).



(a) Enhanced downwelling everywhere in canyon



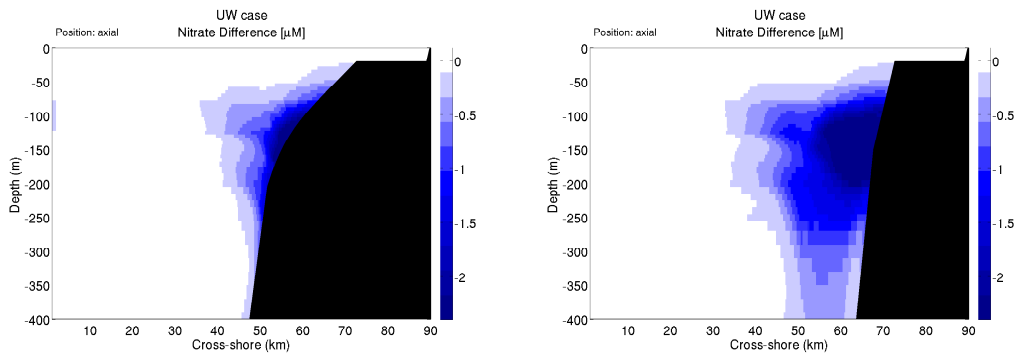
(b) Enhanced downwelling along canyon head

Figure 2.12: Density difference anomaly at shelf break depth (150 m) in (a) simulation with pattern 1: enhanced density advection everywhere in the model domain (UW) and (b) simulation with pattern 2: enhanced downwelling within the canyon and weaker downwelling near the canyon mouth (KL).

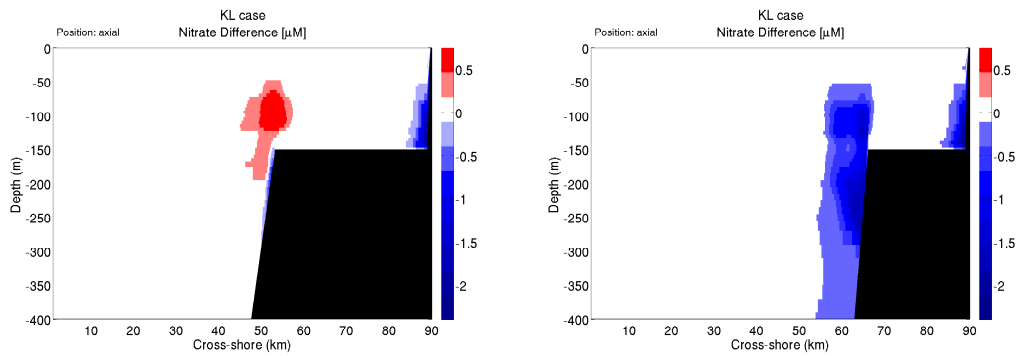
2.2.6 Nitrate anomaly

All model simulations included a passive tracer (nitrate concentration) that was initialized with the same vertical variation for all runs. This provided one parameter that was the same in all simulations, allowing for better comparisons between model runs. Again, anomalies were calculated as changes between the initial nitrate profile and the day 5-8 averaged model output nitrate profile.

Similar to vertical velocity and density anomalies, two patterns appear. With the exception of 2 cases (OBC and ST), simulations that exhibit the pattern 1 density anomaly exhibit the same pattern for nitrate anomaly; negative everywhere within the canyon and strongest along bottom topography (Figure 2.13a). Similarly, simulations that show pattern 2 density anomalies also exhibit negative nitrate anomalies along bottom topography and positive anomalies a few kilometers offshore (Figure 2.13b). The 2 simulations with open boundary conditions (OBC and ST) exhibit a pattern similar to pattern 2, however positive nitrate anomalies occur 5-20 km offshore (Figure F.7c-f).



(a) negative nitrate anomalies



(b) positive nitrate anomalies away from canyon

Figure 2.13: Nitrate anomaly 10 km upstream of canyon axis (left) and along canyon axis (right) in (a) simulation with pattern 1: negative nitrate anomalies at all depths (UW) and (b) simulation with pattern 2: positive nitrate anomalies near the canyon (KL).

2.3 Discussion

2.3.1 Upwelling in downwelling canyons

There are various ways in which upwelling can be defined. Firstly, upwelling can be characterized as the net upwards movement of water in a region. Secondly, upwelling can be described as the net onshore movement of dense, cold (usually nutrient-rich) deep ocean water to the shallower coastal ocean. Coastal upwelling typically involves both processes working together, i.e. as surface waters are pushed offshore, deep ocean water is brought up from the depth to replenish surface waters along the coast. However, upwelling along the coast does not always occur following this same process.

During two observational cruises around Blanes Canyon, Flexas et al., [2008] used velocity and hydrographic samples to calculate vertical flux in the canyon. The authors estimated that at approximately 100 m depth and shallower, vertical velocities were negative; below the thermocline (~ 100 -200 m depth), vertical velocities were positive. The authors concluded that upwelling did occur in Blanes Canyon, with a maximum near the shelf break depth and extending between 100-200 m. Arduin et al., [1999] modelled an upwelling cell beneath a trapped anticyclonic eddy. In this study, offshore deep waters from 300-500 m depth were lifted at the canyon wall and pulled out to the open ocean in the 200-300 m layer.

Plan view images of time-averaged vertical velocity in the current simulations do not directly reveal net upward movement of water in any canyon scenarios. All simulations do show regions of both upwards and downwards vertical velocity, however, downwards motion appears to always be dominant. Results of snapshots of net vertical velocity across 3 planes indicate that net upwards displacement of water does occur in the majority of simulations (Figure 2.9). In most cases this upwards displacement is brief and commonly occurs at depth. However, the OBC case shows an extended period of net upwards velocity across the 150 m plane from model day 4-6, the beginning of the advection dominated phase. This period of net upwards velocity at shelf break depth can be compared to observations in Flexas et al. [2008]. In the current study, a period of net upwelling may be occurring, but the time-mean flow of the advection phase indicates an overall net downwelling.

The prevalence of upwards displacement across the 600 m plane indicates a possible upwelling cell similar to Arduin et al., [1999], in which deep water is upwelled along canyon walls, but returns to the offshore before crossing shelf break depth. Increased stratification has been found to reduce vertical transport [Klinck, 1996]. For all current simulations, stratification is weaker with depth, which is likely the reason vertical exchange shows more variation at depth. The irregular occurrences of net upwards displacement across vertical planes, even under semi-steady circulation, indicates observational studies

may not be detecting the time-mean flow dynamics occurring in submarine canyons.

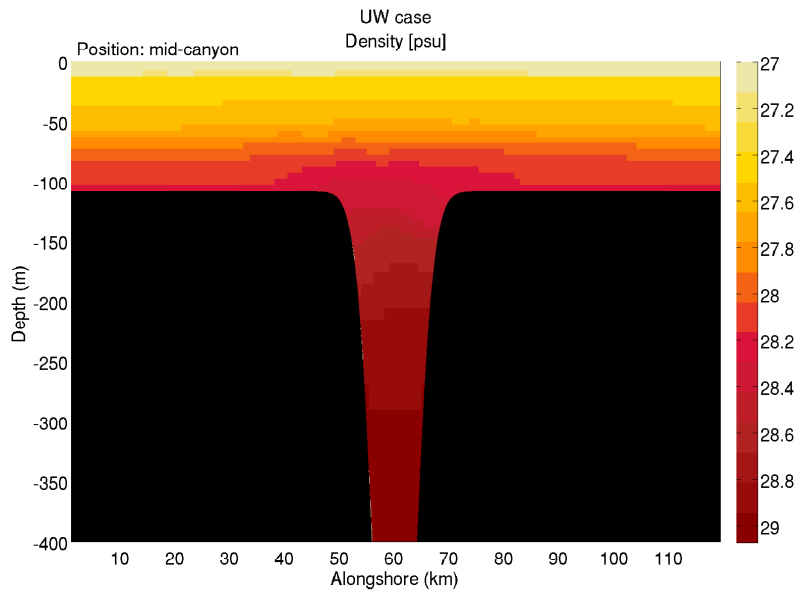
Though vertical velocity reveals that upward displacement of water does occur in downwelling canyons, density and nitrate anomalies indicate there is downwards advection of physical properties. Both density and nitrate exhibit regions of positive advection, however these regions occur away from the canyon and positive advection is weaker than negative advection.

Previous studies have found that submarine canyons in downwelling regions enhance coastal downwelling [Klinck, 1996; She and Klinck, 2000; Skliris et al., 2001; 2002]. Anomalies of density difference in current simulations show that downwelling is enhanced everywhere within the canyon and over the lower canyon, with downwelling being strongest around the canyon axis. In the upper 100 m, relatively weak downwelling occurs over the mid-canyon. This region of weaker downwelling appears as a relative lifting of isopycnals from the downstream to upstream canyon rim (Figure 2.14a). Lifting isopycnals is often a characteristic of upwelling occurring in a region. However, these are instantaneous profiles of what is occurring in the canyon. Using profiles of density difference and density difference anomaly it can be seen that this relative lifting of isopycnals is actually a region of relatively weak downwelling. This is another indicator that some studies may not be observing all the time-mean flow dynamics.

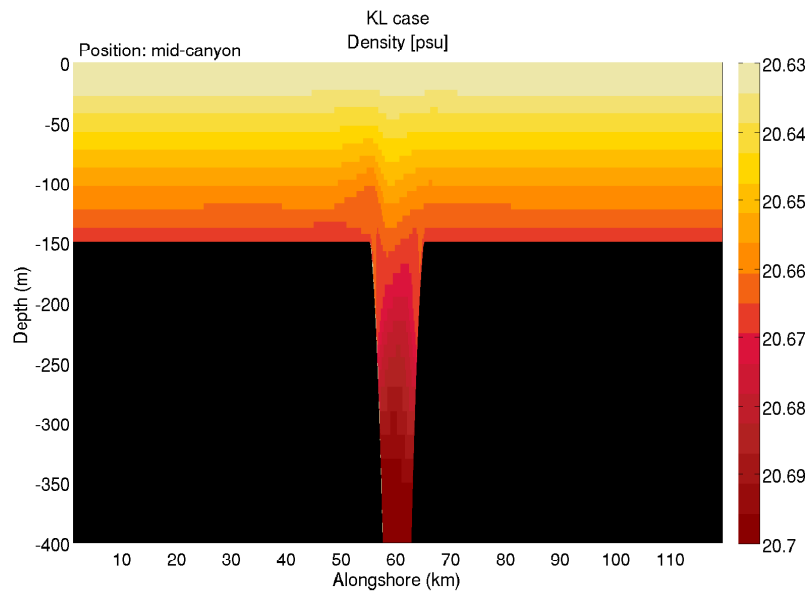
2.3.2 Parameter effects

Stratification has been found to have significant impacts on vertical and cross-shore transport [Klinck, 1996]. Previous studies have compared forcing responses between weakly and strongly stratified domains. However, these studies use either a uniformly stratified domain [Klinck, 1996], or a domain in which stratification varied in only 3 regions [Skliris et al., 2001; 2002]. Other studies have varied stratification in the canyon domain [Ardhuin et al., 1999; She and Klinck, 2000], but the effects of vertical variation in stratification have never before been studied. Thus, the non-dimensional parameter χ was introduced in this study to investigate the impacts vertical changes in stratification have on flow dynamics. Weak χ values indicate stratification is more uniform in the domain. Negative χ values indicate there is stronger stratification variation at shallower depths.

Rosby number and Burger number are non-dimensional parameters that are commonly used to measure the regional significance of Coriolis accelerations and stratification, respectively. These parameters can also be used to determine scales between observational, laboratory, and numerical models. In this section, Rossby number, Burger number, χ values, and incoming jet location are used to determine which regional parameters impact various flow dynamics.



(a) simulation with anticyclonic circulation



(b) simulation with cyclonic circulation

Figure 2.14: Isopycnal cross-sections at mid-canyon in (a) simulation with anticyclonic circulation (UW) and (b) simulation with cyclonic circulation (KL).

Circulation in the canyon

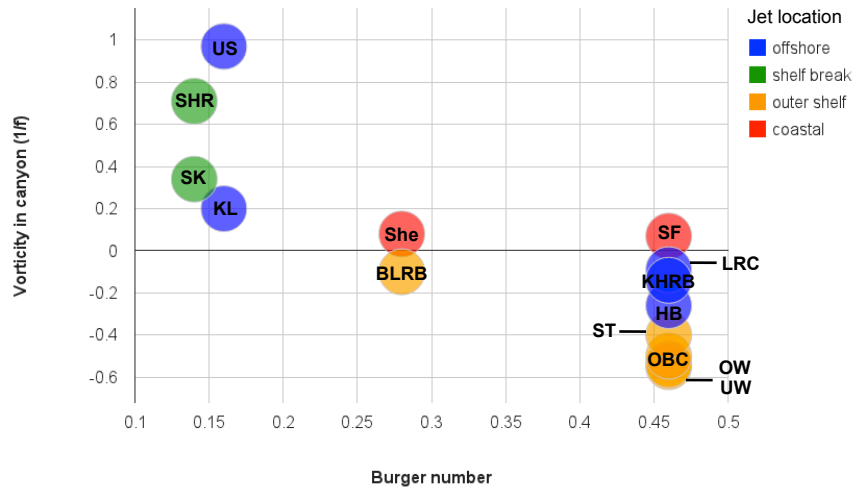
Patterns in horizontal circulation reveal Burger number to be an important parameter in determining vorticity within the canyon (Figure 2.15a). Four simulations with low Burger numbers (SHR, US, SK, KL) exhibit positive vorticity and cyclonic circulation at shelf break depth. Six simulations with high Burger numbers (UW, OW, OBC, ST, HB, KHRB) exhibit negative vorticity and anticyclonic circulation near shelf break depth. Four simulations with varying Burger numbers (BLRB, She, SF, LRC) show weak vorticity and circulation. Rossby number also appears to have an impact on vorticity magnitude (Figure 2.15b). For the simulations with cyclonic circulation, as incoming Rossby number increases vorticity magnitude also increases. This trend is not as apparent for the simulations with anticyclonic circulation.

The importance of the Burger number and its impact on circulation within the canyon is highlighted in the US and HB cases. These two simulations have the same model set-up, with the only difference being their buoyancy frequency (N) value. The US simulation has a lower Burger number and cyclonic shelf break circulation, while the HB simulation has a higher Burger number and anticyclonic shelf break circulation.

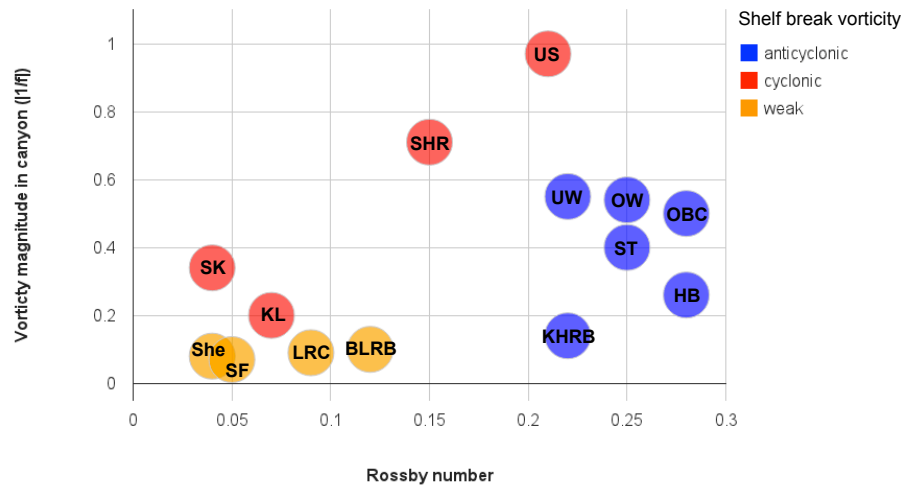
Anticyclonic circulation scenarios exhibit strong flow across the canyon axis and weaker flow along canyon walls and rims during the time-dependent phase, creating a negative shear in horizontal flow. In these simulations, flow is negligible along bottom topography (including the outer shelf) and flow turns weakly into the canyon but does not follow canyon isobaths. This causes flow crossing the canyon axis to impinge on the downstream wall and a small portion moves onshore due to negative vorticity in the canyon. This onshore flow, and compressing isopycnals, generates a trapped anticyclonic eddy within the canyon (Figure 2.4a), which can persist to depths of 500 m.

Cyclonic circulation scenarios have weakest horizontal flow across the canyon axis and strongest flow along canyon walls and rims (Figure 2.4b). This creates a positive shear in horizontal flow and enhances the tendency for cyclonic circulation. In these simulations, flow across the canyon axis is relatively weak and water parcels follow canyon isobaths, moving onshore in the upstream, and offshore in the downstream (Figure 2.4b).

Location of the incoming zonal jet is affected by stratification variations in the domain (Figure 2.16). Several model simulations use the same forcing conditions and different domain stratification, e.g. UW (SK) and US or HB (LRC) have the same forcing conditions with differences in χ values. The simulations with uniformly stratified domains (lower χ ; US, HB, LRC) have a zonal jet that is located further offshore



(a)



(b)

Figure 2.15: Effect of (a) Burger number and (b) incoming Rossby number on canyon vorticity for all model simulations.

relative to their counterparts with high χ values (UW, SK). Simulations forced by wind stress have weak coastal flows, regardless of domain stratification.

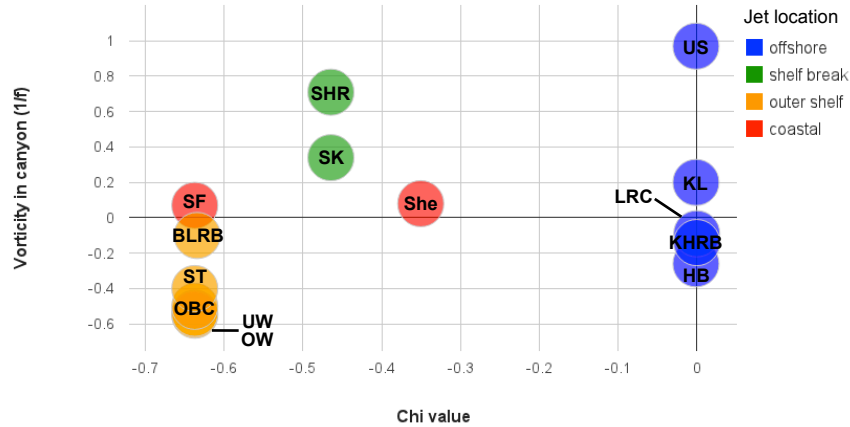
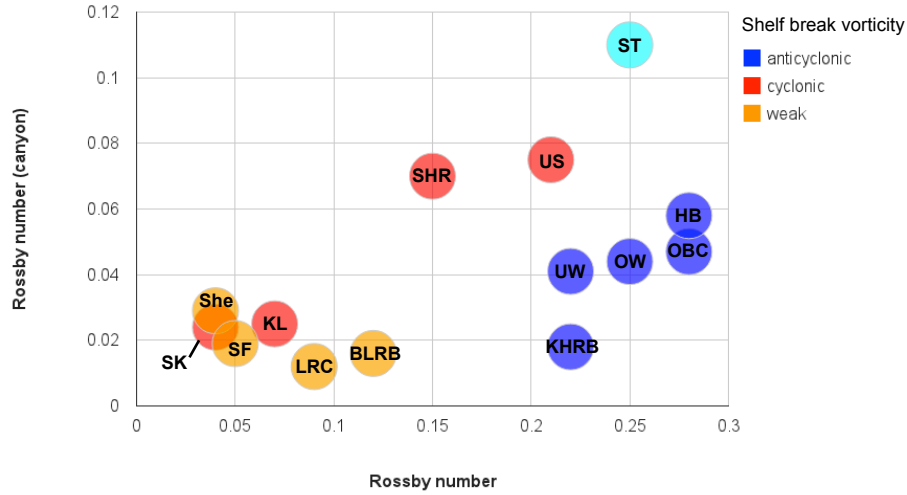


Figure 2.16: Zonal jet location upstream of the canyon.

As the body force is applied to model simulations, an onshore flow occurs and tilts isopycnals downwards. This leads to surface intensification of the zonal jet. Baroclinicity increases with increasing stratification in the upper water column. However, downwelling tends to reduce stratification over the shelf, making the jet more barotropic. With weak near surface stratification (low χ), this leads to an almost barotropic jet which feels bottom friction fairly strongly and is therefore reduced in intensity. In simulations with an offshore jet and low χ values, the zonal velocity is intensified at shelf break depth and negligible along continental slope topography (Table 2.3; KL, US, HB, LRC, KHRB). Strong near surface stratification (high χ) allows baroclinicity of the jet on the shelf, and thus less friction on it. In simulations with an outer shelf jet and high χ values, zonal velocity is intensified near the surface and negligible along bottom topography (Table 2.3; UW, OW, OBC, ST, BLRB).

Until now, Rossby number has been based on incoming flow strength. However, a Rossby number based on flow across the canyon axis ($R_{\bar{U}_{can}}$) may be more appropriate for looking at flow dynamics within the canyon. These values are compared to determine correlations between incoming and canyon axis flow (Figure 2.17). Due to the more complex topography in the slanted canyon simulation (ST), it is suspected that $R_{\bar{U}_{can}}$ is overestimated for this scenario and is thus marked as a possible outlier in subsequent plots.

For simulations with cyclonic circulation at shelf break depth, there is a relatively strong coupling



(a) Incoming and canyon zonal flow

Figure 2.17: Correlation between Rossby numbers based on incoming zonal flow and zonal flow integrated across the canyon axis. Due to complex canyon topography, canyon Rossby number for ST is likely overestimated and ST is considered an outlier.

between incoming and canyon axis flow speed. However, for anticyclonic circulation the coupling is weaker. The same incoming Rossby number results in a weaker canyon Rossby number. For the simulations with weak circulation, both Rossby numbers are small and not strongly correlated to each other.

Flow patterns describe the stronger (weaker) coupling between incoming and canyon Rossby numbers in the cyclonic (anticyclonic) simulations. In the anticyclonic cases, the eddy is focused over the canyon axis and flow in the canyon head is towards the upstream, while flow along the mid-canyon is towards the downstream (flow between mid-canyon and canyon mouth is downstream and slightly stronger along the canyon axis) (Figure 2.4a). This causes net zonal flow between the canyon head and mid-canyon to be almost negligible and thus weaken overall flow strength across the canyon axis. For cyclonic simulations, zonal flow is weaker across the canyon axis but everywhere towards the downstream (Figure 2.4b). Therefore, strong incoming flow increases zonal flow everywhere within the canyon.

For all simulations, Rossby number across the canyon is approximately one-third (or more) lower than Rossby number based on incoming flow. Incoming Rossby number is based on maximum zonal flow at shelf break depth upstream of the canyon, whereas Rossby number across the canyon is integrated from the canyon head to canyon mouth. Thus, incoming Rossby number is slightly overestimated relative to

canyon Rossby number.

Downwelling submarine canyons have been observed to modify incoming coastal jets by deflecting the current along canyon walls, with major modifications observed at shelf break depth [Flexas et al., 2008]. Current simulations indicate two types of flow deflection occurring, dependent on Burger number. With a high Burger number, strong flow impinges on the downstream wall and generates an anticyclonic eddy. With a low Burger number, flow follows canyon isobaths with strongest flow along bottom topography.

Vertical flux

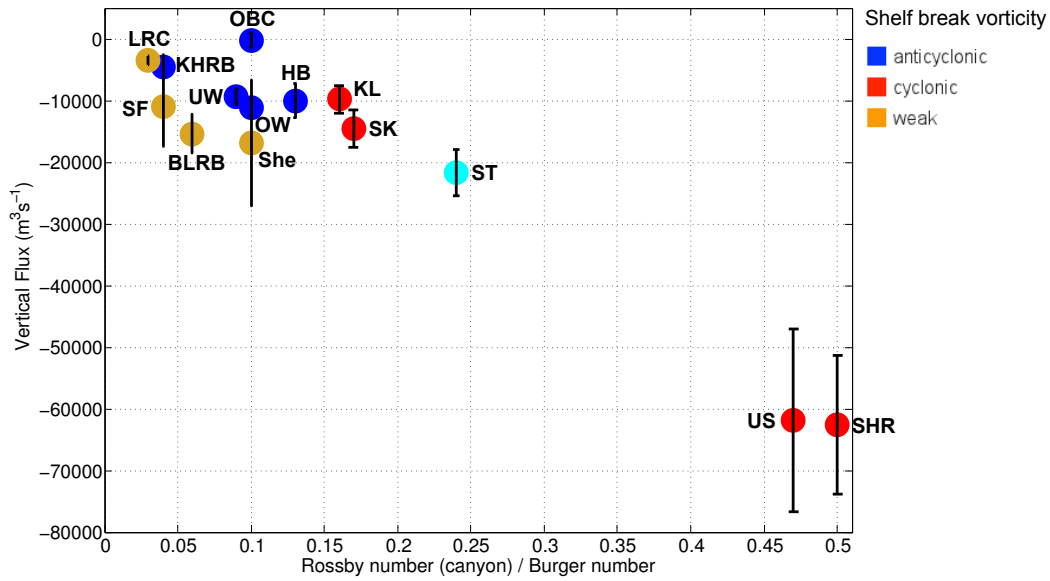
Net vertical flux was calculated for all model simulations as net flux in the canyon across the shelf break plane (150 m) averaged during the approximate advection dominated phase (averaged from model days 4-10). Initial errors in net vertical flux were calculated as the difference in flux values during two averaging periods, days 4-10 and days 3-9. However, 2 other sources of error were taken into consideration: 1) error due to variations in zonal flux (which varied 2-17% for most cases and 50% for the She and SF simulations); 2) 12 hr model output provided an approximately 10% aliasing error (Appendix E). Therefore, error in all model simulations was taken as the maximum error in: 1) the sum of the minimum 10% aliasing error plus error due to zonal flux variations or 2) errors in averaging period.

Net vertical flux is directly proportional to Rossby number of flow across the canyon axis and inversely proportional to Burger number (Figure 2.18). For example, US and SHR have the highest canyon Rossby number to Burger number ratios, and exhibit the greatest downward flux.

Although previous studies have not specifically looked at changes in zonal flow strength, current simulations show that scenarios with stronger flow across the canyon axis lead to stronger downwards flux. This is unsurprising since increasing Rossby number indicates increasing cross-canyon flow, and thus a stronger pressure gradient along the canyon.

Increased stratification has been found to reduce vertical and cross-shore transport, as well as the depth range which fluid parcels move in a circuit around a canyon [Klinck, 1996; Skliris et al., 2001; 2002]. Current simulations show a similar pattern. For example, US and HB cases have the same forcing and variation in stratification, with the only difference being that HB has an increased buoyancy frequency (N). Net cross-shore transport (not shown) in the US (weaker stratification) case is 2x larger and net vertical transport is approximately 6x larger.

Circulation and vertical velocity are instantaneous measurements that capture what is occurring during the advection dominated phase, and both are influenced by Burger and Rossby number. Burger number drives circulation type and strength of vertical flux: simulations with a high Burger number



(a) Vertical flux

Figure 2.18: Burger and canyon Rossby number effect on vertical flux at shelf break depth (150 m). Bubble size is directly proportional to errors in flux estimates, based on percent differences. Due to complex canyon topography, canyon Rossby number for ST is likely overestimated and ST is considered an outlier.

exhibit a trapped anticyclonic eddy and weak vertical flux, simulations with a low Burger number exhibit cyclonic circulation and strong vertical flux. Rossby number drives strength of vertical flux: high Rossby numbers generate strong vertical flux. Thus, Burger and Rossby numbers are important parameters during the advection dominated phase.

Zonal jet placement has an effect on the time dependence of vertical flux. Simulations with an outer shelf jet show strong variations in flux across the shelf break plane (150 m depth). In the majority of these simulations, vertical flux across both the upstream and downstream planes oscillates between positive and negative values. Simulations with an offshore jet have relatively steady vertical fluxes at this depth (Figure F.1). In the majority of these scenarios flux in the upstream is always downwards, while flux in the downstream is always upwards. Previous studies have found that onshore/offshore displacement of a zonal jet impacts flow dynamics in a canyon [Alvarez et al., 1996; Jordi et al., 2005; Ahumada-Sempoal et al., 2013]. Onshore displacement (towards the canyon head) has been found to generate a current meander which produces an enhancement of shelf-slope exchange and an oscillation in vertical flow [Jordi et al., 2005]. In present simulations, cross-shore transport is roughly the same in simulations with an offshore or outer shelf jet (Figure F.1). It should be noted that differences exist between the current and

previous studies. Primarily, previous studies looked at time-varying displacement of the zonal jet, which produced a meander that drove vertical and cross-shore variations. Simulations presented here looked at flow that was semi-steady in time, and a meander is not produced.

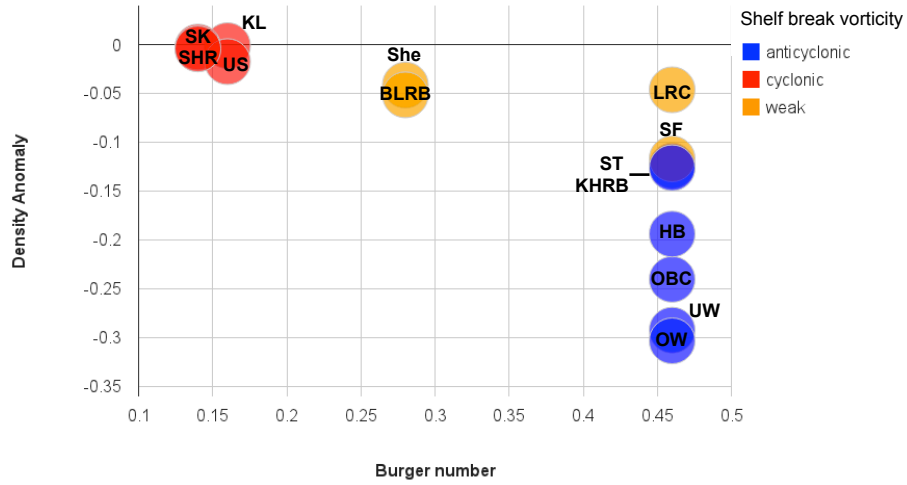
Density anomalies

Patterns in density anomalies indicate that Burger number (and subsequently vorticity) has the largest impact on the magnitude of density anomalies (Figure 2.19a). All simulations show net downwards advection of density within the canyon. Simulations with lower Burger numbers (and cyclonic circulation) have weaker density anomalies at shelf break depth. Simulations with anticyclonic circulation exhibit stronger downwards density advection. Simulations with weak circulation also appear to be affected by Burger number.

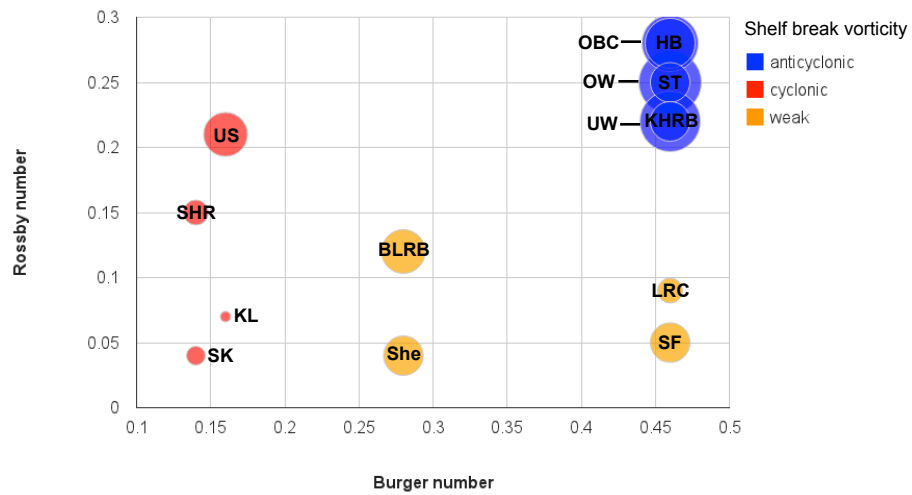
It is unsurprising that simulations with high Burger numbers have stronger density anomalies. These simulations have stronger variations in initial density between vertical layers. Thus, a water parcel that advects the same vertical distance in a simulation with a high Burger number versus one with a low Burger number will have a stronger density anomaly. To remove the effect of Burger number on density advection, density anomaly was divided by the squared buoyancy frequency (N_{sb}^2) to give a normalized density value (Figure 2.19b). This value represents the vertical height change of a water parcel in each simulation. For this estimated vertical height change, there does not appear to be a pattern based on any parameter. By normalizing the density anomaly, effects due to Burger number have been removed and there appears to be no correlation in increasing/decreasing Rossby or Burger number and depth change of an advected water parcel. However, it is likely that using normalized density anomaly to look for other patterns between model simulations does not work due to differences in initial density profiles. Curvature of density profiles varies between simulations and vertical height change of a water parcel is estimated differently for each scenario.

Location of incoming zonal jet does affect the occurrence of positive density anomalies in the model domain (Table 2.6). Simulations with the zonal jet located along the shallow coast or over the outer shelf (directly above the upper canyon) exhibit negative density anomalies (downwards advection) at all depths in the model domain (pattern 1). Simulations which show upwards density advection (positive density anomalies) during the day 5-8 averaged period have a zonal jet located either offshore or along the shelf break. The positive anomalies occur away from the canyon in the upstream and downstream (pattern 2). There is not a correlation between pattern 1/2 and average density anomaly.

Forces can explain how jet location impacts the occurrence of positive density anomalies. For the



(a) Density anomaly



(b) Normalized density anomaly

Figure 2.19: (a) Burger number effect on average density anomaly and (b) Burger and incoming Rossby number effect on normalized density anomaly in canyon for all simulations (averaged between model days 4-10). Bubble size in (b) is directly proportional to relative magnitude of normalized density anomaly.

zonal jet to turn shoreward along the upstream canyon rim, it needs a centrifugal force. This is provided by a change in the pressure gradient: higher pressure offshore of the jet and lower pressure onshore. This weakens the Coriolis force and pressure gradient force balance, and allows flow to turn. In the simulations with an offshore or shelf break jet, this pressure gradient change is provided by upwelling of denser water occurring offshore of the canyon and zonal jet (Figure 2.11b). For the simulations with a coastal or outer shelf jet, this upwelling occurs over the outer shelf, where stronger downwelling is already occurring. This is seen as a reduction of downwelling rather than upwelling (Figure 2.11a).

Previous studies have found that submarine canyons, in regions with a right-bounded jet, enhance the downward advection of density properties [Klinck, 1996; She and Klinck, 2000; Skliris et al., 2001; 2002]. Similar results are seen in plots of density difference anomalies (Figure 2.12). Downwards advection of density is enhanced within the canyon for all simulations. The occurrence of positive density anomalies away from the canyon is affected by jet location. Simulations with on offshore or shelf break jet exhibit positive anomalies away from the canyon, while simulations with a coastal or outer shelf jet exhibit negative density anomalies everywhere in the domain.

Nitrate anomalies

Comparisons of non-dimensional parameters indicate incoming Rossby number has the greatest impact on vertical advection of nitrate (Figure 2.20). Simulations with higher Rossby numbers have greater changes in nitrate concentration. This indicates as more flow enters a canyon, advection of passive tracers strengthens. Patterns in incoming Rossby number show a stronger correlation than patterns based on canyon Rossby number.

Density and nitrate anomalies measure a combination of time-dependent and advection dominated downwelling. Density and nitrate anomaly time series for the UW case (not shown) indicate averaged anomalies are approximately 85% time-dependent and 15% advection dominated. Allen [1996] finds vertical flux to be inversely proportional to the Burger number for time-dependent upwelling or downwelling. Thus, it would be expected that changes in nitrate advection would be inversely proportional to Burger number. However, this does not occur in current model simulations, e.g. UW and US cases have the same Rossby number, different stratification, but similar nitrate anomalies. Comparing cross-sections of nitrate anomalies (Figure 2.13a and F.7i, respectively), nitrate anomaly is weaker and broader in the stronger stratification scenario (UW) relative to the weaker stratification scenario (US). The region of negative anomalies upstream of the canyon is approximately 2.5-3x larger in the weaker stratification case (UW). Rossby radius of deformation is 3x larger in the UW case, so size of nitrate anomaly is proportional

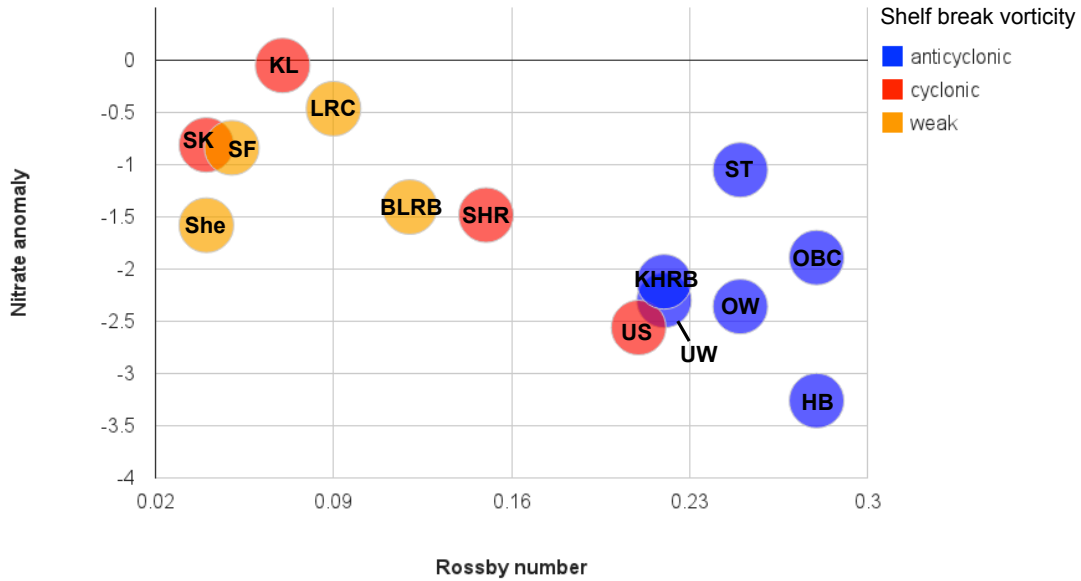


Figure 2.20: Incoming Rossby number effect on nitrate anomaly for all simulations (averaged between model days 4-10).

to Rossby radius (and stratification). Therefore, strength of nitrate anomaly is inversely proportional to stratification, while size of nitrate anomaly is directly proportional to stratification. These have a cancelling effect and only the Rossby number appears to have an influence on nitrate anomaly.

Density and nitrate exhibit the same anomaly patterns in the same model scenarios: negative anomalies everywhere in the canyon domain (pattern 1) and positive anomalies away from the canyon (pattern 2). This indicates jet location impacts the occurrence of nitrate anomalies following the same reasoning described in the previous section. Therefore, the upwelling occurring away from the canyon includes denser water and higher nitrate concentrations.

Density and nitrate anomalies are integrated measurements and include a strong signal from the time-dependent phase. Anomaly patterns are influenced by jet location, which in turn is affected by vertical variations in stratification. As previously discussed (vertical velocity section), zonal jet placement effects time dependence of vertical flux. Offshore and shelf break jets generate upward velocity away from the canyon and steadier vertical flux (relative to coastal/outer shelf jets). Thus, location of the zonal jet is important during time-dependent phases of flow.

2.3.3 Diffusivity

Average diapycnal diffusivity in Ascension Canyon (west coast, North America) has been observed as approximately $3.92 \times 10^{-3} \text{ m}^2\text{s}^{-1}$ [Gregg et al., 2011]. Using this value, an estimate of flux due to mixing in the current canyon scenarios can be determined. Calculating diffusive flux as:

$$\text{Diffusive Flux} = \kappa_p \times \frac{\Delta NO_3}{\Delta z} \times \text{area},$$

where κ_p is average diapycnal diffusivity, changes in nitrate are taken from the initial nitrate profile, and area is taken as area across three horizontal planes (100 m, 150 m, and 600 m).

An advective flux was calculated by estimating the volume of water below the 100 m (150 m and 600 m) plane with a nitrate concentration lower than the initial concentration at 100 m (150 m and 600 m). This was done for each model grid cell below the respective plane ($volume_{cell}$). This volume was then multiplied by depth of the grid cell below the 100 m plane (150 m and 600 m) ($depth_{cell}$). Summing these provided a measure of the volume of water advected below the 100 m (150 m and 600 m) plane and the vertical extent of the advection (V_{adv}). This was calculated for each model simulation as:

$$V_{adv} = \Sigma volume_{cell} \times depth_{cell}.$$

V_{adv} was measured for model days 4 and 10, and differences were calculated to isolate advection that occurred during the advection dominated phase. This value was divided by the timescale of the advection phase (Δt) to give an advection speed. Finally, the advection speed was multiplied by the nitrate gradient ($\frac{\Delta NO_3}{\Delta z}$) to give an overall advective flux for each model simulation:

$$\text{Advective Flux} = \frac{\Delta V_{adv}}{\Delta t} \times \frac{\Delta NO_3}{\Delta z}.$$

Nitrate gradient ($\frac{\Delta NO_3}{\Delta z}$) was the same gradient used in the diffusive flux calculation. Diffusion in the current model is small ($10^{-7} \text{ m}^2 \text{ s}^{-1}$), thus mixing has an insignificant impact on nitrate flux calculations in the model simulations. Therefore, comparisons of estimated diffusive flux and model calculated advective flux are true comparisons of the separate processes (Table 2.7).

Table 2.7: Diffusive and advective flux of nitrate across 3 vertical planes

	Diffusive	Advective (maximum)	Advective (mean)	Advective (minimum)
100 m	9.5×10^4	-5.2×10^5	-7.1×10^4	-7.6×10^3
150 m	2.0×10^4	-2.0×10^5	-3.5×10^4	-1.5×10^3
600 m	3.5×10^2	-3.9×10^3	-7.0×10^2	0

Units are $\mu\text{M m}^3 \text{ s}^{-1}$.

Diffusive flux is likely overestimated for regions similar to the Mediterranean Sea, i.e. regions with limited tides. However, these diffusive flux values provide a good estimate for nitrate diffusion in down-

welling canyons in other regions of the world. In the upper 100 m, diffusion of nitrate is stronger than mean advection of nitrate. At 150 m and 600 m, mean downwards advection of nitrate is stronger than upwards diffusion of nitrate. These positive diffusive flux estimates indicate that nitrate anomalies calculated in the previous section (Figure 2.20) are likely stronger than what would occur in a real world downwelling canyon scenario.

Phytoplankton uptake nitrate as a nutrient in the surface photic zone, and as particulate matter sinks nitrate is lost from the photic zone to deeper water. Thus, nitrate concentration is low in the surface layers and high at depth, with strong variations between the surface and deep layers. In the current model domain, nitrate variations are strongest between 50-200 m. Regions with strong nitrate variations between vertical layers lead to stronger diffusive fluxes. This explains why diffusive flux becomes two orders of magnitude smaller at 600 m depth.

2.3.4 Summary: Circulation, flux, and advection for steady flow over downwelling canyons

As present studies have shown, Burger number (stratification) has the largest impact on flow dynamics in downwelling submarine canyons. Circulation in downwelling canyons can be broken down into 2 main categories: 1) cyclonic circulation (positive vorticity), which occurs in canyons with low Burger numbers, and 2) anticyclonic circulation (negative vorticity), which occurs in canyons with high Burger numbers. We will ignore the 3rd category, weak circulation, which shows weak correlation between forcing conditions and flow dynamics. Increasing flow strength increases the magnitude of vorticity for canyons with cyclonic circulation. In both canyon categories, stronger horizontal flow and weaker stratification allow for greater vertical flux at shelf break depth. Jet placement impacts the occurrence of positive density/nitrate anomalies away from the canyon. Offshore/shelf break jets lead to positive density anomalies away from the canyon.

Flow dynamics seen in present studies have been found in previous literature using similar forcing conditions. Klinck [1996] and Skliris [2001; 2002] had offshore/shelf break zonal jets with small Rossby and Burger numbers. This leads to a cyclonic flow pattern and small patches of weak upwelling away from the canyon. Blanes Canyon has an outer-shelf jet with high Rossby and Burger numbers. The high Burger number and jet placement lead to an anticyclonic flow pattern and everywhere downwards density advection. The anticyclonic vorticity leads to a weak coupling between incoming flow strength and flow strength across the canyon axis. Vertical flux is weak and density (nitrate) flux is strong due to

the high Burger (Rossby) number. She and Klinck's [2000] jet was near the coast and weakly coupled to the canyon, and thus vorticity, flux, density and nitrate advection were weak.

2.4 Conclusion

A numerical model (MITgcm) was used to study flow dynamics around downwelling submarine canyons under various forcing conditions. Three non-dimensional parameters were used to determine how regional dynamics impact flow dynamics. Although some simulations do see brief periods of upwards displacement of water during the 10 day model period, the presence of the submarine canyon is found to enhance downwards advection of density in all model scenarios. Stratification strongly affects circulation and temporal density changes. Anticyclonic circulation and stronger downwards advection of density occurs in simulations with higher Burger numbers, while cyclonic circulation and weaker density advection occur in simulations with a lower Burger number. For simulations with cyclonic circulation, stronger incoming flow (higher Rossby number) produces stronger vorticity magnitudes within the canyon. Simulations with cyclonic circulation have strong coupling between incoming and cross canyon Rossby numbers, while anticyclonic simulations have a weaker coupling. Strong flow across the canyon axis (high canyon Rossby number) and weak stratification (low Burger number) increase downwards vertical flux at shelf break depth (150 m), while increasing incoming Rossby number leads to stronger downwards advection of nitrate. Patterns in advection phase nitrate anomalies differ from patterns of density anomalies, indicating that measurements of nitrate cannot be easily inferred from modelled density advection. Zonal jet location is influenced by vertical variations in stratification (χ). Uniformly stratified domains (low $|\chi|$) exhibit offshore or shelf break jets, while non-uniformly stratified domains (high $|\chi|$) exhibit outer shelf or coastal jets. In turn, jet location impacts temporal density anomalies, with offshore or shelf break jets generating positive density anomalies away from the canyon and outer shelf or coastal jets generating negative density anomalies everywhere in the model domain.

Chapter 3

Conclusions

3.1 Research objectives

Fourteen numerical simulations of downwelling canyons were modelled based on various forcing conditions. Two simulations were modelled after coastal flow observed in Blanes Canyon [Flexas et al., 2008]. Three more simulations were modelled after previous studies of various downwelling canyons [Klinck, 1996; She and Klinck, 2000; Skliris et al., 2001; 2002]. Nine simulations include minor changes to various parameters in the previous scenarios. These simulations were used to study flow dynamics in and around downwelling submarine canyons. Of particular interest was the degree to which upwelling occurs in these regions, as well as how changes in forcing conditions impact flow dynamics in the canyon. Research objectives stated in Chapter 1 are used to summarize model results.

3.1.1 Determine if upwelling occurs in or around downwelling canyons. If so, where does upwelling occur, and how intense is upwelling?

Net upwards displacement does occur for some scenarios, but times of positive vertical flux in the canyon is brief and irregular. Density and nitrate profiles show that net downwards advection of these properties occur in all model simulations. In none of the 14 modeled scenarios did upwelling of dense, cold deep water onto the shallow shelf occur.

An observational study of Blanes Canyon [Flexas et al., 2008] found evidence of upwelling occurring near shelf break depth inside the canyon (between 100-200 m depth), but upwelled water did not reach the continental shelf. This was the first study with a right-bounded incoming jet which found upwelling

to occur near shelf break depth. Evidence for upwelling was based on volume flux estimates and isopycnal profiles. Results from current model simulations show that periods of net upwelling do occur at shelf break depth in Blanes Canyon simulations (Figure 2.9; UW, OW, OBC). For the UW and OW cases, these periods are brief and do not last more than a day. However, the simulation with open boundary conditions (OBC) did exhibit a 2 day period of net upwards velocity across the shelf break plane. In the current study and the observational study, isopycnals along the downstream wall appear to lift relative to their placement along the downstream wall (Figure 2.14), which is a characteristic of upwelling. However, plan views images of density difference reveal that downwards density advection occurs everywhere within the canyon (Figure 2.11a). Anomalies in density difference show that downwelling is enhanced everywhere within the canyon (Figure 2.12a). For the Blanes Canyon simulation, downwards density advection along the upstream wall is stronger relative to the same position along the downstream wall.

3.1.2 Determine what parameters affect flow dynamics.

Circulation

Plan view images of vorticity and horizontal velocity vector plots were used to determine absolute vorticity and canyon circulation. Three types of canyon circulation occur based on Burger number. Simulations with a high Burger number have negative vorticity at shelf break depth and generate a trapped anticyclonic eddy within the canyon. Simulations with a low Burger number have positive vorticity and cyclonic circulation at shelf break depth. Some simulations have very weak circulation regardless of Burger number. This is due to strength of incoming zonal flow (Rossby number). For the cyclonic simulations, increasing Rossby number creates stronger vorticity within the canyon.

Vertical variations in stratification impact jet placement. Simulations with uniform stratification have jets located further offshore relative to simulations with the same forcing and less uniform stratification. Simulations with cyclonic circulation have a strong coupling between incoming and canyon axis flow strength, while simulations with anticyclonic circulation (and a trapped eddy) exhibit weaker coupling. Scenarios with weak circulation have weak incoming and canyon Rossby numbers.

Vertical flux

Plan views images were used to determine vertical flux patterns in model simulations; two patterns occur. In simulations with weak or anticyclonic circulation, enhanced downwards (upwards) velocity is limited to the upstream (downstream) corner of the canyon mouth. In simulations with cyclonic

circulation, vertical velocity has an antisymmetrical pattern where positive and negative vertical velocity is split along the canyon axis. Negative velocity occurs in the upstream portion of the canyon, and positive velocity occurred in the downstream portion of the canyon.

An average net vertical flux was calculated as the average flux across each grid cell at shelf break depth within the canyon domain. Average net vertical flux during the advection dominant phase is negative for all canyon scenarios. As canyon Rossby number increases, or Burger number decreases, vertical flux within the canyon increases. This pattern is strongest for scenarios with cyclonic circulation.

Density anomalies

Average density within the canyon at shelf break depth was calculated during model day 5-8. This value was subtracted from initial density at shelf break depth to give a density anomaly. From this, a background density anomaly was calculated along downstream isobaths. These values were subtracted from grid points of similar isobaths to give a density difference anomaly. The density difference anomaly was then used to determine how much the canyon enhanced or reduced the background downwelling in the domain.

Simulations with a zonal jet placed along the coast or over the outer shelf have negative density anomalies everywhere within the model domain. Density difference anomaly revealed downwards advection is enhanced everywhere within the canyon, and is strongest near the canyon head. Simulations with a shelf break or offshore jet have negative density anomalies within the canyon, but positive anomalies away from the canyon. For these simulations, downwards advection is enhanced within the canyon, being strongest along canyon walls and weaker towards the canyon axis.

Average density anomalies were calculated during the advection dominant phase (model day 4-10). Burger number impacts the strength of density anomalies within the canyon. Simulations with a high Burger number (strong vertical variations in density) exhibit the greatest density anomalies, while simulations with a low Burger number (weak vertical variations in density) exhibit relatively weak density anomalies. However, none of the non-dimensional parameters appear to have an impact on vertical advection (normalized density anomaly) of a water parcel.

Nitrate anomalies

Nitrate profiles act as a passive tracer and provide one input parameter that was the same for all model simulations. Cross-section images reveal downwards advection of nitrate within the canyon for all model simulations. However, simulations with an offshore or shelf break jet do show upwards advection

of nitrate away from the canyon over the outer shelf and shelf break.

Nitrate anomalies within the canyon were used to calculate flux due to advection. An average nitrate value within the canyon at shelf break depth was calculated. This average was subtracted from the initial nitrate concentration at shelf break depth to give an estimate of nitrate anomaly in the canyon. Nitrate advection increases with increasing incoming Rossby number. This correlation is stronger with the incoming Rossby number than the canyon Rossby number.

3.2 Future research

The aim of this study was to better understand basic forcing parameters and their impacts on flow dynamics in downwelling submarine canyons. But there are many real world forcing conditions that are not included in this study. Future work could include addition of regional river input, as well as seasonal changes in climate, which would both impact density structure and time-varying placement of coastal flow. Density structure is an important parameter in determining density advection and vertical flux, and a better understanding of seasonal changes would be important. Previous studies have suggested that onshore/offshore displacement of coastal jets has a significant impact on flow dynamics [Alvarez et al., 1996; Jordi et al., 2005; Ahumada-Sempoal et al., 2013]. Time-varying displacement of zonal jets may have different hydrodynamic responses depending on the canyon geometry and density structure.

Future work could also include the addition of wind events. Studying a downwelling canyon with a trapped anticyclonic eddy, Arduin et al. [1999] found that a right-bounded 1 day wind event enhanced coastal downwelling, but rebound upwelling occurred as the wind relaxed. In the same study, coastal wind blowing offshore initiated upwelling followed by rebound downwelling. However, the upwelling event allowed renewal of waters trapped in the anticyclonic canyon eddy. Studying a downwelling canyon with cyclonic circulation, Skliris et al. [2001; 2002] similarly found a right-bounded wind event to enhance coastal downwelling, while a left-bounded wind event led to a reversal of flow and strong coastal upwelling. Both studies found that during wind events, canyons enhanced cross-slope and vertical exchange. Wind events could be applied to simulations of the current study to develop an improved understanding of the impacts these wind events have to various downwelling systems.

Few laboratory studies have been performed for downwelling canyons, especially canyons with a strong shelf break jet. Laboratory experiments can isolate individual processes and aid in the development of numerical models [Boyer et al., 2004]. Important non-dimensional parameters found in this study could be used in a physical model to further test how these forces affect flow. Performance of the numerical

model can then be compared to laboratory results.

3.3 Application to real world

Forcing conditions can vary between submarine canyons along the same continental shelf. There are many regional factors that impact forcing conditions, e.g. river runoff, wind events, bottom morphology, regional/seasonal climatology. Thusly, it would be naive to assume numerical models can incorporate the many complex processes that occur in real world physical systems. Exact flow dynamics cannot be reproduced, but numerical models and knowledge of local dynamics can help to create an understanding of general circulation around downwelling canyons. It is hoped the results from this study can be used as the foundational building blocks in the continuing pursuit of understanding canyon impacts on regional circulation.

This project adds to the continuing study of flow dynamics in downwelling submarine canyons. This study compliments previous studies performed by Klinck [1996], She and Klinck [2002], Skliris et al., [2001, 2002], and Flexas et al., [2008]. Downwelling submarine canyons, especially those in the Mediterranean Sea, and their impacts on coastal ecosystems has become an interest to scientists in recent years [Wurtz, 2012]. A fundamental understanding of the physical dynamics of these regions is important for broader studies of ecosystem chemistry and biology as well as more complex physical mechanisms. Furthermore, an understanding of regional impacts to flow dynamics will be useful in determining important measurement regions during observational cruises.

Bibliography

- Adcroft, A., Hill, C., Campin, J.-M., Marshall, J., and Heimbach, P. (2004). Overview of the formulation and numerics of the MIT GCM. In *Proceedings of the ECMWF seminar series on Numerical Methods, Recent developments in numerical methods for atmosphere and ocean modelling*, pages 139–149.
- Ahumada-Sempoal, M.-A., Flexas, M., Bernardello, R., Bahamon, N., and Cruzado, A. (2013). Northern Current variability and its impact on the Blanes Canyon circulation: A numerical study. *Progress in Oceanography*, 118(0):61 – 70.
- Allen, J. S. and Newberger, P. A. (1998). On symmetric instabilities in oceanic bottom boundary layers. *Journal of Physical Oceanography*, 28(6):1131–1151.
- Allen, S. E. (1996). Topographically generated, subinertial flows within a finite length canyon. *Journal of Physical Oceanography*, 26(8):1608–1632.
- Allen, S. E. (2000). On subinertial flow in submarine canyons: Effect of geometry. *Journal of Geophysical Research: Oceans (1978–2012)*, 105(C1):1285–1297.
- Allen, S. E. (2004). Restrictions on deep flow across the shelf-break and the role of submarine canyons in facilitating such flow. *Surveys in geophysics*, 25(3-4):221–247.
- Allen, S. E. and Durrieu de Madron, X. (2009). A review of the role of submarine canyons in deep-ocean exchange with the shelf. *Ocean Science*, 5(4):607–620.
- Alvarez, A., Tintoré, J., and Sabatés, A. (1996). Flow modification and shelf-slope exchange induced by a submarine canyon off the northeast Spanish coast. *Journal of Geophysical Research: Oceans*, 101(C5):12043–12055.
- Ardhuin, F., Pinot, J.-M., and Tintor, J. (1999). Numerical study of the circulation in a steep canyon off

- the Catalan coast (western Mediterranean). *Journal of Geophysical Research: Oceans*, 104(C5):11115–11135.
- Bennett, A. F. and Kloeden, P. E. (1978). Boundary conditions for limited-area forecasts. *Journal of the Atmospheric Sciences*, 35(6):990–996.
- Boyer, D. L., Haidvogel, D. B., and Perenne, N. (2004). Laboratory-numerical model comparisons of canyon flows: A parameter study. *Journal of Physical Oceanography*, 34(7):1588–1609.
- Brink, K. (1998). *Deep-sea forcing and exchange processes*. John Wiley and Sons, New York.
- Camerlengo, A. L. and O’Brien, J. J. (1980). Open boundary conditions in rotating fluids. *Journal of Computational Physics*, 35(1):12 – 35.
- Company, J. B., Ramirez-Llodra, E., Sarda, F., Aguzzi, J., Puig, P., Canals, M., Calafat, A., Palanques, A., Sole, M., Sanchez-Vidal, A., Martin, J., Lastras, G., Tecchio, S., Koenig, S., Fernandez-Arcaya, U., Mecho, A., and Fernandez, P. (2012). Submarine canyons in the Catalan Sea (NW Mediterranean): megafaunal biodiversity patterns and anthropogenic threats. In Wurtz, M., editor, *Mediterranean Submarine Canyons: Ecology and Governance*, pages 133–144, Gland, Switzerland and Mlaga, Spain: IUCN.
- Dawe, J. T. and Allen, S. E. (2010). Solution convergence of flow over steep topography in a numerical model of canyon upwelling. *Journal of Geophysical Research: Oceans*, 115(C5):n/a–n/a.
- Dinniman, M. S. and Klinck, J. M. (2002). The influence of open versus periodic alongshore boundaries on circulation near submarine canyons. *Journal of Atmospheric and Oceanic Technology*, 19(10):1722–1737.
- Flather, R. A. (1976). A tidal model of the northwest European continental shelf. *Mem. Soc. R. Sci. Liege*, 10(6):141–164.
- Flexas, M. M., Boyer, D. L., Espino, M., Puigdefbregas, J., Rubio, A., and Company, J. B. (2008). Circulation over a submarine canyon in the NW Mediterranean. *Journal of Geophysical Research: Oceans*, 113(C12):n/a–n/a.
- Garcia, R., van Oevelen, D., Soetaert, K., Thomsen, L., Stigter, H. D., and Epping, E. (2008). Deposition rates, mixing intensity and organic content in two contrasting submarine canyons. *Progress in Oceanography*, 76(2):192 – 215.

- Gregg, M. C., Hall, R. A., Carter, G. S., Alford, M. H., Lien, R.-C., Winkel, D. P., and Wain, D. J. (2011). Flow and mixing in Ascension, a steep, narrow canyon. *Journal of Geophysical Research: Oceans*, 116(C7):n/a–n/a.
- Griffies, S. M. and Hallberg, R. W. (2000). Biharmonic friction with a Smagorinsky-like viscosity for use in large-scale eddy-permitting ocean models. *Mon. Wea. Rev.*, 128(8):2935–2946.
- Harris, P. T. and Whiteway, T. (2011). Global distribution of large submarine canyons: Geomorphic differences between active and passive continental margins. *Marine Geology*, 285(14):69 – 86.
- Hickey, B. (1995). Coastal submarine canyons. *Topographic effects in the ocean. SOEST Special publications*, pages 95–110.
- Hickey, B. M. (1997). The response of a steep-sided, narrow canyon to time-variable wind forcing. *Journal of Physical Oceanography*, 27(5):697–726.
- Jordi, A., Orfila, A., Basterretxea, G., and Tintor, J. (2005). Shelf-slope exchanges by frontal variability in a steep submarine canyon. *Progress in Oceanography*, 66(24):120 – 141.
- Kämpf, J. (2006). Transient wind-driven upwelling in a submarine canyon: A process-oriented modeling study. *Journal of Geophysical Research: Oceans*, 111(C11):n/a–n/a.
- Klinck, J. M. (1988). The influence of a narrow transverse canyon on initially geostrophic flow. *Journal of Geophysical Research: Oceans (1978–2012)*, 93(C1):509–515.
- Klinck, J. M. (1996). Circulation near submarine canyons: A modeling study. *Journal of Geophysical Research: Oceans*, 101(C1):1211–1223.
- Lapouyade, A. and de Madron, X. D. (2001). Seasonal variability of the advective transport of particulate matter and organic carbon in the Gulf of Lion (NW Mediterranean). *Oceanologica Acta*, 24(3):295 – 312.
- Marques, V., Chaves, C., Morais, A., Cardador, F., and Stratoudakis, Y. (2005). Distribution and abundance of snipefish (*Macroramphosus* spp) off Portugal (1998-2003). *Scientia Marina*, 69:563–576.
- Marshall, J., Adcroft, A., Hill, C., Perelman, L., and Heisey, C. (1997). A finite-volume, incompressible Navier Stokes model for studies of the ocean on parallel computers. *Journal of Geophysical Research: Oceans*, 102(C3):5753–5766.

- Martinsen, E. A. and Engedahl, H. (1987). Implementation and testing of a lateral boundary scheme as an open boundary condition in a barotropic ocean model. *Coastal Engineering*, 11(56):603 – 627.
- Millot, C. (1999). Circulation in the western Mediterranean Sea. *Journal of Marine Systems*, 20(14):423 – 442.
- Morais, P., Borges, T. C., Carnall, V., Terrinha, P., Cooper, C., and Cooper, R. (2007). Trawl-induced bottom disturbances off the south coast of portugal: direct observations by the delta manned-submersible on the submarine canyon of portimão. *Marine Ecology*, 28:112–122.
- Oliger, J. and Sundstrom, A. (1978). Theoretical and practical aspects of some initial boundary value problems in fluid dynamics. *SIAM Journal on Applied Mathematics*, 35(3):419–446.
- Orlanski, I. (1976). A simple boundary condition for unbounded hyperbolic flows. *Journal of Computational Physics*, 21(3):251 – 269.
- Palma, E. D. and Matano, R. P. (1998). On the implementation of passive open boundary conditions for a general circulation model: The barotropic model. *Journal of Geophysical Research: Oceans*, 103(C1):1319–1341.
- Palomera, I. (1992). Spawning of anchovy *Engraulis encrasicolus* in the northwestern Mediterranean relative to hydrographic features in the region. *Marine ecology progress series. Oldendorf*, 79(3):215–223.
- Roed, L. and Cooper, C. (1987). A study of various open boundary conditions for wind-forced barotropic numerical ocean models. In Nihoul, J. and Jamart, B., editors, *Three-Dimensional Models of Marine and Estuarine Dynamics*, volume 45 of *Elsevier Oceanography Series*, pages 305 – 335. Elsevier.
- Sabates, A. and Olivar, M. (1996). Variation of larval fish distributions associated with variability in the location of a shelf-slope front. *Marine Ecology Progress Series*, 135:11–20.
- She, J. and Klinck, J. M. (2000). Flow near submarine canyons driven by constant winds. *Journal of Geophysical Research: Oceans*, 105(C12):28671–28694.
- Sigman, D. M. and Hain, M. P. (2012). The biological productivity of the ocean. *Nature Education Knowledge*, 3.

- Skliris, N., Goffart, A., Hecq, J. H., and Djenidi, S. (2001). Shelf-slope exchanges associated with a steep submarine canyon off Calvi (Corsica, NW Mediterranean Sea): A modeling approach. *Journal of Geophysical Research: Oceans*, 106(C9):19883–19901.
- Skliris, N., Hecq, J., and Djenidi, S. (2002). Water fluxes at an ocean margin in the presence of a submarine canyon. *Journal of Marine Systems*, 32(13):239 – 251. *Exchange Processes at the Ocean Margins*.
- Smagorinsky, J. (1963). General circulation experiments with the primitive equations. *Monthly Weather Review*, 91(3):99–164.
- Taylor, G. I. (1923). Experiments on the motion of solid bodies in rotating fluids. *Proc. Roy. Soc. A*, 104:213–218.
- Tsimplis, M. N., Proctor, R., and Flather, R. A. (1995). A two-dimensional tidal model for the Mediterranean Sea. *Journal of Geophysical Research: Oceans*, 100(C8):16223–16239.
- Waterhouse, A. F., Allen, S. E., and Bowie, A. W. (2009). Upwelling flow dynamics in long canyons at low rossby number. *Journal of Geophysical Research: Oceans*, 114(C5):n/a–n/a.
- Wurtz, M. (2012). Submarine canyons and their role in the Mediterranean ecosystem. In Wurtz, M., editor, *Mediterranean Submarine Canyons: Ecology and Governance*, pages 11–26, Gland, Switzerland and Mlaga, Spain: IUCN.

Appendix A

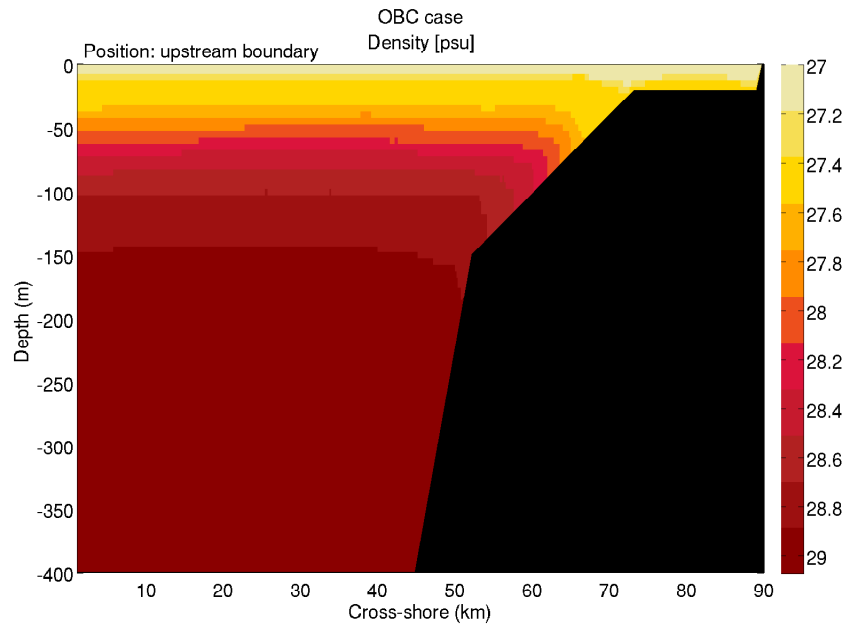
Boundary Conditions

Due to limited computational capacity, it is impractical to model coastal circulation with enough resolution around small topographic features (such as submarine canyons), and still have alongshore boundaries placed beyond the decay distance of coastal trapped waves [Dinniman and Klinck, 2002]. To get around this problem, numerical modellers use either open or periodic boundary conditions; however, open and periodic conditions each have their own problems. Disturbances in periodic domains are not able to advect or propagate out of the model, leading to rapid accumulation of energy and model instability. Also, in periodic boundary conditions, the realism of the flow is limited because alongshore pressure gradients cannot be naturally created; they can only be externally imposed. Imposing open boundary conditions on the hydrostatic primitive equations have shown that a small change in the boundary condition can result in a large change in the interior solution [Oliger and Sundstrom, 1978; Bennett and Kloeden 1978].

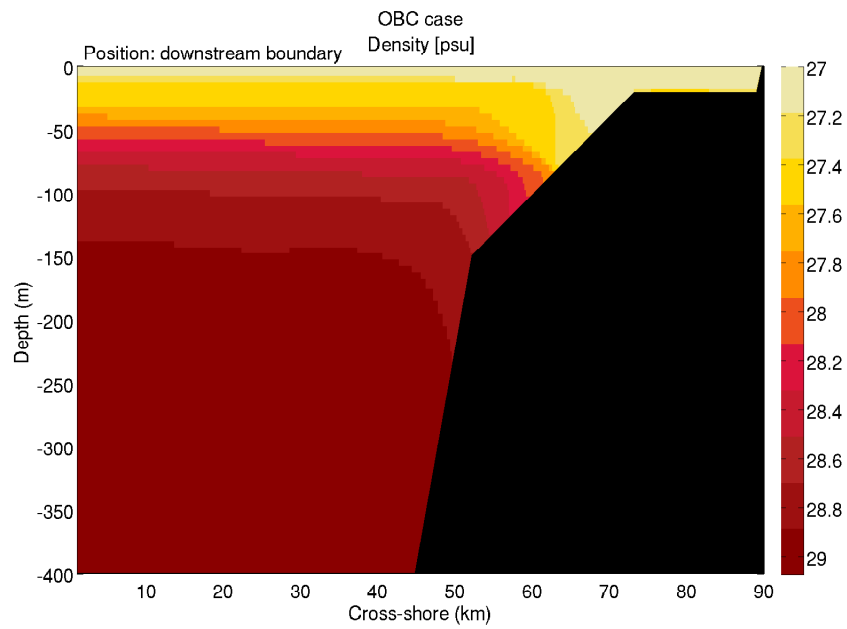
Dinniman and Klinck [2002] ran numerical simulations of submarine canyons with upwelling and downwelling winds to compare different boundary conditions. From their study, the authors found that using a modified Orlanski scheme (one which forces the phase speed to be either zero or the maximum limit as defined by the model grid spacing and time step [Camerlengo and O'Brien, 1980]) produced an undercurrent that caused errors in the alongshore surface height gradient. Similar problems have been seen in other studies using the modified Orlanski scheme on barotropic coastal models [Roed and Cooper, 1987]; [Palma and Matano, 1998]. Stability of the solution was the primary difference between open and periodic boundary conditions in the case for upwelling winds. The presence of the canyon created a disturbance in the barotropic flow, for the periodic case this disturbance was not able to advect or propagate out of the model. Waves in the surface height were visibly travelling with the coast on

their left and they grew well past the point where they were affecting the model flow. The same problem occurred in the downwelling case, but to a lesser extent. Problems were also seen when trying to vary the Coriolis parameter (the β plane) in the periodic conditions. Beta effects are typically weak, especially for small alongshore distances; however, some energy can be lost from the coast due to Rossby waves. Further investigation into these effects could only be studied using open model domains. Of the three schemes used for open boundary conditions (modified Orlandi, Flather radiation scheme [Flather, 1976], and a flow relaxation scheme [Martinsen and Engedahl, 1987]), the Flather radiation scheme and flow relaxation scheme were determined to be the most practical for their coastal ocean setup.

For the current model, both open and periodic boundary conditions were tested. For all simulations, the onshore coast (i.e. northern boundary) was a closed boundary with no-slip conditions. The deep ocean (southern boundary) was open with an Orlandi scheme applied [Orlandi, 1976]. Due to relatively short model run times, the majority of simulations were run with periodic alongshore boundaries (i.e. east and west boundaries); however, a few simulations use open alongshore boundaries, with an Orlandi scheme applied.



(a) upstream boundary



(b) downstream boundary

Figure A.1: Isopycnal cross-sections along the (a) upstream and (b) downstream boundaries for the OBC simulation.

Appendix B

Model Discretization

The MITgcm is discretized using using a finite volume method as described by Adcroft et al. (2004). The governing equations are integrated over (space-filling) finite volumes that make up a discrete grid. By integrating over a finite volume and applying the Gauss-divergence theorem, the continuity equation becomes:

$$A_{east}^u u_{east} - A_{west}^u u_{west} + A_{north}^v v_{north} - A_{south}^v v_{south} + A_{up}^w w_{up} - A_{down}^w w_{down} = 0 \quad (\text{B.1})$$

A (the area of each cell) describes the geometry of a finite volume and the budget is written conceptually in terms of normal flow across the cell face. No normal flow at a rigid boundary translates to setting the rigid boundary velocity to zero (i.e. a cell lying along bottom topography would have $A_{down}^w w_{down} = 0$). The components of velocity are staggered in the horizontal on an Arakawa C grid and a Lorenz grid is used on the vertical. The same finite volume treatment of the continuity equation (B.1) is applied to the tracer equations.

The non-hydrostatic capability allows the model to simulate overturning and mixing processes. This can be used in conjunction with the finite volume representation of topography to become a flexible tool for studying mixing processes and dynamical interactions with steep topography.

Appendix C

Advection Scheme

In oceanography, advection is the transport of a property due to a fluid's bulk motion; there can be active and passive properties. Active properties (e.g. temperature and salinity) are advected due to the currents of a fluid. These properties affect density distribution, which in turn affects pressure field, and pressure field is used in the calculation of currents. Therefore, the accuracy in advection of active tracers is important to overall flow dynamics of a model.

The MITgcm offers eight different advection schemes, each of which is optimum for different applications. The eight schemes fall into 3 general categories: 1) linear schemes integrated with the Adams-Bashforth method (2nd, 3rd, and 4th ordered), 2) unlimited, but multi-dimensional schemes (2nd, 3rd, and 4th order direct space-time), 3) flux limited (2nd and 3rd order). The MITgcm manual offers guidelines for finding the most suitable scheme, although use of trial and error is encouraged. It is recommended that if using a high resolution model, a higher order scheme will give a more accurate solution, but scale-selective diffusion might need to be employed. For solutions with shocks or propagating fronts, a flux limited scheme is highly recommended.

Appendix D

Extended Simulation

An extended simulation of the UW case was modelled to determine how steady the flow is in time. The simulation was doubled to run for 20 model days. Flux time series indicates that flow oscillation in all 3 directions strengthens after day 12 (Figure D.1). Results averaged over model days 10-20 show flow strengthens in the domain, which impacts magnitudes of variables such as velocity, density, and vorticity. Although zonal flux averaged from day 10-20 only varied 4% from day 4-10 averages, meridional and vertical fluxes were found to vary approximately 90% from the model day 4-10 averages. Although flux is stronger during the extended simulation, plots of individual averaged (day 10-20) parameters (not shown) indicate patterns in flow dynamics did not change.

Flow oscillations seen in the flux time series indicate an instability may be occurring around model day 12. Allen and Newberger [1998] modeled two-dimensional, time-dependent, wind-forced, stratified downwelling circulation along a continental shelf. The authors found that near-bottom offshore flow developed time- and space-dependent fluctuations in the bottom boundary layer. Potential vorticity that was initially negative becomes positive in the regions of fluctuation.

In the extended simulation, daily snapshots of zonal velocity show fluctuations in near zero velocity along the continental shelf (not shown). Similarly, daily snapshots of vorticity show regions of weakly positive and 0 vorticity along the continental shelf away from the canyon (not shown); regions which have everywhere negative vorticity during the advection averaged period. These are likely indications that instabilities are occurring along the continental shelf after model day 12. Thus, model averages from day 4-10 are good indicators of the dynamics occurring during the most steady period of flow, before instabilities begin to appear and grow.

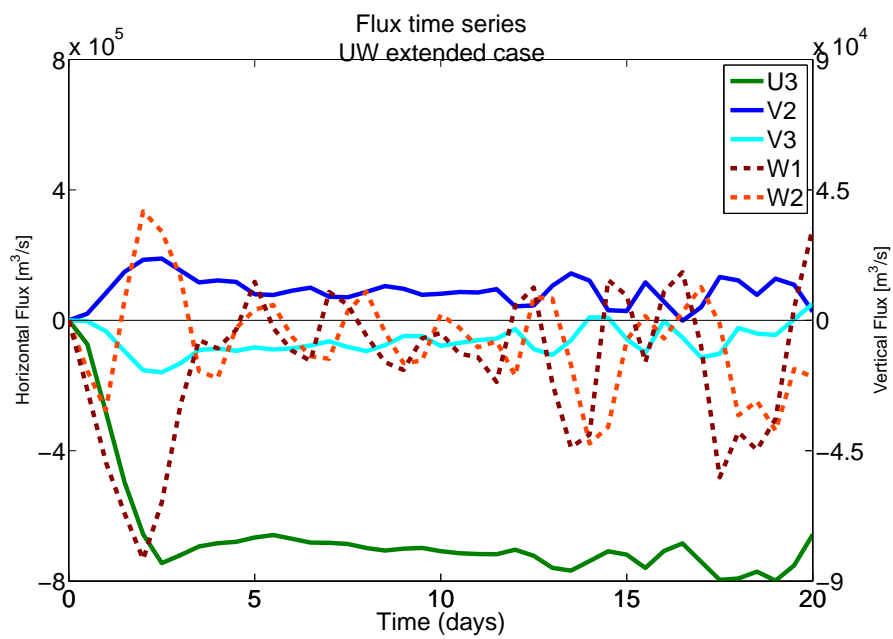
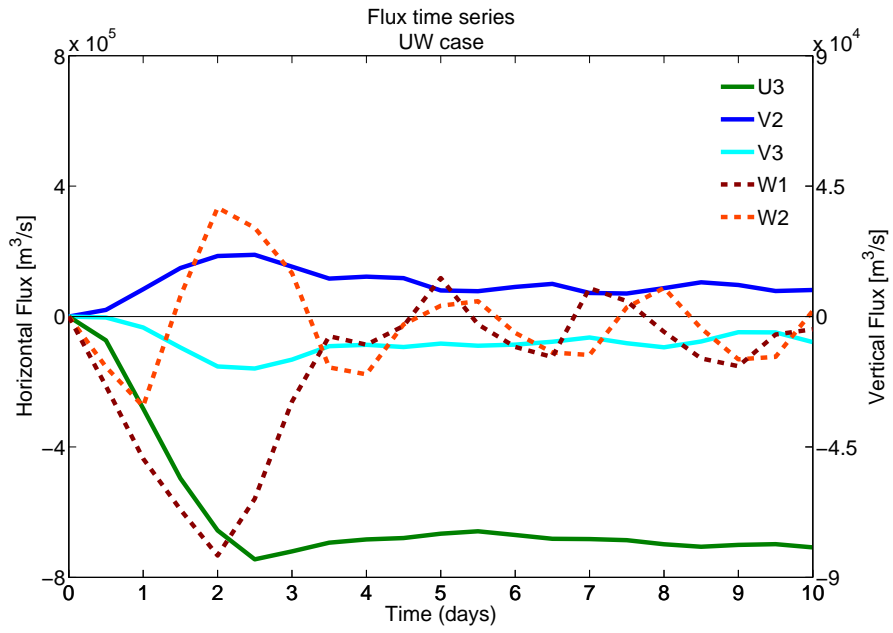


Figure D.1: Time series of horizontal and vertical flux over the canyon for core simulation (UW), extended for 20 model days.

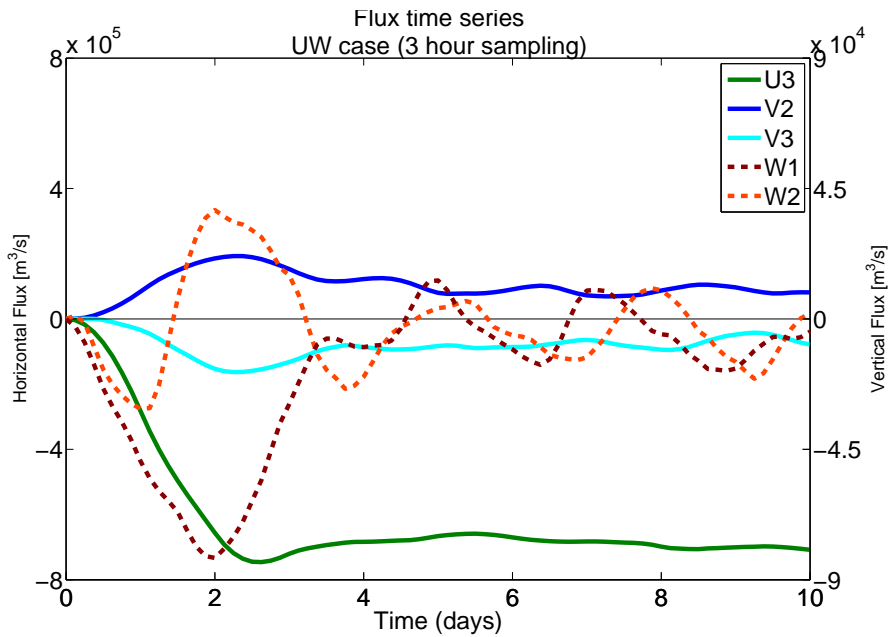
Appendix E

Aliasing

To determine if the 12 hour output of model data is not aliasing the results, a 10 day core case (UW) run was simulated with output collected every 3 hours. There are small differences in vertical flux values during the first 2-3 days of simulation (Figure E.1). However, during the advection dominant phase there appears to be minimal differences in trends across the vertical planes. Vertical flux estimates averaged from model day 4-10 were $-9.39 \times 10^3 \text{ m}^3 \text{ s}^{-1}$ for the original (12 hour sampling) run and $-8.52 \times 10^3 \text{ m}^3 \text{ s}^{-1}$ for the 3 hour sampling run, therefore there is a 10% relative error.



(a) 12 hour model output



(b) 3 hour model output

Figure E.1: Horizontal and vertical flux time series in and around a canyon based on model output every (a) 12 hours and (b) 3 hours.

Appendix F

Additional Figures

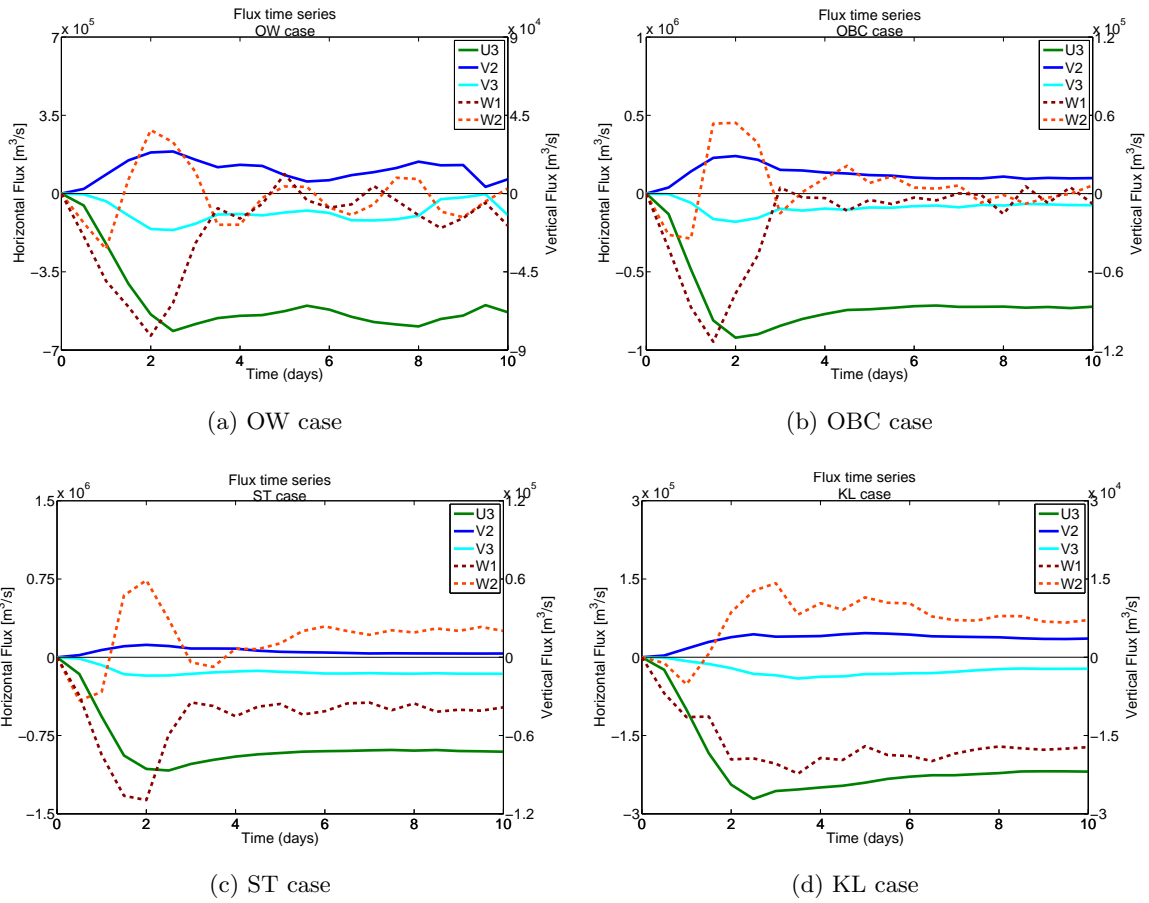
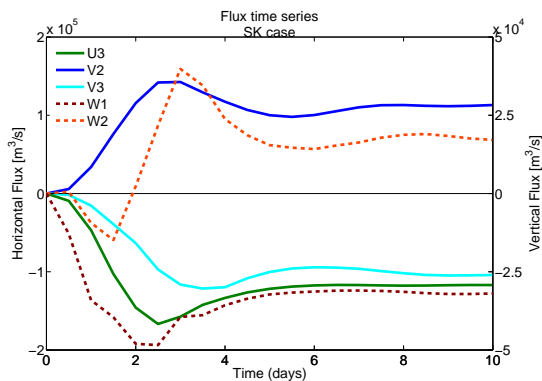
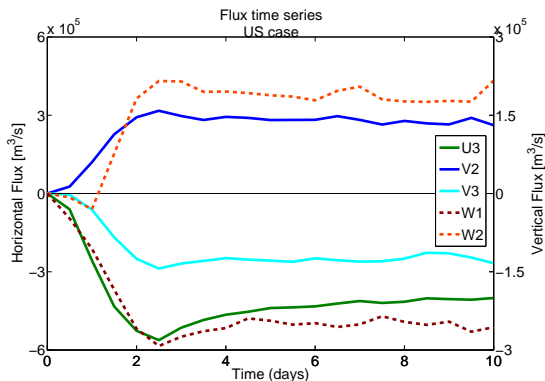


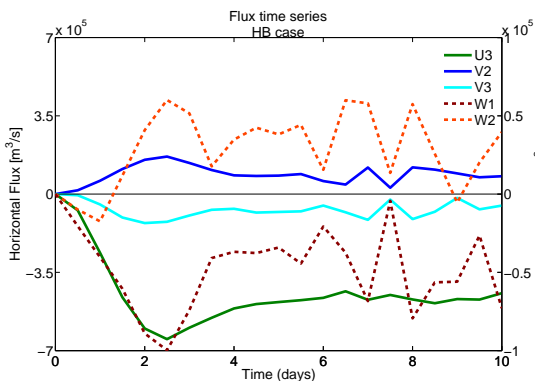
Figure F.1: Time series of horizontal and vertical flux directly over the canyon. Same as Figure 2.2.



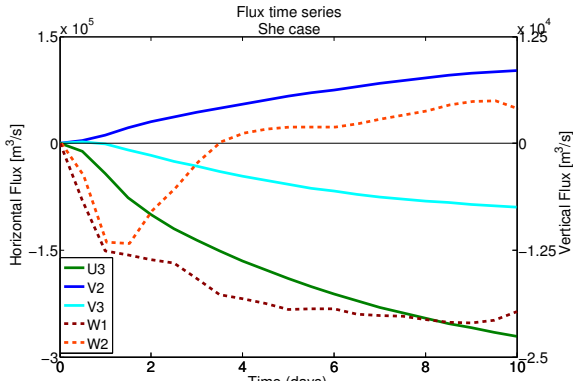
(e) SK case



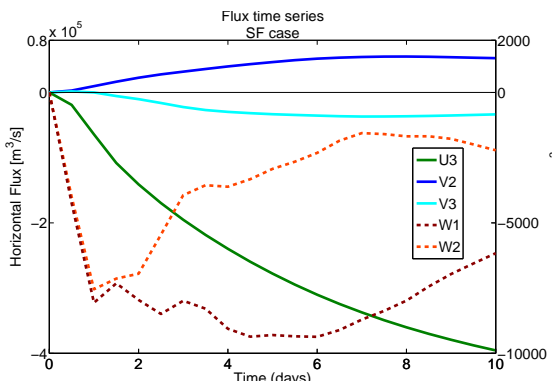
(f) US case



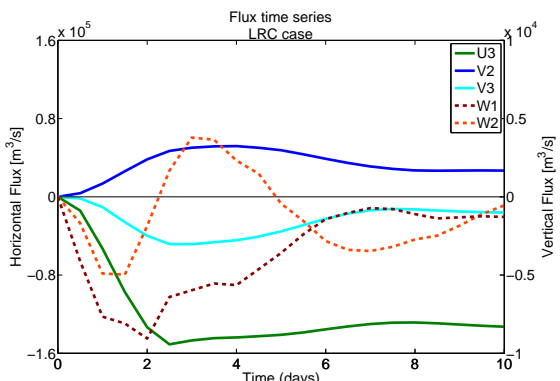
(g) HB case



(h) She case

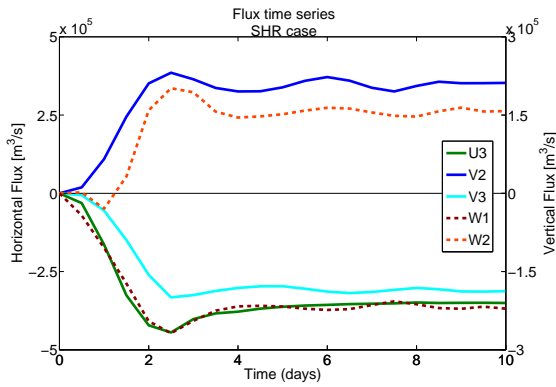


(i) SF case

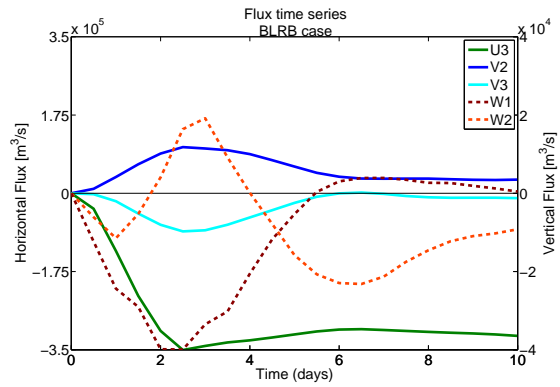


(j) LRC case

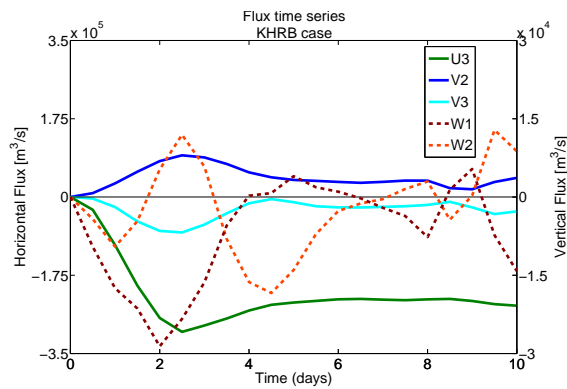
Figure F.1: Continued.



(k) SHR case

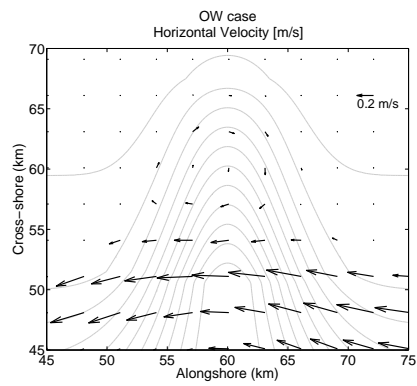


(l) BLRB case

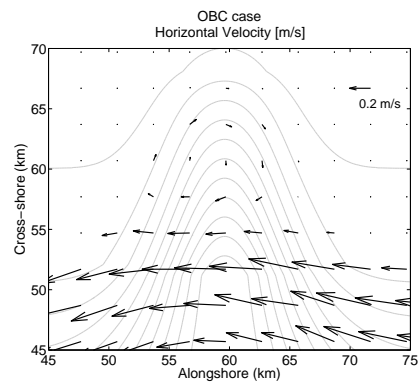


(m) KHRB case

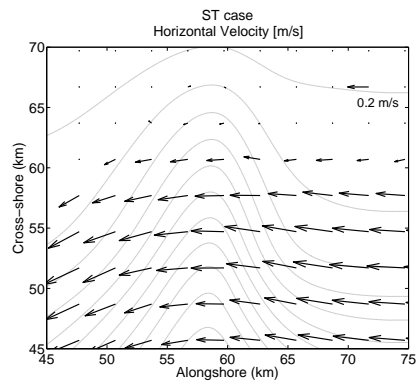
Figure F.1: Continued.



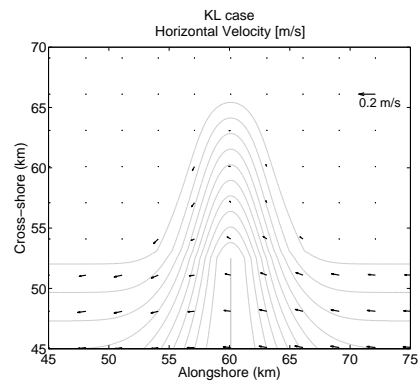
(a) OW case



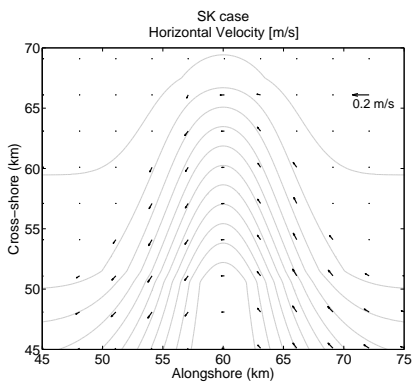
(b) OBC case



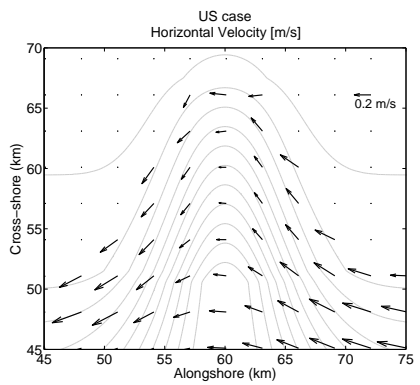
(c) ST case



(d) KL case

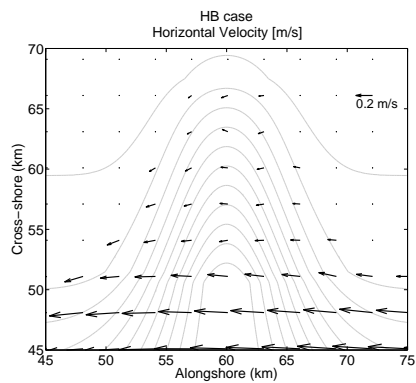


(e) SK case

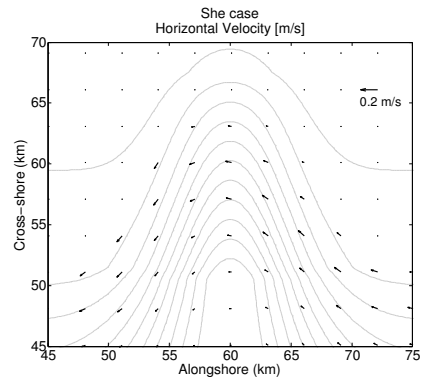


(f) US case

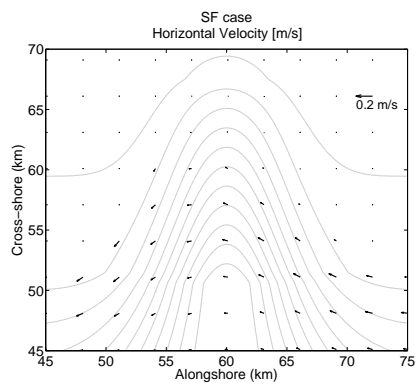
Figure F.2: Horizontal velocity vectors at shelf break depth (150 m). Same as Figure 2.4.



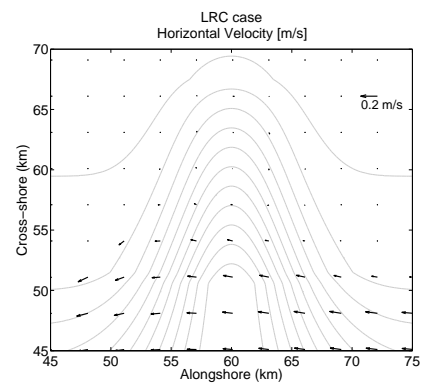
(g) HB case



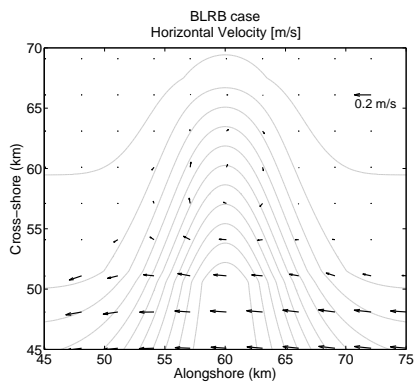
(h) She case



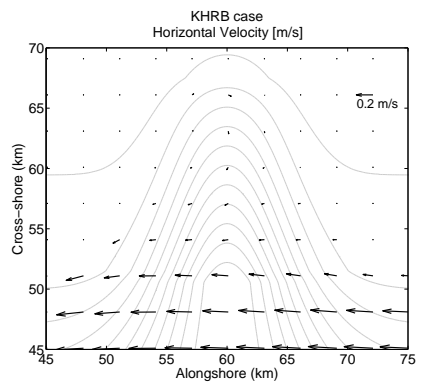
(i) SF case



(j) LRC case



(k) BLRB case



(l) KHRB case

Figure F.2: Continued.

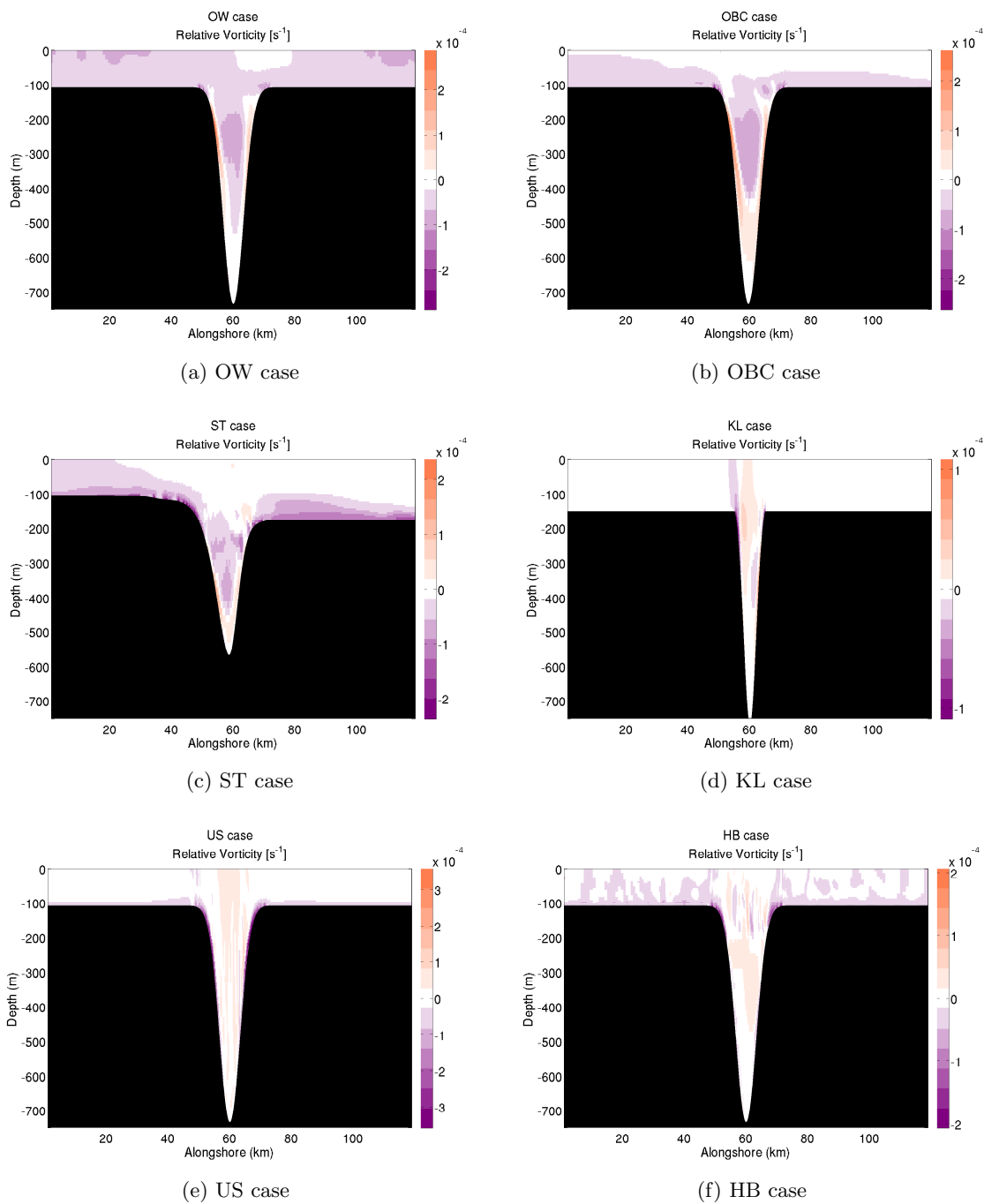
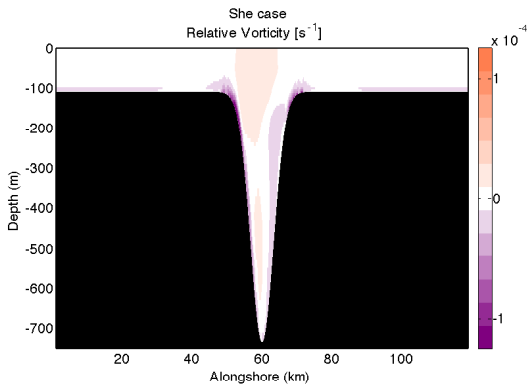
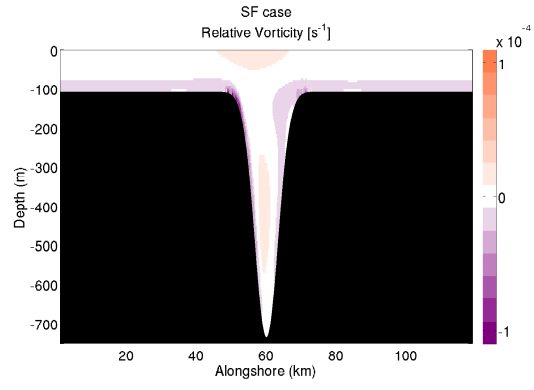


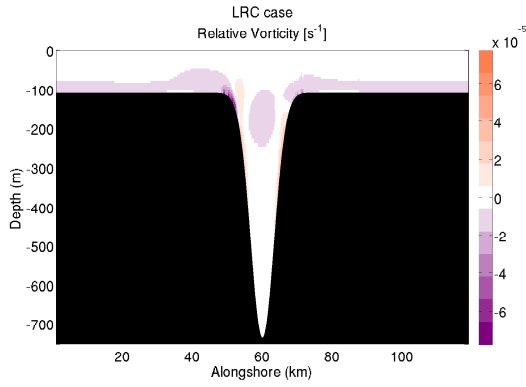
Figure F.3: Cross-section of vorticity at mid-canyon. Same as Figure 2.7.



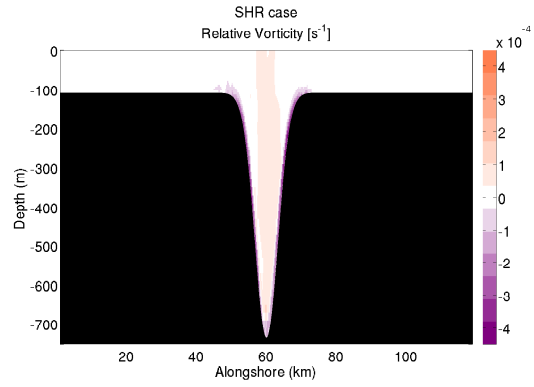
(g) She case



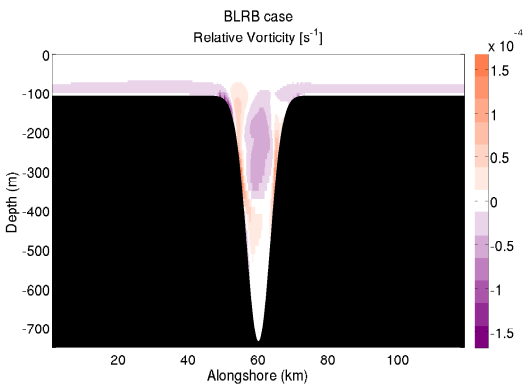
(h) SF case



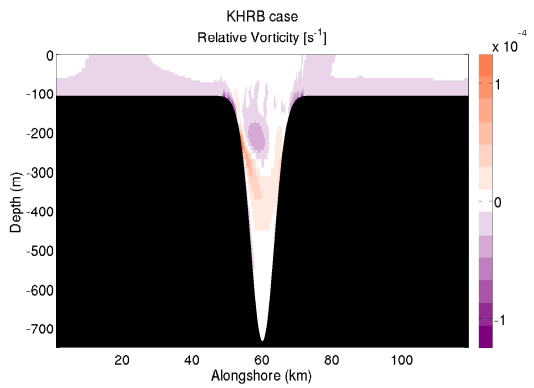
(i) LRC case



(j) SHR case

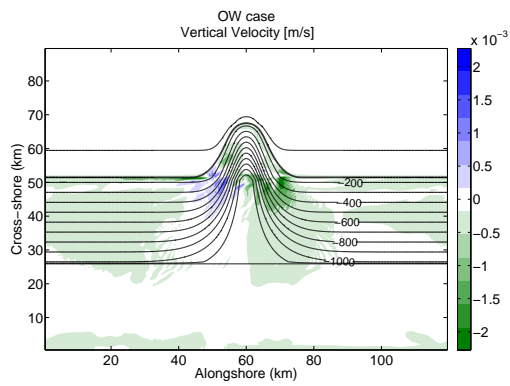


(k) BLRB case

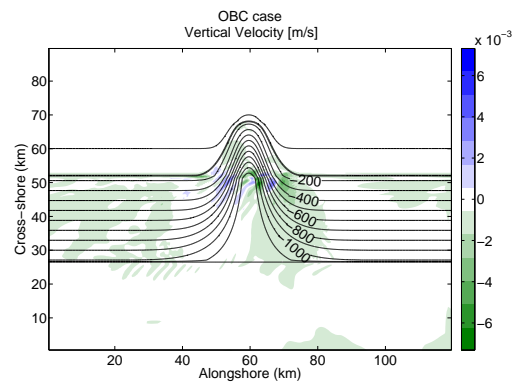


(l) KHRB case

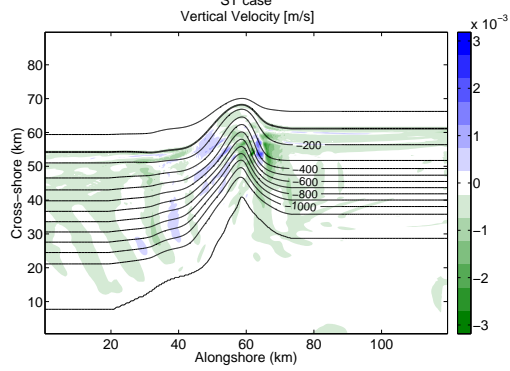
Figure F.3: Continued.



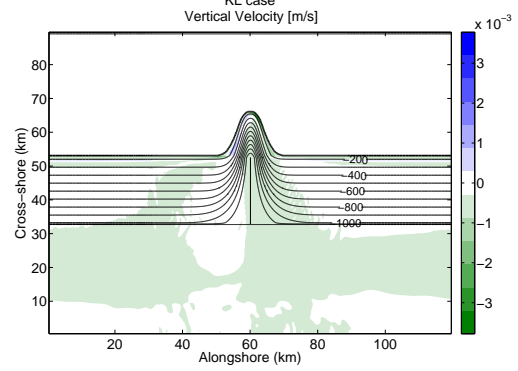
(a) OW case



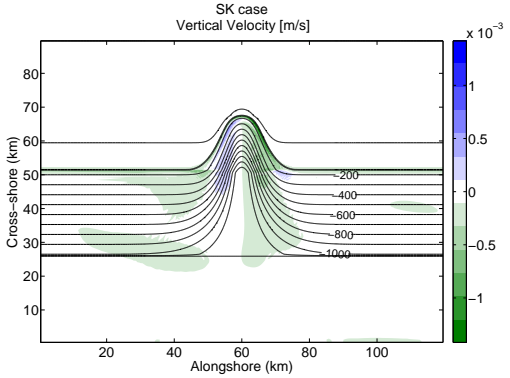
(b) OBC case



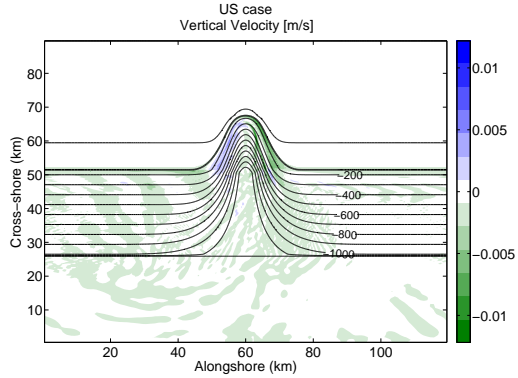
(c) ST case



(d) KL case

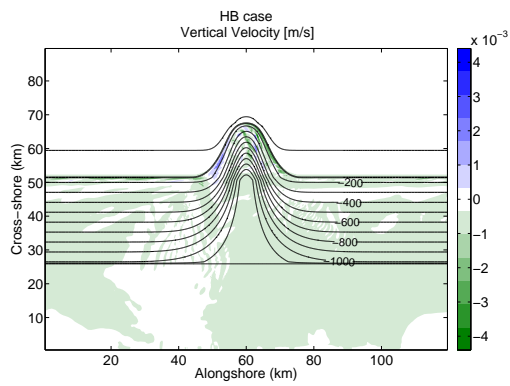


(e) SK case

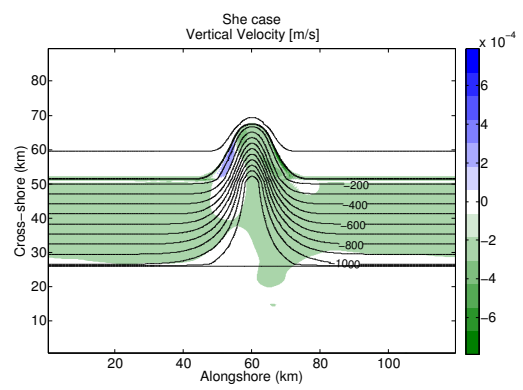


(f) US case

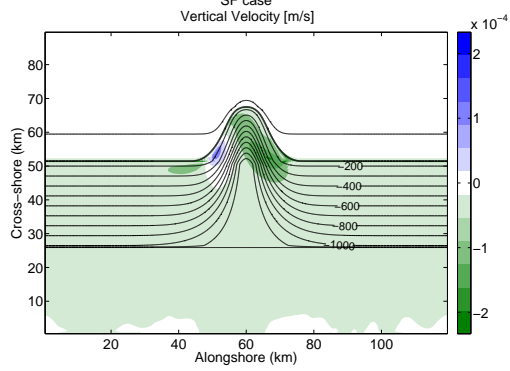
Figure F.4: Vertical velocity at shelf break depth (150 m). Same as Figure 2.8.



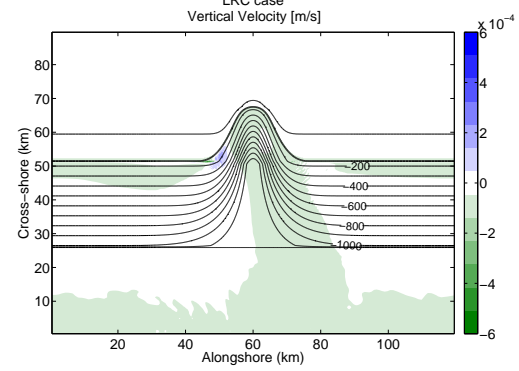
(g) HB case



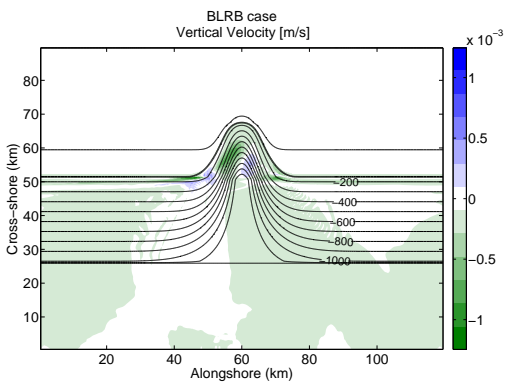
(h) She case



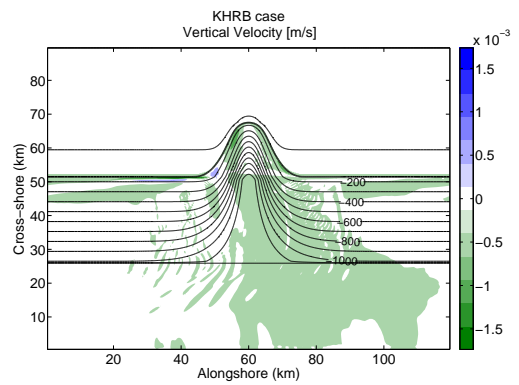
(i) SF case



(j) LRC case



(k) BLRB case



(l) KHRB case

Figure F.4: Continued.

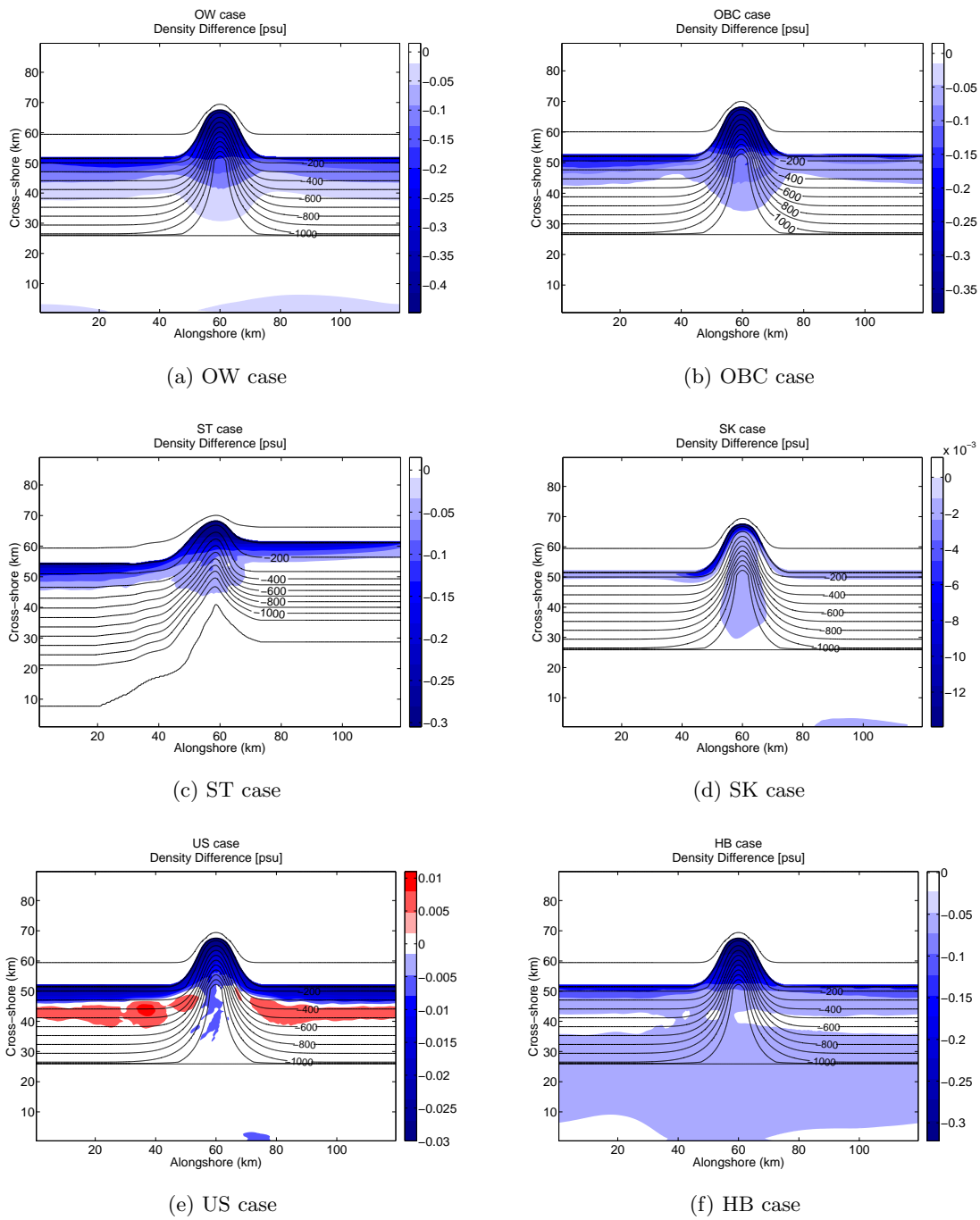
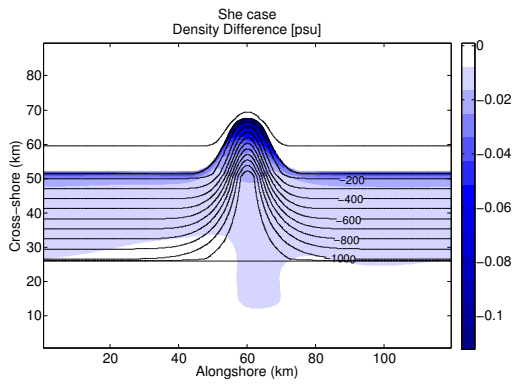
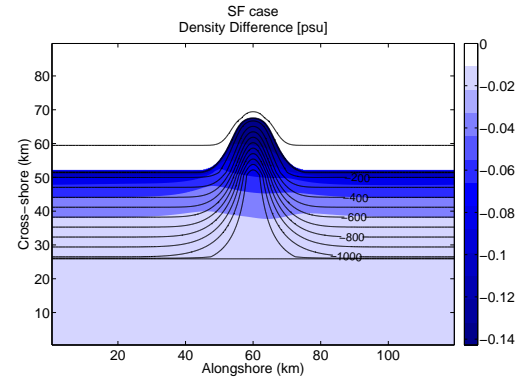


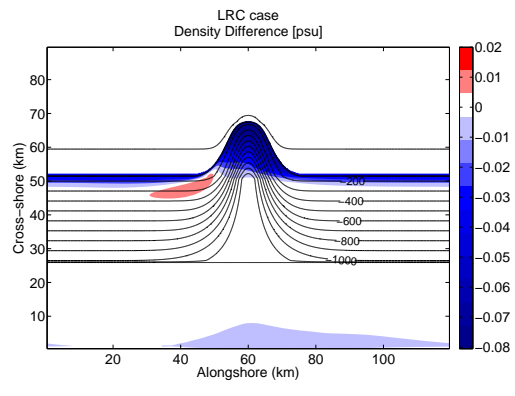
Figure F.5: Density anomaly at shelf break depth (150 m). Same as Figure 2.11.



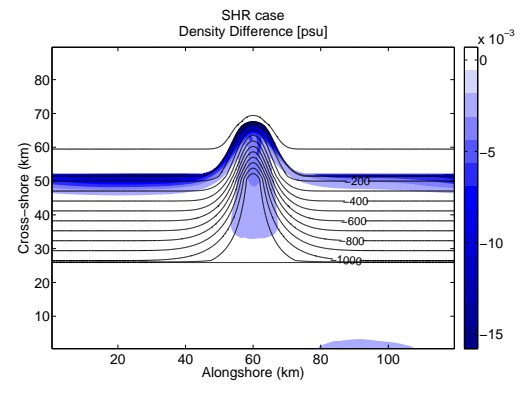
(g) She case



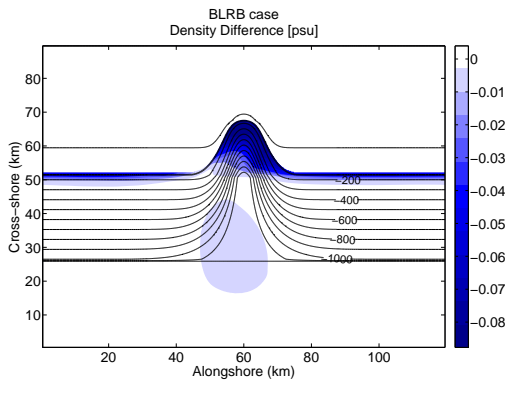
(h) SF case



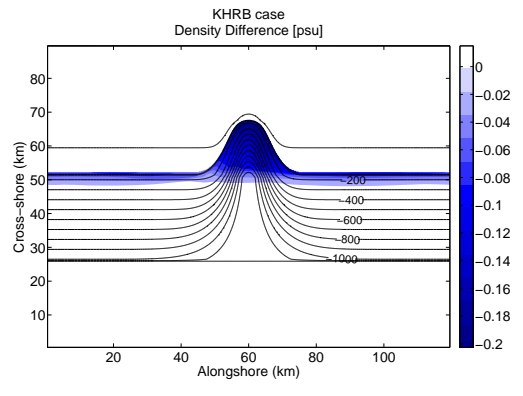
(i) LRC case



(j) SHR case



(k) BLRB case



(l) KHRB case

Figure F.5: Continued.

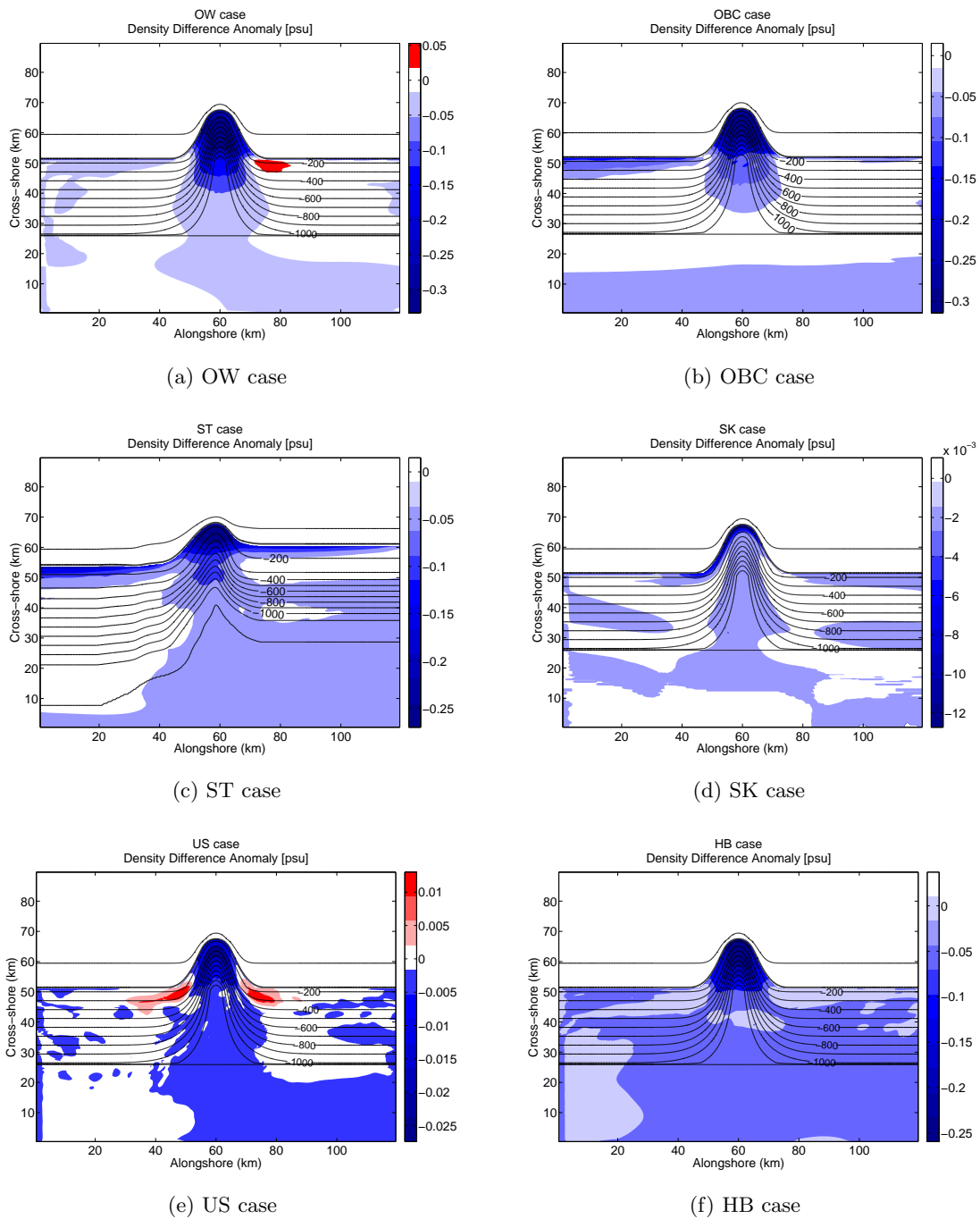
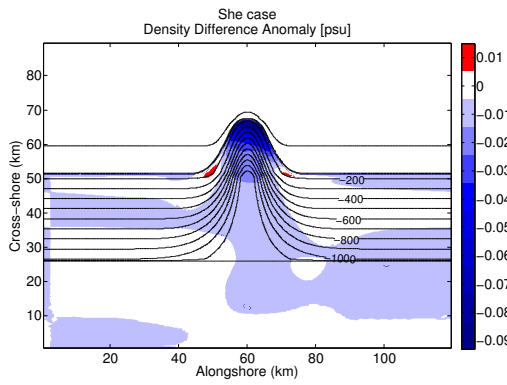
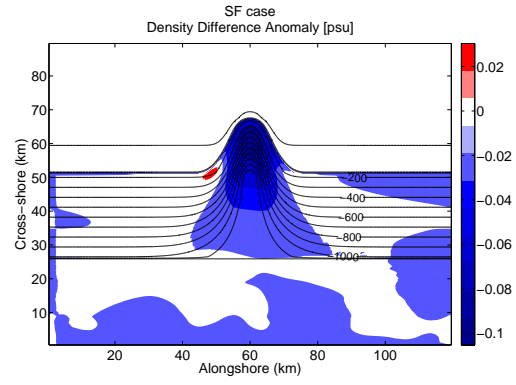


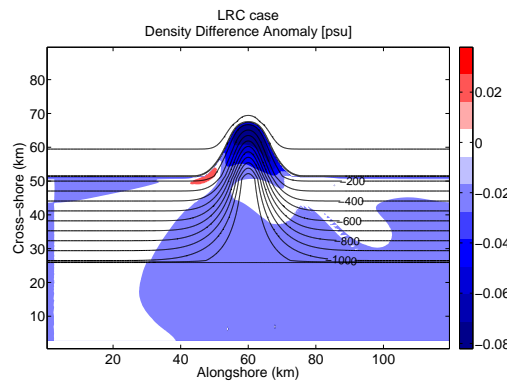
Figure F.6: Density difference anomaly at shelf break depth (150 m). Same as Figure 2.12.



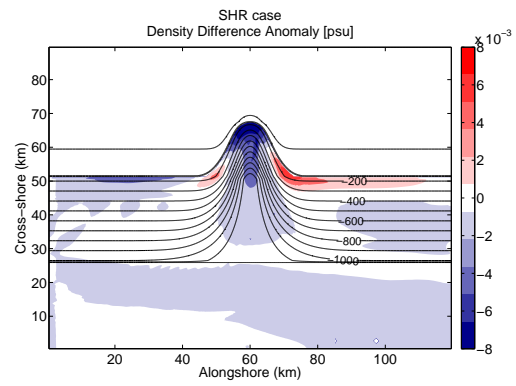
(g) She case



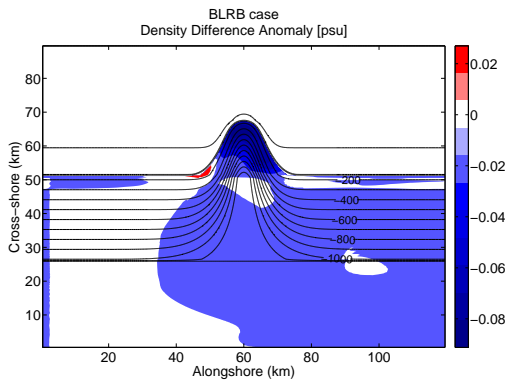
(h) SF case



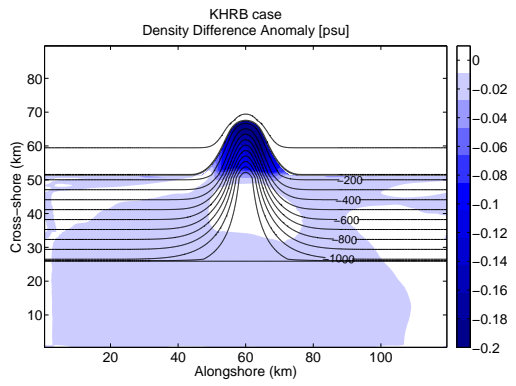
(i) LRC case



(j) SHR case

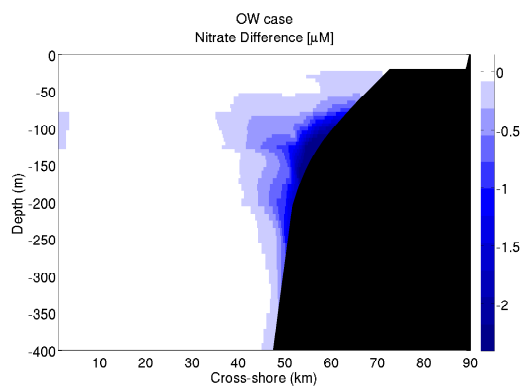


(k) BLRB case

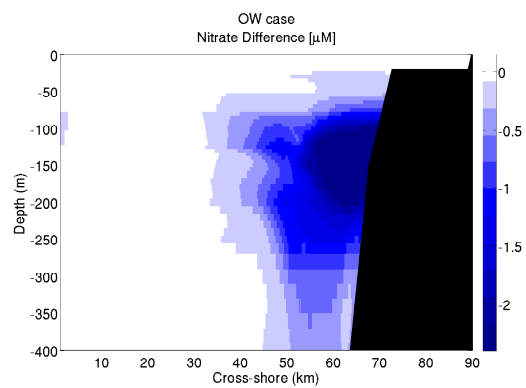


(l) KHRB case

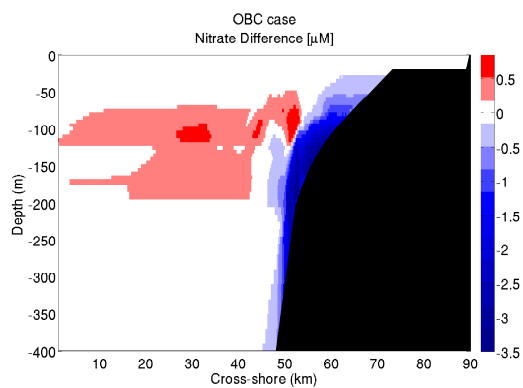
Figure F.6: Continued.



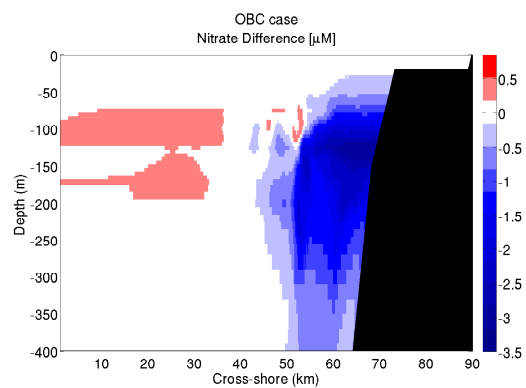
(a) OW case, upstream



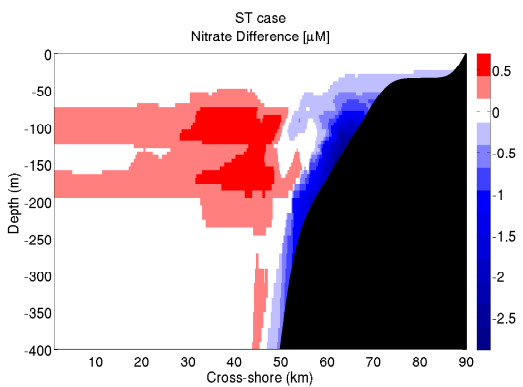
(b) OW case, axial



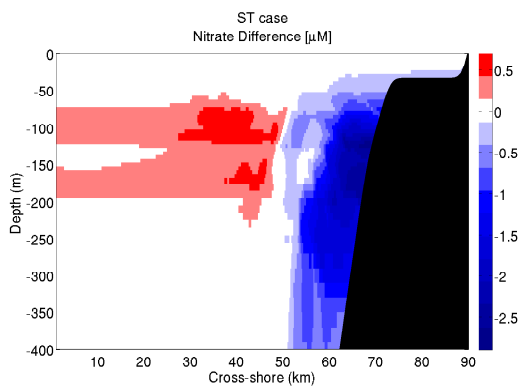
(c) OBC case, upstream



(d) OBC case, axial

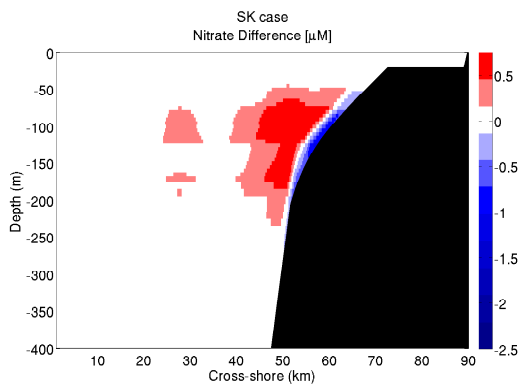


(e) ST case, upstream

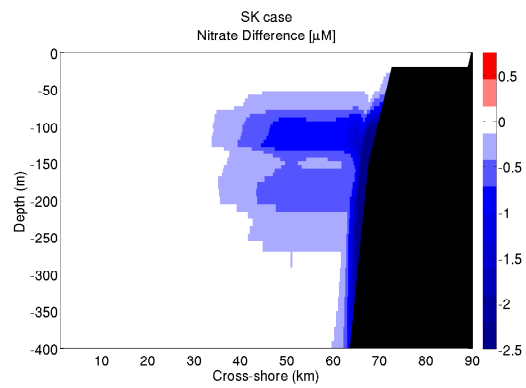


(f) ST case, axial

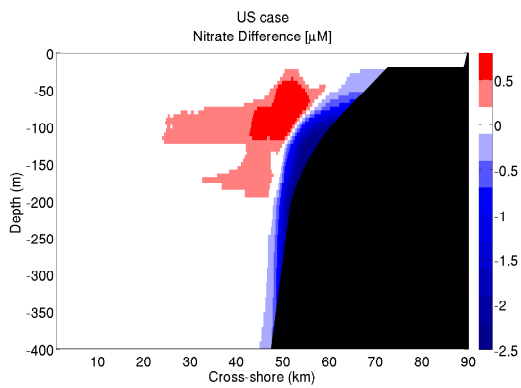
Figure F.7: Nitrate anomaly 10 km upstream (right) and along canyon axis (right). Same as Figure 2.13.



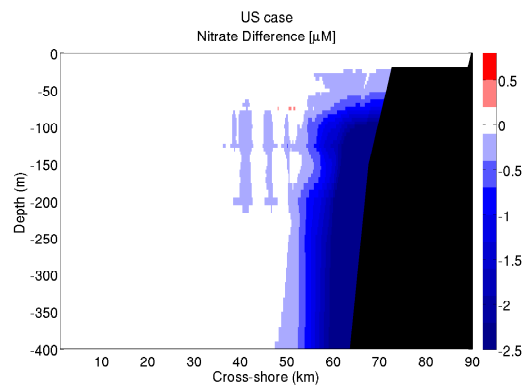
(g) SK case, upstream



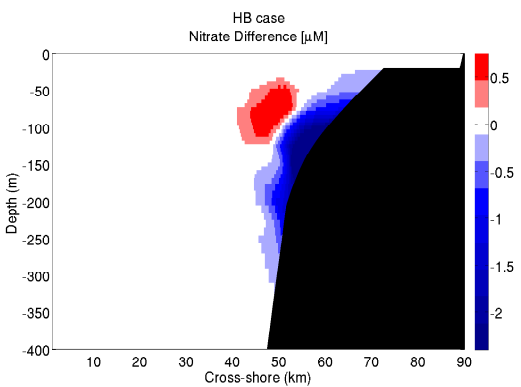
(h) SK case, axial



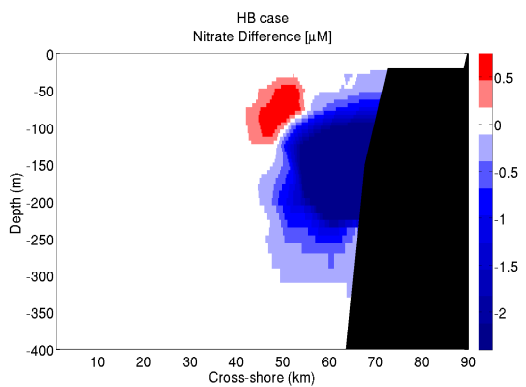
(i) US case, upstream



(j) US case, axial

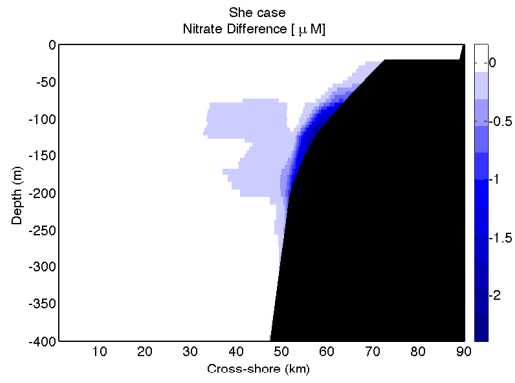


(k) HB case, upstream

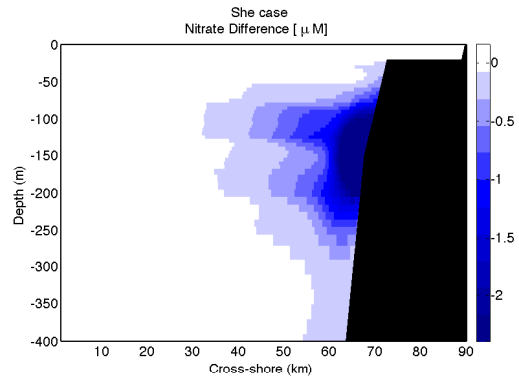


(l) HB case, axial

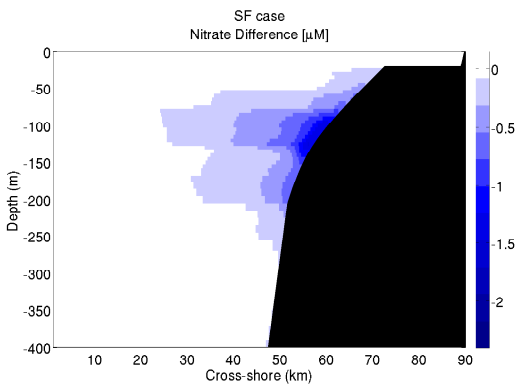
Figure F.7: Continued.



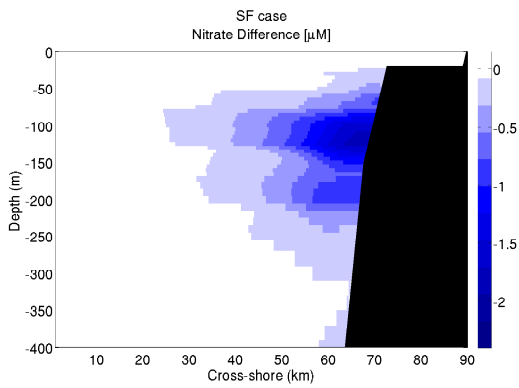
(m) She case, upstream



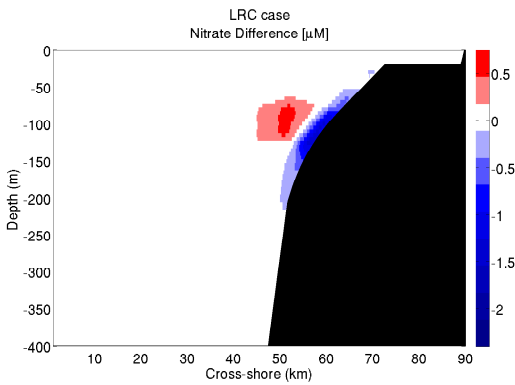
(n) She case, axial



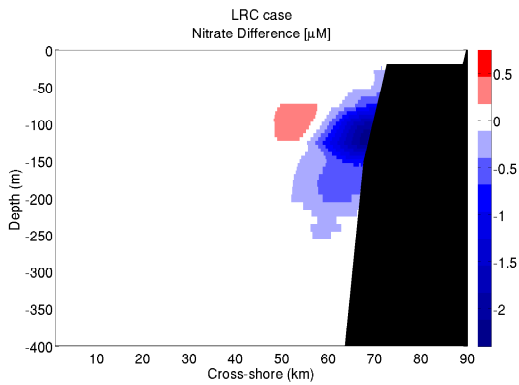
(o) SF case, upstream



(p) SF case, axial

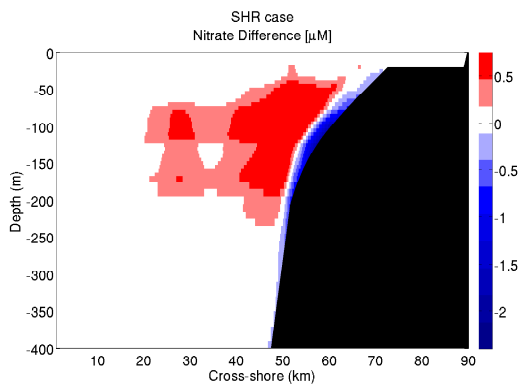


(q) LRC case, upstream

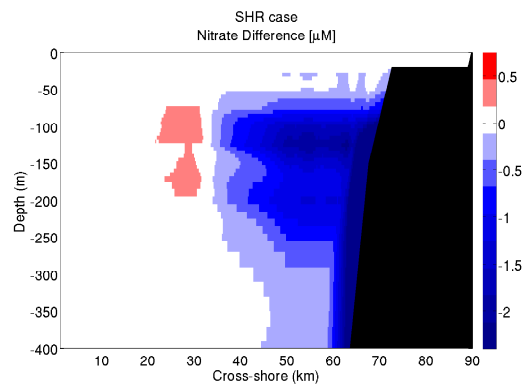


(r) LRC case, axial

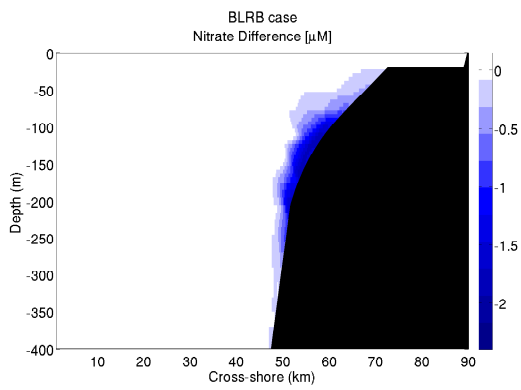
Figure F.7: Continued.



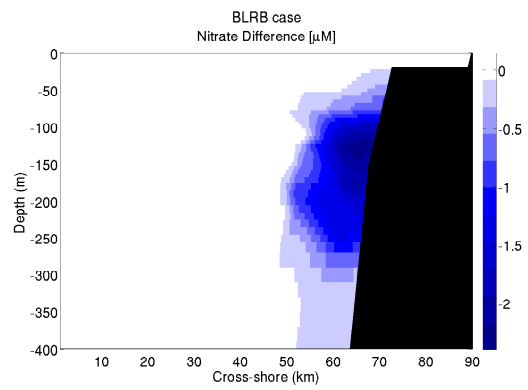
(s) SHR case, upstream



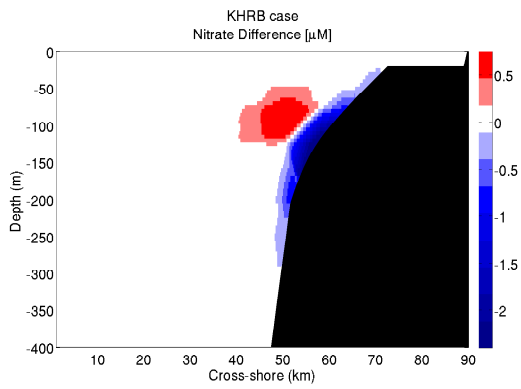
(t) SHR case, axial



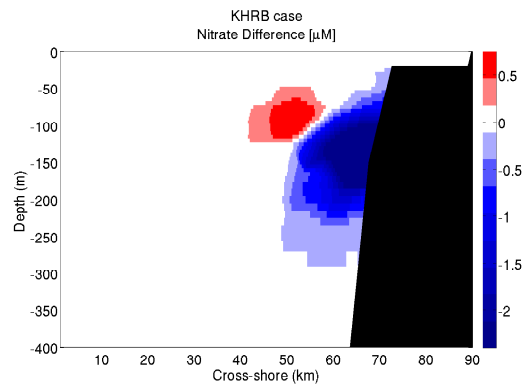
(u) BLRB case, upstream



(v) BLRB case, axial



(w) KHRB case, upstream



(x) KHRB case, axial

Figure F.7: Continued.